FRIEDRICH-SCHILLER-
UNIVERSITÄT
JENA

THEORETICAL STUDY OF ATOMIC IONIZATION UNDER INTENSE LASER PULSES

DISSERTATION

zur Erlangung des akademischen Grades

doctor rerum naturalium (Dr. rer. nat.)

vorgelegt dem Rat der
Physikalisch-Astronomischen Fakultät
der
Friedrich-Schiller-Universität Jena

von

von M. Sc. Danish Furekh Dar

geboren am 09.02.1998 in Anantnag, Indien

GUTACHTER:

1. Prof. Dr. Stephan Fritzsche (Friedrich-Schiller-Universität Jena, Germany)

2. Dr. Wilhelm Becker (Max-Born-Institut Berlin, Germany)

3. Prof. Dr. Lars Bojer Madsen (Aarhus University, Denmark)

TAG DER DISPUTATION: 04 November 2025

This thesis is dedicated to the blessed memory
of my beloved grandparents.

May they find joy in the world beyond
as they brought joy to this one.

ABSTRACT

Strong-field ionization (SFI) serves as a cornerstone in understanding ultrafast electron dynamics and light-matter interactions under the influence of intense laser fields. This thesis presents a rigorous theoretical investigation of SFI, focusing on above-threshold ionization (ATI)—a process in which ionized electrons absorb additional photons above the ionization threshold, leading to discrete high-energy peaks in the photoelectron spectrum, as well as quantum interference phenomena and nondipole effects across different laser field configurations.

The study first examines SFI driven by few-cycle laser pulses within the strong-field approximation (SFA), systematically comparing dipole and nondipole regimes. While the dipole approximation effectively captures quantum interference structures in photoelectron momentum distributions (PMDs), nondipole effects induce significant momentum shifts and asymmetries, particularly along the laser propagation axis. Theoretical predictions for so-called peak shifts, specially for a few-cycle pulse, show enhanced experimental agreement upon incorporating nondipole corrections.

To unravel these strong-field dynamics, this work employs two complementary analytical approaches: (1) The Jacobi-Anger expansion provides a complete decomposition of the ionization transition amplitude into photon orders in terms of Bessel functions. (2) The saddle-point method isolates dominant quantum orbits (stationary solutions to the classical action) that contribute maximally to the ionization amplitude, offering both physical insight and improved computational efficiency in resolving PMDs within different laser configurations. The validity regimes, advantages, and limitations of these methods are critically assessed. A detailed analysis of nonlinear interference effects reveals how electron dynamics are governed by the interplay of fundamental frequencies concealed within a pulse. The influence of the carrier-envelope phase on interference structures is quantified, while an increasing number of optical cycles is shown to constrain PMD features and reshape the energy-resolved ionization spectrum.

In the end, the theoretical framework is generalized to structured light fields, particularly twisted Bessel pulses carrying orbital angular momentum (OAM). Within the SFA and saddle-point formalism, analytical expressions for the ionization amplitude are derived for hydrogenic targets. The impact of the Bessel pulse's opening angle and OAM on shaping PMDs and ATI peak positions is systematically investigated, highlighting their role as tunable parameters for electron emission.

ZUSAMMENFASSUNG

Die Starkfeldionisation (engl. SFI) bildet einen Grundpfeiler zum Verständnis ultraschneller Elektronendynamik und Licht-Materie-Wechselwirkungen unter dem Einfluss intensiver Laserfelder. Diese Dissertation präsentiert eine rigorose theoretische Untersuchung der SFI mit Fokus auf die Above-Threshold-Ionisation (engl. ATI) – einen Prozess, bei dem ionisierte Elektronen zusätzliche Photonen oberhalb der Ionisationsschwelle absorbieren, was zu diskreten, hochenergetischen Peaks im Photoelektronenspektrum führt – sowie auf Quanteninterferenzphänomene und Nicht-Dipol-Effekte in verschiedenen Laserfeldkonfigurationen.

Die Studie untersucht zunächst die SFI, angetrieben durch Laserpulse mit wenigen optischen Zyklen innerhalb der Starkfeldnäherung (engl. SFA), und vergleicht systematisch Dipol- und Nicht-Dipol-Regime. Während die Dipolnäherung Quanteninterferenzstrukturen in Photoelektronenimpulsverteilungen (engl. PMDs) effektiv beschreibt, verursachen Nicht-Dipol-Effekte signifikante Impulsverschiebungen und Asymmetrien, insbesondere entlang der Ausbreitungsachse des Lasers. Theoretische Vorhersagen für sogenannte Peak-Shifts, insbesondere für Pulse mit wenigen optischen Zyklen, zeigen eine verbesserte Übereinstimmung mit Experimenten bei Einbeziehung von Nicht-Dipol-Korrekturen.

Um diese Starkfelddynamiken zu entschlüsseln, werden in dieser Arbeit zwei komplementäre analytische Ansätze verwendet: (1) Die Jacobi-Anger-Entwicklung liefert eine vollständige Zerlegung der Ionisationsübergangsamplitude in Photonenordnungen mittels Besselfunktionen. (2) Die Sattelpunktsmethode isoliert dominante Quantenbahnen (stationäre Lösungen der klassischen Wirkung), die maximal zur Ionisationsamplitude beitragen, und bietet sowohl physikalische Einsichten als auch verbesserte Recheneffizienz bei der Auflösung von PMDs in verschiedenen Laserkonfigurationen. Die Gültigkeitsbereiche, Vorteile und Grenzen dieser Methoden werden kritisch bewertet. Eine detaillierte Analyse nichtlinearer Interferenzeffekte zeigt, wie die Elektronendynamik durch das Zusammenspiel fundamentaler Frequenzen innerhalb eines Pulses bestimmt wird. Der Einfluss der Träger-Einhüllenden-Phase auf Interferenzstrukturen wird quantifiziert, während eine zunehmende Anzahl optischer Zyklen die Merkmale der PMDs einschränkt und das energieaufgelöste Ionisationsspektrum verändert.

Abschließend wird der theoretische Rahmen auf strukturierte Lichtfelder verallgemeinert, insbesondere auf getwistete Bessel-Pulse mit orbitalem Drehimpuls (engl.

OAM). Innerhalb der SFA und des Sattelpunktsformalismus werden analytische Ausdrücke für die Ionisationsamplitude für wasserstoffähnliche Zielatome hergeleitet. Der Einfluss des Öffnungswinkels und des OAM der Bessel-Pulse auf die Gestalt von PMDs und ATI-Peak-Positionen wird systematisch untersucht, wobei ihre Rolle als einstellbare Parameter für die Elektronenemission hervorgehoben wird.

PUBLICATIONS

The material presented in this thesis was contributed to the following publications:

- *Comparison between Jacobi–Anger and saddle point methods to treat Above-threshold ionization*
  Danish Furekh Dar and Stephan Fritzsche
  Journal of Physics B: Atomic, Molecular and Optical Physics **58**, (2025)

- *Photoionization dynamics in intense few-cycle twisted laser pulses*
  Danish Furekh Dar, Anne Weber, Shreyas Ramakrishna and Stephan Fritzsche
  PHYSICAL REVIEW A **111**, 053113 (2025)

- *Nonlinear interference and electron dynamics: Probing photoelectron momentum distributions in strong-field ionization*
  Danish Furekh Dar, and Stephan Fritzsche
  PHYSICAL REVIEW A **109**, L041101 (2024)

- *Nondipole strong-field approximation for above-threshold ionization in a few-cycle pulse*
  Danish Furekh Dar, Björn Minneker, and Stephan Fritzsche
  PHYSICAL REVIEW A **107**, 053102 (2023)

- *Pulse Cycle Dependent Nondipole Effects in Above-Threshold Ionization*
  Danish Furekh Dar, and Stephan Fritzsche
  Atoms **11**, 11060097 (2023)

ACKNOWLEDGMENTS

Gratitude makes sense of our past,
brings peace for today,
and creates a vision for tomorrow.
–Melody Beattie

Completing this thesis has been a challenging yet rewarding journey, and I am deeply grateful to all those who have supported me throughout this process.

First and foremost, I would like to express my deepest gratitude to my supervisor, *Prof. Stephan Fritzsche*, for accepting me as his PhD student and providing me with the extraordinary opportunity to grow as a researcher. His trust in my potential from the very beginning gave me the confidence to pursue challenging questions and push the boundaries of my understanding.

I am grateful to *Prof. Fritzsche* for his exceptional mentorship, which extended far beyond the boundaries of academic supervision. His keen eye for scientific writing not only refined my technical expression but also transformed the way I communicate research, teaching me how to craft a compelling narrative that resonates with the scientific community. I am also grateful to *Dr. Bindiya Arora* for guiding me throughout my research journey. From my bachelor's to my master's degree, she introduced me to the exciting world of science and gave me my first real experience in research. Her constant support and belief in me helped me become the researcher I am today. This thesis is a reflection of everything she taught me from the very beginning.

I am also grateful to *Dr. Birger Böning* for first introducing me to the fascinating field of strong-field physics. His enthusiasm and expertise ignited my curiosity and laid the foundation for my academic journey. Without his early mentorship, introducing me to key concepts, sharing his profound insights, and encouraging me to explore bold ideas, this thesis would not have taken shape. Dr. Böning's generosity with his time and knowledge opened doors I had not imagined, and for that, I will always be grateful.

I am equally grateful to all my colleagues for stimulating discussions, collaborative meetings, and the vibrant academic environment we shared. Our exchanges of ideas, whether during coffee breaks or seminars fundamentally shaped my research perspective. *Dr. Giorgio Visentin* , my officemate, thank you for all the laughs, the ran-

dom chats about life, and the moments when we both just needed a break from science. You made the PhD grind so much lighter, and I'll always remember our shared laughs at whatever nonsense the day brought. This journey would've been way less fun without you.

A special thanks goes to *Dr. Shreyas Ramakrishna*, *Dr. Aloka Kumar Sahoo* and *Richard Bernecker* for generously dedicating their time to proofread my thesis. Their sharp corrections and insightful comments on technical phrasing greatly enhanced the quality of my thesis. Additionally, I deeply appreciate *Richard Bernecker* for his careful review of the abstract and his precise corrections to the German translation.

I would also like to express my heartfelt thanks to my friends, especially *Dr. Fang Liu* and *Joseph Andrews*, for making my time in Jena truly unforgettable. Their companionship, support, and countless shared moments turned challenges into adventures and made this journey all the more meaningful. Beyond academic pursuits, they helped create a home away from home. I must specially thank *Sumeet*, who was my first point of contact in Germany. From helping me navigate the initial culture shock to being a constant friend through visits to Erlangen, her support formed the foundation of my positive experience here.

Above all, I owe my deepest gratitude to my family, especially my parents, for their unconditional love and endless support throughout this journey. Their sacrifices paved the way for my education, their encouragement carried me through challenges, and their belief in me never wavered, even across continents. This achievement belongs as much to them as it does to me.

CONTENTS

LIST OF FIGURES

TOOLS AND METHODS

- This document was typeset in LaTex using the typographical look-and-feel `classicthesis` developed by André Miede and Ivo Pletikosić.
- Writefull language feedback tool was used to improve English grammar.
- The content of this thesis primarily encompasses analytical work. Wherever results are shown for specific physical parameters, computational tools have been employed to evaluate the respective analytical expressions for numerical values. In particular, Julia and Python were used for computation purposes and for creating all the plots in this thesis.
- Furthermore, most of the figures shown in this thesis have been edited using Inkscape v. 1.2.

1

INTRODUCTION

"Behind every atom of this world hides an infinite Universe."

— Rumi

1.1 BACKGROUND AND CONTEXT

Since the dawn of civilization, humanity has been driven by an intrinsic desire to comprehend the fundamental laws that govern the natural world. These principles not only dictate the behavior of natural phenomena but also shape the very fabric of our existence. By understanding these laws, we gain the ability to manipulate and harness natural processes, leading to innovations that simplify our lives and revolutionize the way we live. Central to many of these advancements is our ability to precisely control and engineer matter, enabling the development of transformative technologies that have reshaped society.

One of the most profound and effective methods for probing and manipulating matter at its most fundamental level is through the interaction of light and matter [1–5]. Among the various techniques available, *photoionization* stands out as a direct and powerful approach for investigating the electronic structure of atoms, molecules, and solid materials. This phenomenon, first explained by Albert Einstein in 1905 as part of his pioneering work on the photoelectric effect, describes the process by which matter absorbs photons—particles of light—and subsequently releases electrons [6]. This interaction results in the transformation of the matter into a charged, or ionic, state.

For photoionization to occur, the energy of the absorbed photon must exceed the binding energy that holds the electron within its atomic or molecular structure. When this condition is met, the electron is ejected, becoming what is known as a *photoelectron*. By analyzing the properties of these photoelectrons—such as their kinetic energy and angular distribution—we can extract critical insights into the electronic configuration

and behavior of the original material. This information is invaluable for understanding the fundamental properties of matter.

1.2 HISTORICAL DEVELOPMENT OF STRONG FIELD IONIZATION

The dynamics of interactions between atoms and photons are profoundly influenced by the energy of the incident photons in the applied radiation field. These interactions exhibit distinct behaviors depending on whether the photon energy $\hbar\omega$ exceeds or falls below the ionization potential I_p of the bound electron in an atom. Here $\hbar$ and ω are the Planck's constant and frequency of the photon respectively. When $\hbar\omega > I_p$, the process is dominated by *single-photon ionization*. In this regime, the kinetic energy E_k of the ejected electron is given by the relation

$$E_k = \hbar\omega - I_p.$$

This equation encapsulates the fundamental principle that the excess energy of the photon, beyond what is required to overcome the binding energy of the electron, is transferred to the electron as kinetic energy.

In contrast, when the photon energy $\hbar\omega$ is less than the ionization potential I_p, single-photon ionization is no longer possible. Instead, ionization can occur through the simultaneous absorption of multiple photons, a process known as *multi-photon ionization*. This concept was first theorized by Paul Dirac in 1927, who proposed that electrons could absorb multiple photons collectively to achieve the energy necessary for ionization [7]. Initially considered a theoretical curiosity, multi-photon ionization was later confirmed as a genuine physical phenomenon through experimental observations [8].

The probability of an atom absorbing n photons from a radiation field of intensity I, for each absorbed photon, is governed by the expression $P_n \propto \left(\frac{I}{I_{\text{a.u.}}}\right)^n$, where $I_{\text{a.u.}}$ is a characteristic value representing the intensity corresponding to the electric field that binds an electron in a Hydrogen atom. The minimum number of photons n_{th} required for ionization is determined by the threshold condition $n_{\text{th}} = \left\lfloor \frac{I_p}{\hbar\omega} \right\rfloor + 1$, where $\lfloor\cdot\rfloor$ represents the floor function. This equation highlights the nonlinear dependence of the ionization process on the intensity of the radiation field.

The advent of the Ruby laser in 1960, pioneered by Theodore Maiman [9], marked a turning point in the study of multi-photon processes [10]. The availability of intense, coherent laser sources enabled researchers to explore higher-order multi-photon ionization phenomena in greater detail. A landmark achievement in this field was the discovery of *above-threshold ionization* (ATI) by Agostini and colleagues in 1979 [11].

ATI occurs when an atom absorbs more photons than the minimum required for ionization, resulting in the emission of electrons with kinetic energies significantly higher than those predicted by simple perturbation theory [12]. The observation of ATI challenged the conventional understanding of multi-photon ionization, as it revealed the limitations of perturbative approaches in describing highly nonlinear processes [13]. While perturbation theory provides a useful framework for understanding low-order multi-photon interactions [14], it fails to account for the complex dynamics observed in experiments involving intense laser fields [15, 16]. Consequently, non-perturbative methods, such as the numerical solution of the time-dependent Schrödinger equation, have become essential for accurately modeling these phenomena [17–20].

The evolution of our understanding of atom-photon interactions underscores the intricate relationship between theory and experiment in advancing scientific knowledge. While early theoretical frameworks provided foundational insights, experimental breakthroughs often revealed new complexities that necessitated the development of more sophisticated models. The study of multi-photon ionization, in particular, exemplifies the interplay between nonlinear optical processes and quantum mechanical principles, offering a rich area of research with implications for fields ranging from atomic physics to quantum chemistry [21–26].

1.3 OVERVIEW OF STRONG FIELD IONIZATION

Strong-field ionization (SFI) is a fundamental process in atomic, molecular, and optical physics that occurs when an atom or molecule is exposed to an intense laser field, typically with electric field strengths comparable to the atomic unit ($50\,\mathrm{V/Å}$). In this regime, the electric field of the laser becomes strong enough to significantly distort the Coulomb potential binding the electron to the nucleus, leading to ionization through mechanisms such as tunneling or over-the-barrier escape. This phenomenon has profound implications for understanding light-matter interactions and has become a cornerstone of modern physics, enabling advancements in fields such as attosecond science, high-harmonic generation, and ultrafast spectroscopy.

The study of strong-field ionization is not only of theoretical interest but also has practical applications in areas such as laser technology, plasma physics, and quantum chemistry. By manipulating the intensity, wavelength, and duration of laser pulses, the ionization process can be control to explore the dynamics of electrons in atoms and molecules with unprecedented precision. This section provides an in-depth discussion of the fundamental principles underlying strong-field ionization and its diverse applications in modern physics.

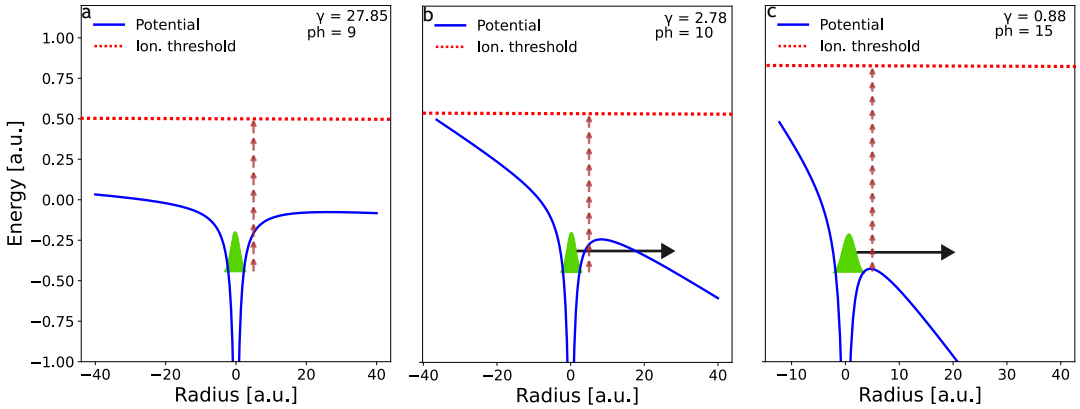

Figure 1.1: Schematic illustration of strong-field ionization mechanisms driven by a two-cycle circularly polarized 800 nm laser pulse. The blue lines depict the total potential, combining the Coulomb potential and the laser-induced potential at the peak electric field. The red dotted lines represent the ionization threshold, including the ponderomotive potential. The hydrogen 1*s* radial electron probability distribution (green), with its energy level aligned to the lower part of the potential well. Red arrows indicate the multi-photon ionization (MPI) process, illustrating the required photon absorption (ph) for ionization at varying intensities. (a) At an intensity of $8{\times}10^{11}$ W/cm^2 ($\gamma = 27.85$), ionization is dominated by MPI, as the potential barrier remains largely intact, suppressing tunneling. (b) For 8×10^{13} W/cm^2 ($\gamma = 2.78$), the potential barrier is significantly distorted, enabling tunneling ionization (black arrow), while additional photon absorption is required to surpass the ionization threshold. (c) At 8×10^{14} W/cm^2 ($\gamma = 0.88$), tunneling dominates, and MPI becomes negligible. The barrier is further suppressed, leading to over-the-barrier ionization (OBI) at higher intensities, where the electron escapes without tunneling, primarily near the peak laser intensity.

1.3.1 *Fundamental Principles*

The behavior of electrons in strong laser fields is governed by the interplay between the laser's electric field and the atomic or molecular potential. A key theoretical framework for understanding strong-field ionization is provided by the *Keldysh parameter* γ, a dimensionless quantity defined as [13]

$$\gamma = \sqrt{\frac{I_p}{2U_p}},$$

where I_p is the ionization potential of the atom or molecule, and U_p is the ponderomotive energy, which represents the cycled-average kinetic energy of an electron oscillating in the laser field. The Keldysh parameter distinguishes between three primary ionization regimes (see Fig. 1.1).

When $\gamma \gg 1$ (Fig.1.1a), the ionization process is dominated by the simultaneous absorption of multiple photons. This regime is characterized by a low-intensity laser field, where the photon energy $\hbar\omega$ is much smaller than the ionization potential I_p.

Multiphoton ionization was first observed experimentally in the 1960s and was theoretically explained by Keldysh, who developed a formalism to describe the transition from multiphoton to tunneling ionization [27]. MPI has been extensively studied in a variety of systems, including small molecules, clusters, and biomolecules, providing valuable insights into their electronic structures and dynamics [28–31].

For $\gamma \approx 1$ (Fig.1.1b), the electric field is strong enough to distort the atomic potential barrier, enabling the electron to tunnel through it. This phenomenon was first described by Fowler and Nordheim in the context of electron emission from metals [32] and was later extended to atoms and molecules through the development of the Ammosov-Delone-Krainov (ADK) theory [33, 34]. The ADK theory provides a semiclassical framework for calculating ionization rates in non-hydrogenic atoms, taking into account the effects of multiple electrons and atomic centers. Further refinements, such as the Keldysh-Faisal-Reiss (KFR) theory, incorporate additional factors like orbital geometry and atomic interactions, offering a more comprehensive understanding of ionization rates [13, 35, 36].

When the Keldysh parameter satisfies $\gamma \ll 1$ (Fig. 1.1c), the ionization process occurs predominantly via quantum tunneling through the laser-distorted potential barrier. In this regime, the laser field varies slowly compared to the electron's tunneling time, allowing the electron to escape even though the barrier remains finite. For a fixed intensity, this tunneling limit can be reached by decreasing the laser frequency (i.e., increasing the wavelength), without necessarily entering the over-the-barrier ionization (OBI) regime. Only when the electric field becomes sufficiently strong to suppress the potential barrier below the binding energy does OBI occur. Such extreme field conditions, often realized with few-femtosecond laser pulses, enable the study of ultrafast electron dynamics and non-thermal distributions, providing a deeper understanding of the underlying physical processes [37, 38].

1.3.2 *Applications in Modern Physics*

The study of strong-field ionization extends far beyond its theoretical foundations, offering a wealth of practical applications that have revolutionized our understanding of atomic and molecular systems. By subjecting matter to intense laser fields, researchers can explore regimes where traditional perturbative approaches fail, revealing new physical phenomena that are both complex and enlightening. Among these, ATI stands out as a cornerstone of strong-field physics, providing a unique lens through which to examine the nonlinear interaction between light and matter.

ATI occurs when an electron absorbs more photons than the minimum required for ionization, resulting in kinetic energies that exceed those predicted by conventional

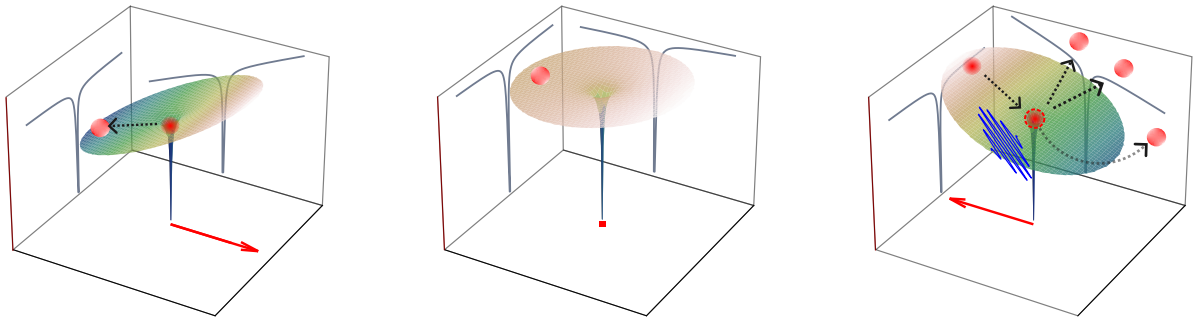

Figure 1.2: Three-step model of laser-induced ionization dynamics in krypton, modeled using a Coulombic binding potential $V(r) = -1/r$. The atom is exposed to an intense laser field of wavelength 800 nm and peak intensity 10^{14} W/cm^2. (Left) **Tunnel Ionization:** An electron (red dot) escapes the atomic potential well by tunneling through the laser-distorted potential barrier (red arrow). (Mid) **Propagation in the Continuum:** The ionized electron moves in the laser field, tracing a trajectory away from the nucleus. (Right) **Re-collision:** The electron may return to the nuclear vicinity, leading to processes such as High-Harmonic Generation (HHG), high-order ATI, or double ionization (multiple red dots), illustrating the intricate post-ionization dynamics.

models. This phenomenon challenges the simplistic view of ionization as a single-photon process and instead highlights the intricate dynamics of multi-photon absorption in strong laser fields. The study of ATI has not only deepened our understanding of quantum mechanics but has also paved the way for advancements in ultrafast spectroscopy and attosecond science. By analyzing the energy and angular distributions of photoelectrons, researchers can extract detailed information about the electronic structure and dynamics of atoms and molecules.

A particularly intriguing aspect of strong-field ionization is the role of recollision phenomena, where ionized electrons are driven back to their parent ions by the oscillating laser field. These recollisions give rise to a variety of effects that are well explained by the three-step model , proposed by Corkum in 1993, as show in Fig. 1.2. For example, laser-induced electron diffraction [39, 40] exploits the wave-like nature of recolliding electrons to create interference patterns that encode information about the spatial arrangement of atoms within a molecule. Similarly, electron holography [41] uses these interference effects to reconstruct detailed images of molecular structures, offering insights into processes such as chemical bonding and reaction dynamics.

Recollision also plays a central role in high-order above-threshold ionization (HATI), a process in which rescattered electrons gain additional energy through interactions with the parent ion. This results in photoelectrons with kinetic energies far beyond those predicted by simple tunneling models [42]. HATI provides a powerful platform for studying the non-perturbative nature of strong-field interactions, shedding light on the complex interplay between the laser field and the ionized electron. Additionally, recollision-driven processes such as non-sequential multiple ionization[43–

45] have revealed the correlated behavior of electrons in strong fields, where a single recolliding electron can liberate multiple electrons from the same ion. These findings have profound implications for understanding electron-electron interactions in complex systems.

While the primary focus of this thesis is on ATI phenomena, it is worth noting the broader impact of strong-field ionization on other areas of research. One such area is high-harmonic generation (HHG), a process in which recolliding electrons generate coherent radiation at integer multiples of the laser frequency. Although HHG is not the central theme of this work, it exemplifies the rich and diverse phenomena that arise from strong-field interactions. HHG has enabled the development of attosecond light sources, which are used to probe ultrafast electron dynamics in atoms, molecules, and solids [46–48]. The ability to control and observe electron dynamics on attosecond timescales has opened new frontiers in modern physics [49]. By leveraging the unique capabilities of strong-field ionization, researchers can probe ultrafast processes such as electron tunneling, wave packet dynamics, and molecular fragmentation with unprecedented precision. These advancements have far-reaching implications for fields such as quantum chemistry, materials science, and ultrafast optics, where understanding and manipulating electron behavior is essential for developing new technologies.

1.4 ABOVE-THRESHOLD IONIZATION: CONCEPTS AND SIGNIFICANCE

ATI is a fundamental phenomenon in strong-field physics that occurs when an atom or molecule absorbs more photons than the minimum number required for ionization. This process, first observed in the late 1970s, has since become a cornerstone in the study of light-matter interactions, particularly in the regime of intense laser fields. ATI provides critical insights into the dynamics of electrons under extreme electromagnetic conditions and has significant implications for understanding nonlinear optical processes, electron correlation, and quantum mechanics in intense fields.

1.4.1 *Experimental Observations and Implications*

The experimental discovery of ATI marked a turning point in the study of laser-atom interactions. Early experiments using intense laser pulses revealed that ionized electrons could be ejected with kinetic energies corresponding to the absorption of additional photons beyond the ionization threshold (see Fig. 1.3) [11, 50]. This observation contradicted the classical picture of photoionization, where electrons were expected to absorb only the minimum energy required to escape the atomic potential. Instead,

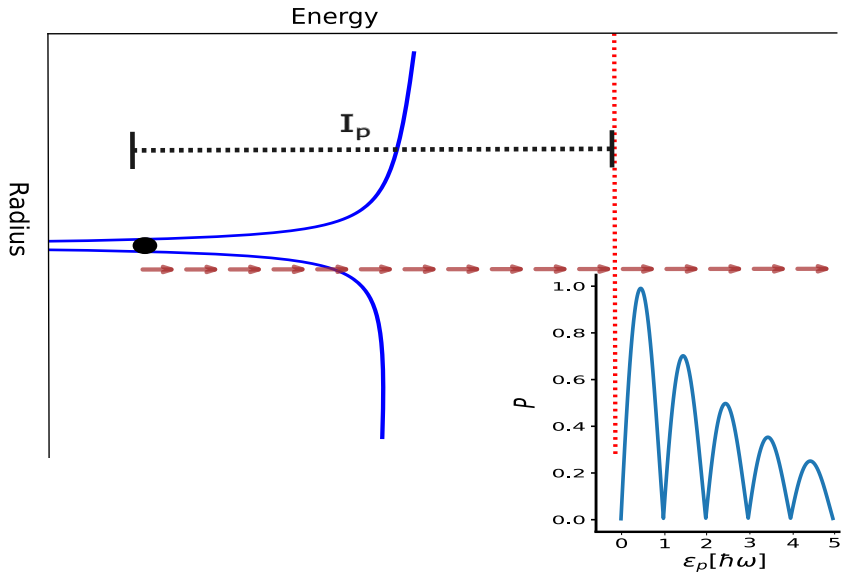

Figure 1.3: Potential energy curve and above-threshold ionization (ATI) spectrum of an Krypton atom in a strong laser field. The blue curve represents the atomic potential energy, while small red arrows indicate the absorption of photons enabling the electron to surpass the ionization potential (I_p). The inset displays the ATI spectrum, with peaks corresponding to the absorption of excess photons beyond I_p, measured in units of $\hbar\omega$.

the energy spectrum of emitted electrons exhibited discrete peaks, each separated by the photon energy of the incident laser field [51]. These peaks, known as ATI peaks, provided direct evidence of multiphoton processes in the strong-field regime [52].

The implications of ATI are profound. First, it demonstrated the breakdown of perturbation theory in intense laser fields, necessitating the development of non-perturbative theoretical frameworks. Second, ATI spectra serve as a sensitive probe of the laser field parameters, such as intensity, wavelength, and pulse duration, as well as the atomic or molecular structure [53–58]. For instance, the angular distribution of ATI electrons encodes information about the symmetry of the initial electronic state and the influence of the laser field on the ionization dynamics [59]. Furthermore, ATI has been instrumental in the development of attosecond science, as the high-energy electrons generated through ATI can be used to probe ultrafast processes in atoms, molecules, and solids.

Recent advances in experimental techniques, such as velocity map imaging and coincidence spectroscopy, have enabled detailed measurements of ATI spectra with unprecedented resolution [60, 61]. These experimental techniques have revealed subtle features, such as low-energy structures and rescattering plateaus, which have deepened our understanding of strong-field ionization mechanisms [42, 62]. Moreover, ATI has found practical applications in the generation of high-harmonic radiation

and the development of compact electron accelerators, highlighting its significance beyond fundamental research.

1.4.2 *Theoretical Approaches of ATI*

The theoretical description of ATI is rooted in quantum mechanics and the interaction of atoms with intense electromagnetic fields. Two primary models have been developed to explain ATI: the *strong-field approximation* (SFA) and the *semiclassical recollision model*. These approaches provide complementary insights into the underlying physics of ATI, enabling researchers to interpret experimental observations and refine theoretical frameworks.

The strong-field approximation, also known as the Keldysh-Faisal-Reiss theory, treats the laser field as a classical electromagnetic wave and describes the ionization process using time-dependent perturbation theory. In this model, the electron is assumed to be instantaneously liberated from the atomic potential via tunneling ionization, after which it propagates as a free particle in the laser field. The SFA successfully predicts the existence of ATI peaks and their dependence on laser parameters, such as intensity and wavelength [63–65]. However, it neglects the influence of the atomic potential on the ejected electron, which can lead to discrepancies with experimental observations, particularly in the low-energy regime [66, 67].

The semiclassical recollision model as shown in Fig. 1.2, often associated with high-harmonic generation (HHG), also provides valuable insights into ATI. While the three-step model is more commonly used to describe HHG, it can be adapted to explain certain aspects of ATI [68, 69], particularly the rescattering mechanism [70]. In this model, the ionization process is divided into three steps: (1) *tunneling ionization*, where the electron escapes the atomic potential through the barrier suppressed by the laser field; (2) *acceleration in the laser field*, where the electron gains energy from the oscillating electric field; and (3) *recollision*, where the electron may return to the parent ion. In the context of ATI, recollision can lead to elastic or inelastic scattering, contributing to the high-energy plateau observed in ATI spectra. However, the primary focus of the three-step model remains on HHG and other higher-order processes.

Both the SFA and recollision models have been extended and refined to incorporate additional effects, such as Coulomb focusing, quantum interference, and multielectron dynamics [71–75]. For instance, the inclusion of the Coulomb potential in the SFA has significantly improved its agreement with experimental data, particularly for low-energy electrons. Furthermore, advanced numerical methods, such as *time-dependent density functional theory* (TDDFT) and solutions to the *time-dependent Schrödinger equation* (TDSE), have enabled precise simulations of ATI in complex systems. The SFA

is employed in this thesis due to its computational efficiency and ability to provide physical insight into strong-field ionization dynamics while maintaining reasonable agreement with experimental observations.

MOTIVATION FOR THE STUDY

The study of strong-field ionization and ATI lies at the heart of modern atomic, molecular, and optical physics. As laser technology continues to advance, enabling the generation of ultrashort and high-intensity pulses, the interaction of light with matter has entered a regime where traditional perturbative approaches no longer suffice. Understanding the dynamics of electrons in such intense fields is not only a fundamental scientific challenge but also a gateway to groundbreaking applications in ultrafast science, attosecond physics, and laser-driven particle acceleration.

One of the primary motivations for this research is the need to unravel the complex mechanisms underlying strong-field ionization. The ATI process provides a unique window into the quantum dynamics of electrons in extreme electromagnetic environments. By studying ATI, we gain insights into the interplay between quantum mechanics and classical electrodynamics, as well as the role of electron correlation and nondipole effects in ionization processes.

From a practical perspective, the implications of strong-field ionization extend far beyond fundamental physics. ATI plays a crucial role in the generation of high-harmonic radiation, which is the foundation of attosecond science. Attosecond pulses, in turn, enable the real-time observation of electron dynamics in atoms, molecules, and solids, opening new frontiers in ultrafast spectroscopy and imaging. Furthermore, the high-energy electrons produced through ATI have potential applications in compact electron accelerators and advanced radiation sources, which could revolutionize fields such as materials science, chemistry, and medicine.

Another key motivation for this study is the exploration of structured light, particularly twisted light beams, in strong-field processes. Unlike conventional plane waves, twisted light carries orbital angular momentum, offering new degrees of freedom for controlling ionization dynamics. Understanding how such structured light interacts with matter could lead to novel techniques for manipulating electron motion and designing tailored laser-matter interactions. This has implications for quantum information processing, precision metrology, and the development of next-generation optical technologies.

Finally, this research is driven by the desire to bridge the gap between theory and experiment. While significant progress has been made in understanding strong-field ionization, many questions remain unanswered. For instance, the role of nondipole ef-

fects, the influence of laser pulse parameters, and the behavior of electrons in complex systems are areas that require further exploration. Nondipole effects emerge from the spatial variation of the laser field, where the magnetic component exerts a Lorentz force on the ionized electron. By developing advanced theoretical models and numerical techniques, this thesis aims to provide a deeper understanding of these phenomena and offer predictions that can guide future experimental investigations.

In summary, the motivation for this study is multifaceted, encompassing both fundamental scientific inquiry and practical applications. By advancing our understanding of strong-field ionization and ATI, this research contributes to the broader goals of ultrafast and high-intensity laser physics, paving the way for understanding the ionization in greater details.

1.5 STRUCTURE OF THE THESIS

This thesis is systematically organized into several chapters, each dedicated to exploring a critical aspect of strong-field ionization. The progression of the chapters is designed to guide the reader from foundational concepts to advanced theoretical frameworks, numerical methodologies, and discussions on experimental relevance and future prospects. Below is an overview of the structure and content of each chapter.

In Chapters 2 and 3, we establish the theoretical framework for strong-field ionization. Chapter 2 begins with an overview of electromagnetic waves, covering Maxwell's equations, plane-wave solutions, and the distinctive features of twisted light beams in strong-field processes. Chapter 3 then introduces the strong-field approximation as a key theoretical approach, elaborating on dipole and nondipole effects, as well as the role of the Lorentz force in ionization dynamics. Additionally, the chapter examines different gauge formulations, laying a rigorous foundation for the analysis of laser-atom interactions.

Chapter 4 focuses on the mathematical and computational techniques employed in this research. The Jacobi-Anger expansion is introduced as a powerful method for analyzing twisted wavefields. The saddle point approximation (SPA) is discussed in detail, including its derivation, validity, and limitations. The chapter also covers the numerical implementation of saddle point equations, utilizing root-finding algorithms and iterative methods. Additionally, computational techniques for calculating photoelectron momentum distributions are presented, providing a bridge between theory and numerical results.

Chapter 5 presents the core findings of this research, offering a detailed exploration of various aspects of ATI. Topics include ionization dynamics in few-cycle laser pulses, the role of ellipticity in saddle point solutions, and nonlinear interference effects in

ATI peaks and momentum distributions. Nondipole effects and their dependence on laser pulse parameters are analyzed, alongside the interaction of twisted light with atoms and its impact on ATI peak positions. The chapter also examines asymmetries in photoelectron momentum distributions, providing insights into their dependence on laser characteristics. These results are discussed in the context of both theoretical predictions and experimental observations.

The final chapter summarizes the key contributions of this thesis to the field of strong-field ionization. It highlights the implications of the findings for ultrafast and high-intensity laser physics. The chapter concludes with a forward-looking perspective, proposing future research directions.

2

LIGHT FIELD AND ITS PROPERTIES

The study of light fields is central to understanding strong field ionization, a process in which atoms or molecules are ionized by intense laser fields. This chapter provides a foundation for the interaction of light with matter, starting with Maxwell's equations, which govern the behavior of electromagnetic waves. We then discuss plane waves, twisted light beams, few-cycle pulses, and the role of the carrier-envelope phase, all of which are critical for modeling and interpreting strong field ionization experiments.

2.1 MAXWELL'S EQUATIONS AND ELECTROMAGNETIC WAVES

The interaction of intense laser fields with atomic systems demands a robust and comprehensive mathematical framework, which is elegantly provided by Maxwell's equations [76]. These equations serve as the cornerstone for describing the behavior of electromagnetic fields in a vacuum and are indispensable for understanding the intricate dynamics of light. In the absence of external charges or currents, the electric field $\mathbf{E}(\mathbf{r},t)$ and the magnetic field $\mathbf{B}(\mathbf{r},t)$ satisfy the following set of conditions, derived directly from Maxwell's equations [77]

$$\nabla \cdot \mathbf{E}(\mathbf{r},t) = 0, \tag{2.1}$$

$$\nabla \times \mathbf{E}(\mathbf{r},t) = -\frac{\partial \mathbf{B}(\mathbf{r},t)}{\partial t}, \tag{2.2}$$

$$\nabla \cdot \mathbf{B}(\mathbf{r},t) = 0, \tag{2.3}$$

$$\nabla \times \mathbf{B}(\mathbf{r},t) = \frac{1}{c^2}\frac{\partial \mathbf{E}(\mathbf{r},t)}{\partial t}, \tag{2.4}$$

where c represents the speed of light in a vacuum. For practical applications, particularly in computational modeling, it is often advantageous to express the electric and magnetic fields in terms of scalar and vector potentials, denoted as $\phi(\mathbf{r},t)$ and $\mathbf{A}(\mathbf{r},t)$, respectively. These potentials are defined as follows:

$$\mathbf{E}(\mathbf{r},t) = -\nabla\phi(\mathbf{r},t) - \frac{\partial \mathbf{A}(\mathbf{r},t)}{\partial t}, \qquad \mathbf{B}(\mathbf{r},t) = \nabla \times \mathbf{A}(\mathbf{r},t). \tag{2.5}$$

Although the physical fields $\mathbf{E}(\mathbf{r}, t)$ and $\mathbf{B}(\mathbf{r}, t)$ are uniquely determined by the potentials $\phi(\mathbf{r}, t)$ and $\mathbf{A}(\mathbf{r}, t)$, the potentials themselves are not unique due to the inherent gauge freedom in the theory. This freedom allows for the introduction of an arbitrary scalar function, known as the gauge function $\lambda(\mathbf{r}, t)$, which can be used to redefine the potentials without altering the physical fields. The gauge transformations are given by:

$$\phi'(\mathbf{r}, t) = \phi(\mathbf{r}, t) - \frac{\partial \lambda(\mathbf{r}, t)}{\partial t}, \tag{2.6}$$

$$\mathbf{A}'(\mathbf{r}, t) = \mathbf{A}(\mathbf{r}, t) + \nabla \lambda(\mathbf{r}, t). \tag{2.7}$$

These transformations, known as gauge transformations, leave the physical fields invariant and play a pivotal role in various branches of physics. To uniquely specify the potentials, additional constraints, known as gauge conditions, must be imposed. One of the most commonly used gauges in electrodynamics is the Coulomb gauge, defined by the following conditions:

$$\nabla \cdot \mathbf{A}(\mathbf{r}, t) = 0, \qquad \phi(\mathbf{r}, t) = 0. \tag{2.8}$$

In the Coulomb gauge, the scalar potential $\phi(\mathbf{r}, t)$ is eliminated due to the absence of free charges, simplifying Maxwell's equations significantly. Under this gauge, the vector potential $\mathbf{A}(\mathbf{r}, t)$ satisfies the wave equation

$$\nabla^2 \mathbf{A}(\mathbf{r}, t) - \frac{1}{c^2} \frac{\partial^2 \mathbf{A}(\mathbf{r}, t)}{\partial t^2} = 0. \tag{2.9}$$

Electromagnetic waves in a vacuum can be represented as a superposition of monochromatic waves, each of which is a solution to the wave equation. For a monochromatic vector potential corresponding to a single light wave, the solution can be expressed as:

$$\mathbf{A}(\mathbf{r}, t) = \Re \left[\mathbf{A}(\mathbf{r}) e^{-i\omega t} \right], \tag{2.10}$$

where ω is the angular frequency of the wave and $\Re$ stands for Real. Substituting this form into the wave equation yields the Helmholtz equation for the vector potential

$$(\nabla^2 + k^2)\mathbf{A}(\mathbf{r}) = 0, \tag{2.11}$$

where $k = \omega/c$ is the wave number. The wave number k is related to the momentum of the electromagnetic wave, and the momentum operator in quantum mechanics is

given by $\mathbf{p} = -i\hbar\nabla$. The spatial structure of the vector potential $\mathbf{A}(\mathbf{r})$ plays a crucial role in determining the characteristics of the associated laser fields.

If $\mathbf{A}(\mathbf{r})$ is spatially constant, implying no spatial variation, the derived momentum $\mathbf{pA}(\mathbf{r}) = k\mathbf{A}(\mathbf{r})$ vanishes, leading to $k = 0$. This scenario results in an unphysical situation where the magnetic field disappears entirely. To address spatially structured light fields formally, we refer to the definition of the wave number and the dispersion relation $k = \omega/c$, which ensures that oscillating light fields cannot maintain a consistent spatial structure across different media.

In many practical scenarios, particularly in the study of atom-light interactions, the spatial dependence of the fields is often negligible. This simplification leads to the use of the dipole approximation. While this approximation is valid under certain conditions, it can break down in situations where the effects of magnetic fields or photon momentum become significant. These considerations are critical and must be carefully accounted for in both classical electrodynamics and quantum mechanics.

2.2 PLANE WAVES SOLUTION

The vector potential $\mathbf{A}(\mathbf{r})$ for a transverse plane wave is a fundamental solution to the Helmholtz equation, as presented in Eq. 2.11. It is expressed in the following form

$$\mathbf{A}(\mathbf{r}) = A_0\, e^{i\mathbf{k}\cdot\mathbf{r}}\, \boldsymbol{\epsilon}, \tag{2.12}$$

where A_0 represents the amplitude of the electromagnetic field, $\mathbf{k} = k\mathbf{e}_z$ is the wave vector pointing in the z-direction, and $\boldsymbol{\epsilon}$ is the polarization vector. The polarization vector is defined as

$$\boldsymbol{\epsilon} = \frac{1}{\sqrt{1+\varepsilon^2}}(\mathbf{e}_z + i\varepsilon\mathbf{e}_y). \tag{2.13}$$

Here, ε quantifies the ellipticity of the plane wave, and λ denotes its helicity. This dissertation primarily focuses on transverse plane waves, often referred to simply as "plane waves." These waves are characterized by their wavelength λ, field amplitude A_0, and ellipticity ε. The intensity of the field is a critical property of plane waves and can be calculated using the cycle-averaged Poynting vector [78], defined as

$$\mathbf{P} = \frac{1}{\mu_0}\mathbf{E}(\mathbf{r},t) \times \mathbf{B}(\mathbf{r},t). \tag{2.14}$$

The corresponding intensity is given by:

$$I(\mathbf{r},t) = \frac{1}{T}\left|\int_t^{t+T} d\tau\, \mathbf{P}(\mathbf{r},t)\right|, \tag{2.15}$$

which evaluates to

$$I(\mathbf{r},t) = \frac{A_0^2\omega^3 c}{8\pi^2(1+\varepsilon^2)}\int_t^{t+T} d\tau \left(\sin^2(kz-\omega t) + \varepsilon^2\cos^2(kz-\omega t)\right) = \frac{A_0^2\omega^2 c}{8\pi}. \tag{2.16}$$

Under the Coulomb gauge, the cycle-averaged intensity simplifies significantly. In this gauge, the electric field amplitude is constrained to $E_0 = -A_0\omega$, assuming the electric and magnetic fields are derived from Eqs. 2.5 and 2.8.

For more complex scenarios, such as the superposition of plane-wave beams [79, 80], it is advantageous to generalize the definition of the vector potential using an orthonormal basis $\{\mathbf{e}_1, \mathbf{e}_2, \mathbf{e}_k\}$. A general monochromatic plane wave is defined as

$$\mathbf{A}(\mathbf{r},t) = \Re\left[A_0 e^{i(\mathbf{r}\cdot\mathbf{k}-\omega t)}\boldsymbol{\epsilon}\right], \tag{2.17}$$

where $\boldsymbol{\epsilon}$ is the complex polarization vector. We choose an orthonormal basis $\{\mathbf{e}_1, \mathbf{e}_2, \mathbf{e}_k\}$, where $\mathbf{e}_k = \hat{\mathbf{k}}$, such that the polarization vector $\boldsymbol{\epsilon}$ is given by Eq. 2.13. With this generalization, the full vector potential corresponding to Eq. 2.17 can be written as

$$\mathbf{A}(\mathbf{r},t) = \frac{A_0}{\sqrt{1+\varepsilon^2}}\left(\cos(\mathbf{k}\cdot\mathbf{r}-\omega t)\mathbf{e}_1 - \varepsilon\Lambda\sin(\mathbf{k}\cdot\mathbf{r}-\omega t)\mathbf{e}_2\right). \tag{2.18}$$

To gain deeper physical insight, it is useful to focus on the case of circular polarization ($\varepsilon = 1$) and explore the significance of the helicity parameter Λ. Matula et al. [81] describe the propagation direction of a plane-wave beam using the unit wave vector

$$\mathbf{e}_k = \begin{pmatrix} \sin\vartheta_k\cos\varphi_k \\ \sin\vartheta_k\sin\varphi_k \\ \cos\vartheta_k \end{pmatrix}, \tag{2.19}$$

where ϑ_k and φ_k denote the polar and azimuthal angles of the wave vector $\mathbf{k}$, respectively. In accordance with the Coulomb gauge condition $\boldsymbol{\epsilon}\cdot\mathbf{k} = 0$, the polarization vector remains perpendicular to the wave vector and is expressed as:

$$\boldsymbol{\epsilon}_{k\Lambda} = -\frac{\Lambda}{\sqrt{2}}\begin{pmatrix} \cos\vartheta_k\cos\varphi_k - i\Lambda\sin\varphi_k \\ \cos\vartheta_k\sin\varphi_k + i\Lambda\cos\varphi_k \\ -\sin\vartheta_k \end{pmatrix}. \tag{2.20}$$

To facilitate further analysis, the polarization vector is often expanded in terms of spin-momentum basis states:

$$\boldsymbol{\epsilon}_{k\Lambda} = \sum_{m_s=0,\pm1} c_{m_s} e^{-im_s\varphi_k} \boldsymbol{\eta}_{m_s}, \tag{2.21}$$

where the eigenstates of the spin operator $\hat{S}_z$ satisfy:

$$\hat{S}_z \boldsymbol{\eta}_{m_s} = m_s \boldsymbol{\eta}_{m_s}, \quad \boldsymbol{\eta}_{\pm1} = \frac{\pm1}{\sqrt{2}} \begin{pmatrix} 1 \\ \pm i \\ 0 \end{pmatrix}, \quad \boldsymbol{\eta}_0 = \begin{pmatrix} 0 \\ 0 \\ 1 \end{pmatrix}. \tag{2.22}$$

The expansion coefficients are given by $c_0 = \frac{\Lambda}{\sqrt{2}} \sin\vartheta_k$ and $c_{\pm1} = \frac{1}{2}(1 \pm \Lambda \cos\vartheta_k)$. By setting $\vartheta_k = 0$ and $\varphi_k = 0$, the wave vector aligns with the optical axis (z-axis), and the helicity Λ corresponds to the photon's spin projection onto its momentum direction [81].

In the case of elliptically polarized laser fields ($\varepsilon \neq 1$), such fields can be decomposed into a superposition of circularly polarized plane waves. Although the spin-photon interpretation originates from circular polarization, it remains valid for more generalized elliptically polarized waves.

In summary, monochromatic plane-wave beams are characterized by their wavelength $\lambda = 2\pi c/\omega$, helicity $\Lambda = \pm1$, ellipticity $0 \leq \varepsilon \leq 1$, and intensity I. These properties provide a comprehensive framework for analyzing and understanding the behavior of plane waves in various physical contexts.

2.3 TWISTED LIGHT BEAMS: ORBITAL ANGULAR MOMENTUM AND PHASE STRUCTURE

While plane waves represent the simplest form of electromagnetic waves, their structure is limited in complexity. In contrast, twisted light beams exhibit a richer spatial profile, characterized by helical phase fronts that rotate around the propagation axis. These beams carry not only spin angular momentum (SAM) but also orbital angular momentum (OAM), making them a fascinating subject of study in modern optics. Among these, Bessel beams stand out as a unique class of non-diffractive solutions to the wave equation, offering intriguing properties and applications.

Bessel beams are monochromatic solutions to the wave equation, derived from the Helmholtz equation. Unlike plane waves, Bessel beams are eigenfunctions of the to-

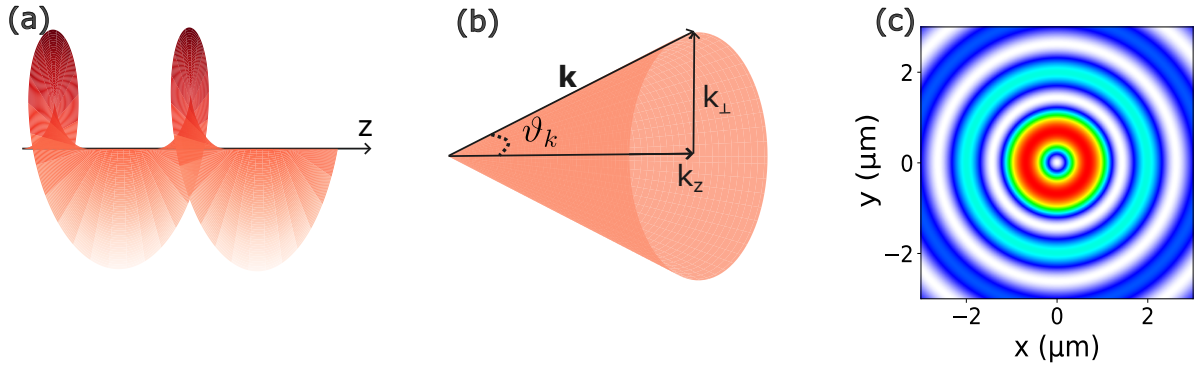

Figure 2.1: Illustration of the properties of Bessel beams. (a) The phase fronts of the beam exhibit a helical structure, spiraling around the central axis. (b) A Bessel beam is generated through the superposition of circularly polarized plane waves, with wave vectors $\mathbf{k}$ distributed on a conical surface defined by the angle $\vartheta_k = \arctan(\varkappa/k_z)$. (c) The transverse intensity distribution of a Bessel beam displays a central null intensity at the beam axis ($x = y = 0$) and an infinite series of concentric rings. The intensity profile is normalized to the maximum intensity for a beam with parameters $\lambda = 800\,\text{nm}$, $\vartheta_k = 20°$, $\Lambda = +1$, and $m_\gamma = 2$.

tal angular momentum (TAM) operator $\hat{J}_z$, which combines spin and orbital angular momentum $\hat{J}_z = \hat{S}_z + \hat{L}_z, \quad \text{with} \quad \hat{L}_z = -i\frac{\partial}{\partial\varphi}$. The eigenvalue equation for the TAM operator is given by

$$\hat{J}_z\mathbf{A}(\mathbf{r}) = m_\gamma\mathbf{A}(\mathbf{r}), \tag{2.23}$$

where m_γ represents the total angular momentum projection of the beam. Additionally, Bessel beams possess a well-defined longitudinal momentum component k_z, satisfying:

$$\hat{p}_z^2\mathbf{A}(\mathbf{r}) = k_z^2\mathbf{A}(\mathbf{r}). \tag{2.24}$$

The transverse momentum modulus $k_\perp$ is related to the total wave number k and the longitudinal component k_z by $k_\perp = |\mathbf{k}_\perp| = \varkappa = \sqrt{k^2 - k_z^2}$. This relationship ensures that the wave vectors $\mathbf{k}$ of the plane wave lie on a cone in momentum space, with an opening angle $\vartheta_k = \arctan(k_\perp/k_z)$.

The vector potential $\mathbf{A}(\mathbf{r})$ of a Bessel beam can be constructed as a superposition of circularly polarized plane waves. Each plane-wave component is weighted by an amplitude function $a_{\varkappa m_\gamma}(\mathbf{k}_\perp)$, which depends on the transverse momentum $\mathbf{k}_\perp$ and the TAM projection m_γ. The general form of the vector potential is

$$\mathbf{A}(\mathbf{r}) = \frac{A_0}{(2\pi)^2}\int \mathrm{d}^2k_\perp\, a_{\varkappa m_\gamma}(k_\perp)\,\boldsymbol{\epsilon}_{k\Lambda}\,e^{i\mathbf{k}\cdot\mathbf{r}}, \tag{2.25}$$

where $\epsilon_{k\Lambda}$ is the polarization vector for helicity $\Lambda = \pm 1$. The amplitude function is given by

$$a_{\varkappa m_\gamma}(\mathbf{k}_\perp) = \sqrt{\frac{2\pi}{\varkappa}}(-i)^{m_\gamma} e^{i m_\gamma \varphi_k} \delta(k_\perp - \varkappa). \tag{2.26}$$

Here, the Dirac delta function $\delta(k_\perp - \varkappa)$ ensures that all contributing wave vectors lie on the momentum cone, as shown in Fig. 2.1(b).

In position space, the vector potential $\mathbf{A}(\mathbf{r})$ is expressed in cylindrical coordinates (r, φ_r, z) using Bessel functions of the first kind, $J_n(x)$. The expansion of $\mathbf{A}(\mathbf{r})$ in terms of spin-momentum eigenstates $\boldsymbol{\eta}_{m_s}$ yields

$$\mathbf{A}(\mathbf{r}) = \sum_{m_s=0,\pm 1} A_{m_s}(\mathbf{r}) \boldsymbol{\eta}_{m_s}, \tag{2.27}$$

where the components $A_{m_s}(\mathbf{r})$ are given by

$$A_{m_s}(\mathbf{r}) = \sqrt{\frac{\varkappa}{2\pi}}(-i)^{m_s} c_{m_s} J_{m_\gamma - m_s}(\varkappa r) e^{i(m_\gamma - m_s)\varphi_r} e^{i k_z z}. \tag{2.28}$$

This representation highlights the helical phase structure of Bessel beams, with the phase fronts determined by the exponential term $(m_\gamma - m_s)\varphi_r + k_z z$. The intensity profile of a Bessel beam is derived from the longitudinal component of the Poynting vector $\mathbf{S}(\mathbf{r}, t)$. The transverse intensity distribution $I_\perp(\mathbf{r})$ is given by [82]

$$I_\perp(\mathbf{r}) = \frac{\omega^2 \varkappa}{4\pi} \left| c_{+1}^2 J_{m_\gamma - 1}^2(\varkappa r) - c_{-1}^2 J_{m_\gamma + 1}^2(\varkappa r) \right|. \tag{2.29}$$

This expression reveals the non-diffractive nature of Bessel beams, as their intensity profile remains invariant along the propagation axis, as illustrated in Fig. 2.1(c). Mathematically, the characteristic ring-like structure of the intensity distribution arises from the properties of Bessel functions.

In the paraxial regime, where the transverse momentum $k_\perp$ is much smaller than the longitudinal component k_z, the vector potential simplifies significantly. Under this approximation, only the term with $m_s = \Lambda$ contributes, leading to

$$\mathbf{A}(\mathbf{r}) \approx \sqrt{\frac{\varkappa}{2\pi}}(-i)^{\Lambda} c_\Lambda J_{m_\gamma - \Lambda}(\varkappa r) e^{i(m_\gamma - \Lambda)\varphi_r} e^{i k_z z} \boldsymbol{\eta}_\Lambda. \tag{2.30}$$

This form explicitly demonstrates the separation of spin and orbital angular momentum in the paraxial limit

$$\hat{S}_z\, \mathbf{A}(\mathbf{r}) = \Lambda\, \mathbf{A}(\mathbf{r}), \qquad \hat{L}_z\, \mathbf{A}(\mathbf{r}) = (m_\gamma - \Lambda)\, \mathbf{A}(\mathbf{r}). \tag{2.31}$$

The term $m_l = m_\gamma - \Lambda$ corresponds to the orbital angular momentum of the beam, which arises from the helical phase structure of the wavefronts. The phase fronts of the beam are determined by the equation $(m_\gamma - \Lambda)\varphi_k + k_z z = \text{const.}$ where φ_k is the azimuthal angle in momentum space. This equation describes the helical structure of the wavefronts, as illustrated in Fig. 2.1(a). In the limit where the opening angle approaches to zero ($\theta_k \to 0$), the Bessel beam reduces to a plane wave with circular polarization ($\varepsilon = 1$).

In the study of ATI processes driven by Bessel beams, it is often necessary to work with a real-valued expression for the vector potential. Conventionally, the imaginary part of the complex vector potential is used in the literature for twisted light beams [83, 84]. This choice does not affect the physical interpretation of the results and is adopted here for consistency. The Cartesian components of the real-valued vector potential are derived as follows [85]

$$\begin{aligned}
A_x(\mathbf{r},t) &= \sqrt{\frac{\varkappa}{4\pi}}\Big[c_{-1}J_{m_\gamma+1}(\varkappa r)\cos\left((m_\gamma+1)\varphi_r + k_z z - \omega t\right) \\
&\quad + c_{+1}J_{m_\gamma-1}(\varkappa r)\cos\left((m_\gamma-1)\varphi_r + k_z z - \omega t\right)\Big], \\
A_y(\mathbf{r},t) &= \sqrt{\frac{\varkappa}{4\pi}}\Big[c_{-1}J_{m_\gamma+1}(\varkappa r)\sin\left((m_\gamma+1)\varphi_r + k_z z - \omega t\right) \\
&\quad - c_{+1}J_{m_\gamma-1}(\varkappa r)\sin\left((m_\gamma-1)\varphi_r + k_z z - \omega t\right)\Big], \\
A_z(\mathbf{r},t) &= \sqrt{\frac{\varkappa}{2\pi}}c_0 J_{m_\gamma}(\varkappa r)\sin\left(m_\gamma\varphi_r + k_z z - \omega t\right).
\end{aligned} \tag{2.32}$$

These expressions describe the spatial and temporal evolution of the vector potential in Cartesian coordinates. The terms c_{-1}, c_{+1}, and c_0 are coefficients that depend on the spin and orbital angular momentum properties of the beam, while $J_n(x)$ represents the Bessel functions of the first kind. The helical phase structure of the beam is evident in the trigonometric terms, which depend on the azimuthal angle φ_r and the propagation coordinate z. The definitions of all the coefficients used above are provided in the Appendix A.4.

In summary, Bessel beams are characterized by their wavelength λ, opening angle ϑ_k, helicity Λ, total angular momentum projection m_γ, and amplitude A_0. These parameters determine the spatial and temporal properties of the beam, including its intensity profile and phase structure.

2.4 FEW-CYCLE PULSES: TEMPORAL AND SPECTRAL PROPERTIES

In experimental and theoretical studies of light-matter interactions, laser pulses of finite duration are often employed instead of continuous-wave (CW) laser fields. Finite-

duration laser pulses are used because they allow for precise temporal control of light-matter interactions, enabling studies of ultrafast dynamics (e.g., electron motion, molecular vibrations, and chemical reactions) that occur on femtosecond or picosecond timescales. Unlike CW lasers, which are described by time-independent solutions to the wave equation, finite-duration pulses introduce a temporal dependence to the laser intensity. As illustrated in Fig. 2.2, the left panel shows the time-domain representations of laser pulses with different cycle durations (2, 4, and 8 cycles). The corresponding frequency spectra, depicted in the right panel, demonstrate how shorter pulses result in broader frequency distributions, whereas longer pulses exhibit narrower spectral bandwidths. This temporal variation is critical in processes that are highly sensitive to changes in laser intensity, such as ATI and HHG.

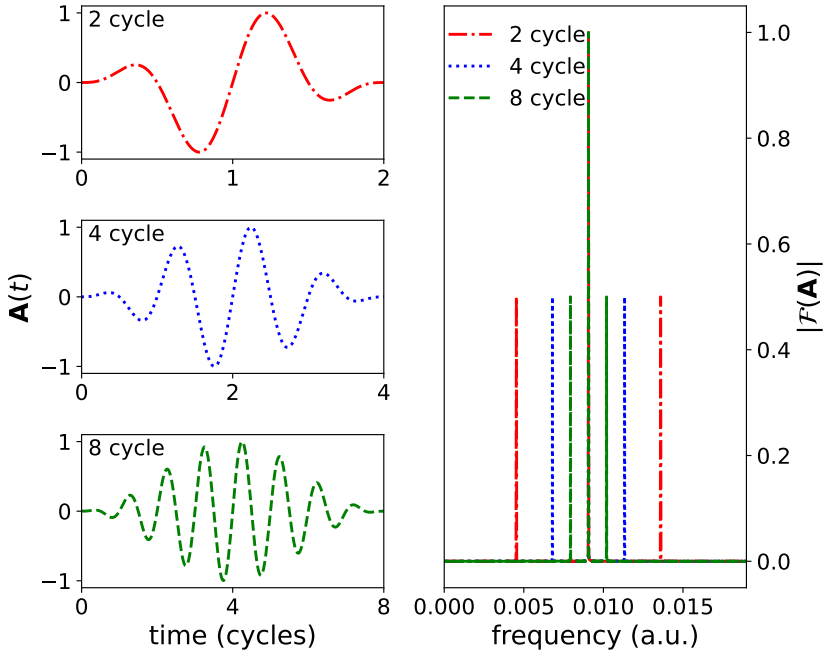

Figure 2.2: Time-domain representation of the total vector potential $\mathbf{A}(t)$ for a circularly polarized plane wave laser pulse is shown in the left panels, while in the right panel its corresponding frequency-domain representation, $[\mathcal{F}(\mathbf{A})](\omega)$. The plots include laser pulses with durations of two (red), four (blue), and eight (green) optical cycles, with a carrier-envelope phase of $\varphi_{\text{cep}} = 0$ and a wavelength of 800 nm. The right panel's vertical axis represents the absolute amplitude of the vector potential at a peak intensity of 5×10^{14} W/cm^2.

The vector potential $\mathbf{A}^{(P)}(\mathbf{r}, t)$ of a finite-duration laser pulse can be constructed by modifying the plane-wave solution with an envelope function $f(t)$. This approach, as proposed by Milošević et al. [86], ensures that the pulse has a well-defined duration and temporal profile. To describe the temporal profile of the laser pulse, an envelope function $f(t)$ is introduced. A commonly used envelope function is the sine-squared

profile, which provides a smooth rise and fall of the pulse intensity. This function is defined as

$$f(t) = \begin{cases} \sin^2\left(\frac{\omega t}{2n_p}\right), & 0 \leq t \leq \tau_p, \\ 0, & \text{otherwise}, \end{cases} \tag{2.33}$$

where τ_p is the total duration of the pulse, and n_p represents the number of optical cycles within the pulse. The pulse duration is related to the number of cycles by $\tau_p = n_p T$, where $T = 2\pi/\omega$ is the period of one optical cycle. The sine-squared envelope ensures that the pulse intensity smoothly transitions from zero to its maximum value and back to zero, minimizing abrupt changes that could lead to unwanted spectral broadening. In the limit of an infinitely long pulse ($n_p \to \infty$), the envelope function $f(t)$ approaches unity for all times t. In this case, the vector potential of a pulse reduces to the plane-wave solution.

In this chapter, we have formally defined the properties of the light field and derived the mathematical representations for plane waves, Bessel beams, and their corresponding pulsed variants. These formulations provide the foundation for our subsequent analysis. In the next chapter, we will apply these definitions to compute the Volkov phase—a key component in strong-field quantum electrodynamics. Specifically, we will derive explicit expressions for the Volkov phase using the field structures introduced here, enabling a rigorous treatment of electron dynamics in intense laser fields.

3

THE STRONG FIELD APPROXIMATION

In this chapter, we provide a comprehensive overview of the Strong Field Approximation, a theoretical framework widely used to model ionization processes in the presence of intense laser fields. The SFA simplifies the description of electron dynamics by neglecting the Coulomb interaction between the ionized electron and the parent ion after the ionization event. This approximation has proven to be highly effective in explaining key phenomena observed in above-threshold ionization, high-harmonic generation, and nonsequential double ionization.

We begin by outlining the theoretical foundations of the SFA, including its derivation and the assumptions underlying its formulation. The standard approach to the SFA is based on the dipole approximation, which is valid in weakly relativistic regimes. However, in strong-field scenarios involving high-intensity and long-wavelength laser pulses, the dipole approximation becomes inadequate. Consequently, we explore the limitations of this approximation and introduce extensions to account for nondipole effects, such as the influence of the Lorentz force and photon momentum transfer. These extensions enable a more accurate description of strong-field ionization in the nonperturbative regime.

3.1 THEORETICAL FOUNDATIONS

The primary goal of a theoretical framework for ATI is to calculate the energy- and angle-resolved photoionization probability $\mathbb{P}(\mathbf{p})$ for an atomic system interacting with a laser field. This process begins with solving the time-dependent Schrödinger equation (TDSE), which governs the quantum evolution of the electron's wavefunction $|\psi(t)\rangle$. The Hamiltonian $\hat{H}(\mathbf{r}, t)$ in this context includes the electron's kinetic energy, its interaction with the external laser field, and the potential energy due to the atomic core. The Hamiltonian is expressed as [87]

$$\hat{H}(\mathbf{r}, t) = \frac{1}{2}\left(\hat{\mathbf{p}} - q\mathbf{A}(\mathbf{r}, t)\right)^2 + q\phi(\mathbf{r}, t) + V(\mathbf{r}), \tag{3.1}$$

where $q = -e$ is the electron charge, $\phi(\mathbf{r}, t)$ and $\mathbf{A}(\mathbf{r}, t)$ represent the scalar and vector potentials of the laser field, respectively, and $V(\mathbf{r})$ is the atomic binding potential. This Hamiltonian captures the influence of the oscillating electric and magnetic fields of the laser on the electron's dynamics.

To solve the TDSE, an initial wavefunction $|\psi(t_0)\rangle$ is specified, typically representing the bound state of the electron before the laser interaction begins. As the system evolves under the influence of the laser field, the probability of detecting an electron with a specific momentum $\mathbf{p}$ is determined by projecting the final state $|\psi(t \to \infty)\rangle$ onto the continuum state $|\psi_{\mathbf{p}}(t)\rangle$, which corresponds to a free electron with momentum $\mathbf{p}$.

The differential photoionization probability, which describes the likelihood of emitting an electron with energy $\epsilon_p = \frac{\mathbf{p}^2}{2}$ into a solid angle element $d\Omega_{\mathbf{p}}$, is given by [86]

$$\mathbb{P}(\mathbf{p}) = |T(\mathbf{p})|^2 \frac{d^3\mathbf{p}}{d\Omega_{\mathbf{p}} d\epsilon_p} = p|T(\mathbf{p})|^2, \tag{3.2}$$

where $T(\mathbf{p})$ is the transition amplitude, quantifying the strength of the transition from the bound state to the continuum state. The transition amplitude is defined as:

$$T(\mathbf{p}) = \lim_{t\to\infty} \langle \psi_{\mathbf{p}}(t) | \psi(t) \rangle. \tag{3.3}$$

This formalism highlights how the interaction between the electron and the intense laser field drives the ionization process. The vector potential $\mathbf{A}(\mathbf{r}, t)$ and scalar potential $\phi(\mathbf{r}, t)$ play critical roles in shaping the electron's trajectory and final momentum distribution. At high laser intensities, non-perturbative effects become significant, necessitating advanced theoretical models such as the SFA and saddle-point methods to accurately describe the ionization dynamics.

The evolution of the electron's wavefunction $|\psi(t)\rangle$ under the influence of the external field is governed by the Hamiltonian $\hat{H}$. The unitary time-evolution operator $\hat{U}(t, t_0)$ describes the transition from the initial state $|\psi(t_0)\rangle$ to the final state

$$|\psi(t)\rangle = \hat{U}(t, t_0)|\psi(t_0)\rangle. \tag{3.4}$$

The time-evolution operator $\hat{U}(t, t_0)$ satisfies the time-dependent Schrödinger equation [88]

$$i\frac{\partial}{\partial t}\hat{U}(t, t_0) = \hat{H}(\mathbf{r}, t)\hat{U}(t, t_0). \tag{3.5}$$

The operator $\hat{U}(t, t_0)$ adheres to the normalization condition $\hat{U}(t_0, t_0) = 1$ and the composition principle, which allows it to be factorized at intermediate times

$$\hat{U}(t, t_0) = \hat{U}(t, \tau)\hat{U}(\tau, t_0), \quad \forall \tau. \tag{3.6}$$

When the total Hamiltonian $\hat{H}(\mathbf{r}, t)$ can be decomposed into two components

$$\hat{H}(\mathbf{r}, t) = \hat{H}_1(\mathbf{r}) + \hat{H}_2(\mathbf{r}, t), \tag{3.7}$$

the Dyson series expansion provides a way to express the full evolution operator in terms of contributions from these components [89]

$$\hat{U}(t, t_0) = \hat{U}_1(t, t_0) - i \int_{t_0}^{t} d\tau \hat{U}(t, \tau)\hat{H}_2(\mathbf{r}, \tau)\hat{U}_1(\tau, t_0), \tag{3.8}$$

where $\hat{U}_1$ is the evolution operator corresponding to $\hat{H}_1(\mathbf{r})$. This expansion allows for the analysis of perturbative contributions from $\hat{H}_2(\mathbf{r}, t)$.

Assuming the Hamiltonian components are defined as

$$\hat{H}_1(\mathbf{r}) = \frac{\hat{\mathbf{p}}^2}{2} + V(\mathbf{r}), \quad \hat{H}_2(\mathbf{r}, t) = V_{le}(\mathbf{r}, t), \tag{3.9}$$

the transition amplitude can be derived as

$$T(\mathbf{p}) = \lim_{t \to \infty} \langle \psi_{\mathbf{p}}(t) | \psi(t) \rangle. \tag{3.10}$$

Expanding the evolution operator within this framework yields

$$\begin{aligned} T(\mathbf{p}) \quad = \quad & \lim_{t \to \infty, t_0 \to -\infty} \Bigg[\langle \psi_{\mathbf{p}}(t) | \hat{U}_A(t, t_0) | \psi_0(t_0) \rangle \\ & -i \int_{t_0}^{t} d\tau \langle \psi_{\mathbf{p}}(t) | \hat{U}(t, \tau) V_{le}(\mathbf{r}, \tau) \hat{U}_A(\tau, t_0) | \psi_0(t_0) \rangle \Bigg]. \end{aligned} \tag{3.11}$$

Since the final continuum state $|\psi_{\mathbf{p}}(t)\rangle$ and the initial bound state $|\psi_0(t_0)\rangle$ are eigenstates of $\hat{H}_A$ and orthogonal, the first term vanishes, leading to:

$$T(\mathbf{p}) = -i \int_{t_0}^{t} d\tau \langle \psi_{\mathbf{p}}(t) | \hat{U}(t, \tau) V_{le}(\mathbf{r}, \tau) | \psi_0(t_0) \rangle. \tag{3.12}$$

Reapplying the Dyson expansion results in

$$T(\mathbf{p}) = -i \int_{t_0}^{t} d\tau \int_{t_0}^{\tau} d\tau' \langle \psi_{\mathbf{p}}(t) | \hat{U}(t, \tau') V(\mathbf{r}) \hat{U}_{le}(\tau', \tau) V_{le}(\mathbf{r}, \tau) | \psi_0(t_0) \rangle. \tag{3.13}$$

To simplify the problem within the SFA, the following assumptions are made [90]

1. The atomic potential $V(\mathbf{r})$ is neglected for continuum state evolution, approximating $\hat{U} \approx \hat{U}_{le}$.

2. The final state of the electron is assumed to be a free plane wave, given by $\langle r|\psi_{\mathbf{p}}(t)\rangle = (2\pi)^{-3/2} e^{i\mathbf{p}\cdot\mathbf{r} - i\epsilon_p t}$.

3. The initial bound state $|\psi_0(t_0)\rangle$ does not interact with other bound states under the external field.

Within this approximation, the evolution operator $\hat{U}_{le}$ can be represented in terms of a momentum basis

$$\hat{U}_{le}(t,t') = \int d^3k \, |\chi_{\mathbf{k}}(t)\rangle\langle\chi_{\mathbf{k}}(t')|. \tag{3.14}$$

Combining these assumptions, the transition amplitude $T(\mathbf{p})$ can be expressed as:

$$\begin{aligned} T(\mathbf{p}) \;=\; & \lim_{t\to\infty}\lim_{t_0\to-\infty}\Bigg[-i\int_{t_0}^{t} \mathrm{d}\tau \int \mathrm{d}^3\mathbf{k}\, \langle \mathbf{p}(t)|\chi_{\mathbf{k}}(t)\rangle\langle\chi_{\mathbf{k}}(\tau)|V_{\mathrm{le}}(\mathbf{r},\tau)|\psi_0(\tau)\rangle \\ & + (-i)^2 \int_{t_0}^{t} \mathrm{d}\tau \int_{\tau}^{t} \mathrm{d}\tau' \int \mathrm{d}^3\mathbf{k}\, \langle \mathbf{p}(t)|\chi_{\mathbf{k}}(t)\rangle \\ & \times \langle\chi_{\mathbf{k}}(\tau')|V(\mathbf{r})U_{\mathrm{le}}(\tau',\tau)V_{\mathrm{le}}(\mathbf{r},\tau)|\psi_0(\tau)\rangle\Bigg]. \end{aligned} \tag{3.15}$$

To further simplify, we take the limit $t \to \infty$, using the identity:

$$\lim_{t\to\infty}\langle \mathbf{p}(t)|\chi_{\mathbf{k}}(t)\rangle = e^{i\varphi_\infty}\delta(\mathbf{p}-\mathbf{k}), \tag{3.16}$$

where φ_∞ is an arbitrary phase factor that does not affect the physical results. Applying this identity, the transition amplitude reduces to:

$$T(\mathbf{p}) = T_0(\mathbf{p}) + T_1(\mathbf{p}), \tag{3.17}$$

where $T_0(\mathbf{p})$ and $T_1(\mathbf{p})$ are defined as:

$$T_0(\mathbf{p}) = -i\int_{-\infty}^{\infty} \mathrm{d}\tau\, \langle\chi_{\mathbf{p}}(\tau)|V_{\mathrm{le}}(\mathbf{r},\tau)|\psi_0(\tau)\rangle, \tag{3.18}$$

and

$$T_1(\mathbf{p}) = (-i)^2 \int_{-\infty}^{\infty} \mathrm{d}\tau \int_{\tau}^{\infty} \mathrm{d}\tau'\, \langle\chi_{\mathbf{p}}(\tau')|V(\mathbf{r})U_{\mathrm{le}}(\tau',\tau)V_{\mathrm{le}}(\mathbf{r},\tau)|\psi_0(\tau)\rangle. \tag{3.19}$$

Here, $T_0(\mathbf{p})$ corresponds to the direct ionization pathway, where the electron is ionized directly from the ground state $|\psi_0\rangle$ due to the interaction potential $V_{\mathrm{le}}(\mathbf{r},\tau)$. The

term $T_1(\mathbf{p})$ represents a more complex process involving rescattering effects, where the electron interacts with the potential $V(\mathbf{r})$ after ionization.

The interaction between a laser field and an atom is a cornerstone of strong-field physics. The theoretical description of this interaction can be formulated in different gauges, each offering unique insights and computational advantages. In this section, we focus on the velocity gauge, which is particularly well-suited for studying strong-field ionization and high-energy processes. We also discuss the length gauge for comparison and explore the concept of gauge invariance, emphasizing its importance in ensuring consistent physical predictions. Special attention is given to the gauge dependence of the SFA.

3.2 INTERACTION IN VELOCITY AND LENGTH GAUGE

The velocity gauge, also known as the *minimal coupling gauge*, is derived from the minimal coupling principle in electrodynamics. In this gauge, the interaction between the laser field and the atom is described by the vector potential $\mathbf{A}(t)$, which modifies the momentum operator in the Hamiltonian. The total Hamiltonian in the velocity gauge is given by:

$$H_{\text{vel}} = \frac{1}{2m}\left(\mathbf{p} - e\mathbf{A}(t)\right)^2 + V(\mathbf{r}),$$

where $\mathbf{p}$ is the canonical momentum, e is the electron charge, m is the electron mass, and $V(\mathbf{r})$ is the atomic potential. The vector potential $\mathbf{A}(t)$ is related to the electric field $\mathbf{E}(t)$ of the laser by $\mathbf{E}(t) = -\partial_t \mathbf{A}(t)$.

The velocity gauge is particularly advantageous for numerical simulations and perturbative calculations in strong-field ionization. This is because the interaction term $\mathbf{p}\cdot\mathbf{A}(t)$ is linear in the momentum, simplifying the treatment of high-energy processes such as ATI and high-harmonic generation HHG. Additionally, the velocity gauge naturally incorporates the kinetic energy of the electron in the presence of the laser field, making it ideal for describing processes involving free electrons.

One of the key strengths of the velocity gauge is its computational efficiency. For example, in numerical solutions of the TDSE, the velocity gauge often leads to faster convergence compared to other gauges. This is particularly important in strong-field physics, where the laser fields are intense and the dynamics are highly nonlinear. Furthermore, the velocity gauge provides a clear framework for understanding the role of the electron's momentum in ionization processes, which is crucial for interpreting experimental results.

However, it is important to note that the SFA is gauge-dependent. In the velocity gauge, the SFA is formulated by neglecting the Coulomb potential $V(\mathbf{r})$ in the Hamiltonian and treating the electron as a free particle in the presence of the laser field. This leads to the so-called Volkov states, which are exact solutions for a free electron in a laser field. The SFA in the velocity gauge is particularly effective for describing processes such as ATI and HHG, where the electron's interaction with the laser field dominates over the atomic potential.

For completeness, we briefly discuss the length gauge, which is derived by performing a unitary transformation on the velocity gauge Hamiltonian. In the length gauge, the interaction between the laser field and the atom is described by the electric field $\mathbf{E}(t)$ acting on the dipole moment of the atom. The Hamiltonian in the length gauge is given by:

$$H_{\text{len}} = \frac{\mathbf{p}^2}{2m} + V(\mathbf{r}) - e\mathbf{r} \cdot \mathbf{E}(t),$$

where $\mathbf{r}$ is the position operator of the electron. The term $-e\mathbf{r} \cdot \mathbf{E}(t)$ represents the dipole interaction between the atom and the laser field.

While the length gauge provides a more intuitive description of tunneling ionization and bound-state dynamics [91, 92], it can be computationally challenging for problems involving high-energy electrons or long propagation times. This is because the dipole interaction term can lead to rapid oscillations in the wavefunction, requiring finer numerical grids and smaller time steps. Despite these challenges, the length gauge remains a valuable tool for understanding the physical mechanisms underlying strong-field processes.

A fundamental principle in electrodynamics is gauge invariance, which states that the physical predictions of a theory should not depend on the choice of gauge. In the context of laser-atom interactions, this means that the velocity gauge and the length gauge must yield identical results for observable quantities, such as ionization probabilities and harmonic spectra. However, the mathematical forms of the Hamiltonians in these gauges are different, leading to distinct theoretical and computational approaches.

Gauge invariance is ensured by the fact that the velocity gauge and the length gauge are related by a unitary transformation. Specifically, the wavefunctions in the two gauges are connected by a phase factor that depends on the vector potential $\mathbf{A}(t)$:

$$\psi_{\text{len}}(\mathbf{r}, t) = \exp\left(-\frac{ie}{\hbar}\mathbf{r} \cdot \mathbf{A}(t)\right) \psi_{\text{vel}}(\mathbf{r}, t).$$

This transformation preserves the physical content of the theory, as it leaves the expectation values of observables unchanged [93, 94]. However, the choice of gauge can influence the interpretation of the underlying physics [95]. For example, in the velocity gauge, the interaction is described in terms of the electron's momentum, which is particularly useful for understanding high-energy processes and free-electron dynamics. In contrast, the length gauge emphasizes the role of the electron's position, providing a clearer picture of tunneling ionization and bound-state dynamics.

The gauge dependence of the SFA is an important consideration in strong-field physics [95]. While the SFA is a powerful tool for understanding laser-atom interactions, its predictions can vary depending on the choice of gauge. This highlights the need for careful interpretation of results obtained using the SFA and underscores the importance of gauge invariance as a guiding principle in theoretical calculations.

In practice, the choice of gauge is often dictated by the specific problem at hand. For strong-field ionization and high-energy processes, the velocity gauge is typically preferred due to its computational efficiency and natural incorporation of the electron's kinetic energy. However, the length gauge may be more suitable for problems involving tunneling ionization or bound-state dynamics. Regardless of the gauge chosen, the principle of gauge invariance ensures that the physical predictions are consistent and reliable. In the rest of our thesis, we will be only considering the velocity guage unless otherwise stated.

3.3 DIPOLE APPROXIMATION AND BEYOND IN LASER–ATOM INTERACTION

The dynamics of an electron in a laser field are profoundly influenced by the oscillating electromagnetic forces acting upon it. In the simplest scenario, where the laser's spatial variation is negligible over the scale of the electron's motionm, the dipole approximation yields the well-known Volkov phase, a key ingredient in describing free-electron states in strong fields. However, as laser intensities or wavelengths rise , this approximation breaks down: the magnetic component of the Lorentz force, and spatial inhomogeneities begin to play decisive roles. This section explores how the Volkov phase evolves in and beyond the dipole regime, capturing nondipole corrections that arise when the electron experiences the full spacetime structure of the laser pulse.

3.3.1 *Formulation in the Dipole Approximation*

When an atom is exposed to an intense laser field, certain approximations can be employed to simplify the theoretical treatment of the problem. One such approximation is the dipole approximation, which is valid when the wavelength of the laser, λ_0, is

significantly larger than the characteristic atomic dimension, such as the Bohr radius a_0. Under this condition, the spatial variation of the laser field within the interaction region can be neglected, and only the temporal dependence of the field is considered. This simplification is particularly useful for describing the interaction dynamics in strong-field physics.

In the dipole approximation, the vector potential $\mathbf{A}_0$ of the laser pulse, as given in Eq. 2.18, can be rewritten as:

$$\mathbf{A}_0 = \frac{A_0}{\sqrt{1+\epsilon^2}} f(t) \left[\cos(\omega t + \phi_{\text{CEP}}) \mathbf{e}_x + \epsilon \Lambda \sin(\omega t + \phi_{\text{CEP}}) \mathbf{e}_y \right]. \tag{3.20}$$

In the velocity gauge (denoted by superscript V) and within the dipole approximation, the evolution of the quantum state $\chi^{(V)}(t)$ of an electron subjected to an external electromagnetic field is governed by the time-dependent Schrödinger equation. The TDSE in this context is expressed as

$$i \frac{\partial}{\partial t} \chi^{(V)}(\mathbf{r}, t) = \left[-\frac{1}{2}\nabla^2 - i\,\mathbf{A}(t) \cdot \nabla + \frac{1}{2}\mathbf{A}^2(t) \right] \chi^{(V)}(\mathbf{r}, t). \tag{3.21}$$

To facilitate further analysis, the wave function is represented in momentum space by introducing the Fourier transform:

$$\tilde{\chi}^{(V)}(\mathbf{p}, t) = \langle \mathbf{p} | \chi^{(V)}(t) \rangle. \tag{3.22}$$

Substituting this transformation into the TDSE leads to the modified equation in momentum space:

$$i\hbar \frac{\partial}{\partial t} \tilde{\chi}^{(V)}(\mathbf{p}, t) = \left[\frac{\mathbf{p}^2}{2} + \mathbf{A}(t) \cdot \mathbf{p} + \frac{1}{2}\mathbf{A}^2(t) \right] \tilde{\chi}^{(V)}(\mathbf{p}, t). \tag{3.23}$$

Applying the method of separation of variables and integrating over time, the solution in momentum representation takes the exponential form:

$$\tilde{\chi}^{(V)}(\mathbf{p}, t) = \exp\left(-\frac{i}{2} \int_0^t \left[\mathbf{p} + \mathbf{A}(\tau) \right]^2 d\tau \right). \tag{3.24}$$

By performing the inverse Fourier transform, the wave function in position representation is obtained:

$$\chi_{\mathbf{p}}^{(V)}(\mathbf{r}, t) = C e^{i\mathbf{p}\cdot\mathbf{r} - \frac{i}{2}\int_0^t (\mathbf{p} + \mathbf{A}(\tau))^2 d\tau}, \tag{3.25}$$

where C is a normalization constant. To determine its value, the normalization condition is applied:

$$\langle \chi_{\mathbf{p}}^{(V)}(\mathbf{r},t)|\chi_{\mathbf{p}'}^{(V)}(\mathbf{r},t)\rangle = \delta(\mathbf{p}-\mathbf{p}'). \tag{3.26}$$

This condition leads to the conclusion that $C = (2\pi)^{-3/2}$, resulting in the final expression for the Volkov wave function under the velocity gauge and dipole approximation:

$$\chi_{\mathbf{p}}^{(V)}(\mathbf{r},t) = (2\pi)^{-3/2} e^{i\mathbf{p}\cdot\mathbf{r}} e^{-iS(\mathbf{p},t)}, \tag{3.27}$$

where the phase factor, also known as the Volkov phase, is given by:

$$S(\mathbf{p},t) = \frac{1}{2}\int_0^t (\mathbf{p}+\mathbf{A}(\tau))^2 d\tau. \tag{3.28}$$

The Volkov phase describes the classical action of a free electron moving in the laser field. It encapsulates the influence of the laser field on the electron's motion and is a key component in understanding strong-field ionization processes.

The Volkov wave function can also be expressed in the length gauge. As described earlier, the two gauges are related by a time-dependent gauge transformation:

$$\chi_{\mathbf{p}}^{(L)}(\mathbf{r},t) = e^{i\mathbf{r}\cdot\mathbf{A}(t)}\,\chi_{\mathbf{p}}^{(V)}(\mathbf{r},t), \tag{3.29}$$

where $\chi_{\mathbf{p}}^{(L)}$ and $\chi_{\mathbf{p}}^{(V)}$ denote the Volkov states in the length and velocity gauges, respectively.

Substituting Eq. (3.27) into Eq. (3.29) yields

$$\chi_{\mathbf{p}}^{(L)}(\mathbf{r},t) = (2\pi)^{-3/2}\, e^{i(\mathbf{p}+\mathbf{A}(t))\cdot\mathbf{r}}\, e^{-iS(\mathbf{p},t)}. \tag{3.30}$$

This expression shows that, in the length gauge, the instantaneous momentum of the electron is shifted by the vector potential $\mathbf{A}(t)$, reflecting the direct coupling of the laser's electric field to the position operator in this gauge.

To solve the Volkov phase, we begin by expressing the vector potential of an elliptically polarized pulse in a more compact form. Starting from the vector potential given in Eq. 3.20, we rewrite it as

$$\mathbf{A}(t) = \sum_{j=0}^{2} \frac{\mathcal{A}_j}{\sqrt{1+\epsilon^2}} \left[\cos(\omega_j t+\phi_{\mathrm{CEP}})\mathbf{e}_x + \epsilon\Lambda\sin(\omega_j t+\phi_{\mathrm{CEP}})\mathbf{e}_y\right], \tag{3.31}$$

where the trigonometric products have been expanded. Here, the index j distinguishes between the lower ($j = 0$), central ($j = 1$), and upper ($j = 2$) frequency components of the pulse. The corresponding frequencies are defined as $\omega_0 = \left(1 - \frac{1}{n_p}\right)\omega$, $\omega_1 = \omega$, and $\omega_2 = \left(1 + \frac{1}{n_p}\right)\omega$, where ω is the central frequency of the pulse and n_p represents the number of optical cycles in the pulse. The amplitudes of the vector potential components vary with frequency and are given by $\mathcal{A}_0 = -A_0/4$, $\mathcal{A}_1 = A_0/2$, and $\mathcal{A}_2 = -A_0/4$, where A_0 is the peak amplitude of the vector potential. These expressions define the spectral characteristics of the field and its amplitude distribution across the frequency components. The lower ($j = 0$) and upper ($j = 2$) components have equal magnitudes but opposite signs, while the central component ($j = 1$) dominates with twice the amplitude of the side components.

The corresponding vector potential, as well as its Fourier spectra for different optical cycles, is illustrated in Fig. 2.2. The figure provides a visual representation of the temporal and spectral properties of the pulse, highlighting the contributions of the lower, central, and upper frequency components to the overall structure of the vector potential.

Using the vector potential 3.20, we carry out the integration in the Volkov phase 3.28 and obtain

$$\begin{aligned} S(\mathbf{p},t) &= \frac{1}{2}\mathbf{p}^2 t + \frac{t}{4}\sum_{i=0}^{2}\mathcal{A}_i^2 + \frac{1-\epsilon^2}{1+\epsilon^2}\sum_{i=0}^{2}\frac{\mathcal{A}_i^2}{8\omega_i}\sin(2\omega_i t + 2\phi_{\text{CEP}}) \\ &+ \sum_{i=0}^{1}\sum_{j=i+1}^{2}\frac{\mathcal{A}_i\mathcal{A}_j}{2(\omega_i-\omega_j)}\sin((\omega_i-\omega_j)t) \\ &+ \frac{1-\epsilon^2}{1+\epsilon^2}\sum_{i=0}^{1}\sum_{j=i+1}^{2}\frac{\mathcal{A}_i\mathcal{A}_j}{2(\omega_i+\omega_j)}\sin((\omega_i+\omega_j)t + 2\phi_{\text{CEP}}) \\ &+ \frac{p_x}{\sqrt{1+\epsilon^2}}\sum_{i=0}^{2}\frac{\mathcal{A}_i}{\omega_i}\sin(\omega_i t + \phi_{\text{CEP}}) \\ &- \epsilon\Lambda\frac{p_y}{\sqrt{1+\epsilon^2}}\sum_{i=0}^{2}\frac{\mathcal{A}_i}{\omega_i}\cos(\omega_i t + \phi_{\text{CEP}}). \end{aligned} \tag{3.32}$$

The detailed derivation of this result is provided in the Appendix A. Above, the Volkov phase was solved for the case of a plane wave laser pulse. However, the situation becomes more intricate when considering a twisted (or vortex) laser pulse, which carries orbital angular momentum and exhibits a complex spatial structure. Unlike plane waves, twisted pulses have non-trivial phase fronts and intensity distributions, characterized by a helical wavefront and a doughnut-shaped intensity profile. This spatial structure introduces additional components in the electron dynamics, particularly in the z-direction, which must be carefully accounted for in the analysis.

To derive the Volkov phase for a twisted laser pulse, we follow a procedure analogous to that used for plane waves, but with crucial modifications to incorporate the three-dimensional nature of the pulse. The envelope of the twisted pulse must be expanded to include not only the transverse (x and y) components but also the longitudinal (z) component. This expansion reflects the fact that the electron's interaction with the pulse is influenced by the spatially varying field structure. After performing the necessary integration over the pulse profile, we arrive at the following expression for the phase $S(\mathbf{p}, \tau)$:

$$\begin{aligned} S(\mathbf{p}, \tau) = \xi t &+ \sum_{j=1}^{9} \gamma_j \cos\left(\phi_j^{(c)} - \omega_j^{(c)} t\right) \\ &+ \sum_{l=1}^{13} \sigma_l \sin\left(\phi_l^{(s)} - \omega_l^{(s)} t\right), \end{aligned} \tag{3.33}$$

where $\mathbf{p}$ denotes the asymptotic momentum of the photoelectron, and τ represents the proper time. The first term, ξt, corresponds to a time-dependent phase accumulation that is linear in t, with ξ being a proportionality constant determined by the laser and electron parameters. The subsequent terms involve sums over harmonic contributions, with amplitudes γ_j and σ_l, frequencies $\omega_j^{(c)}$ and $\omega_l^{(s)}$, and phases $\phi_j^{(c)}$ and $\phi_l^{(s)}$.

The parameters ξ, γ_j, and σ_l are intricately linked to the properties of the twisted laser pulse, including its amplitude A_0, the number of photons n_p, the central frequency ω, the topological charge is denoted m_γ or m_ℓ (which determines the amount of orbital angular momentum carried by the pulse), and the angle θ_k between the pulse propagation axis and the electron momentum. Additionally, the impact parameter $\mathbf{b}$, which describes the transverse displacement of the electron's initial position relative to the pulse axis, plays a significant role in shaping these parameters.

The frequencies $\omega_j^{(c)}$ and $\omega_l^{(s)}$ are particularly noteworthy as they represent the characteristic frequencies associated with the electron's quiver motion in the presence of the Bessel pulse field. These frequencies emerge from the interplay between the electron's momentum and the spatially inhomogeneous fields of the twisted pulse. The phases $\phi_j^{(c)}$ and $\phi_l^{(s)}$ encode the initial conditions and the geometric relationship between the electron trajectory and the pulse's helical wavefronts. A comprehensive derivation of these quantities, along with their explicit mathematical expressions, is provided in Appendix A.

3.3.2 *Breakdown of the Dipole Approximation in Strong Fields*

The dipole approximation, as mentioned before, is a widely used simplification in atomic and laser physics, justified by the assumption that the wavelength of the laser radiation is much larger than the spatial extent of the atomic system. This approximation treats the laser field as spatially uniform, neglecting its spatial variation over the atomic scale. However, this simplification fails to account for the full nature of laser radiation, which consists of transverse electromagnetic waves with both electric ($\mathbf{E}$) and magnetic ($\mathbf{B}$) field components. While the magnetic field is significantly weaker than the electric field, with its magnitude given by $|\mathbf{B}| = |\mathbf{E}|/c$, its influence cannot always be ignored. The force exerted by the magnetic field on an electron is smaller than that of the electric field by a factor of v/c, where v is the electron velocity and c is the speed of light in vacuum. Under typical conditions, the assumption $v/c \ll 1$ holds, rendering the magnetic field's contribution negligible. However, in high-intensity laser fields, electrons can attain velocities such that v/c is no longer negligible, leading to significant magnetic field effects along the propagation direction [37, 96–105]. While the discussion above focuses on the breakdown of the dipole approximation in the long-wavelength (low-frequency) regime, where magnetic and retardation effects become significant, the approximation can also fail in the opposite limit of high photon frequencies. In this case, the wavelength of the radiation becomes comparable to or smaller than the spatial extent of the atomic orbital, such that the field can no longer be considered spatially uniform over the atom, i.e., $kr \sim 1$, where $k = \omega/c$ is the wave number. This high-frequency limit represents the conventional boundary of validity of the dipole approximation in atomic physics, where spatial variations of the electromagnetic field across the atom must be explicitly included in the interaction Hamiltonian.

The influence of the Lorentz force on the dynamics of an electron released into the continuum is illustrated in Fig. 3.1. When the electron is liberated from its parent ion into the continuum, it is accelerated within the transverse polarization plane by the electric field $\mathbf{E} = \mathbf{E}(\mathbf{r}, t)$, resulting in a velocity $\mathbf{v}(t) = (v_x, v_y, 0)$. The classical Lorentz force, $\mathbf{F}_L = q[\mathbf{v}(t) \times \mathbf{B}(\mathbf{r}, t)]$, induces a longitudinal momentum shift Δp_z along the beam propagation direction [80]. This shift becomes significant for electrons with sufficiently high velocities.

The trajectory of the photoelectron within the *reaction* plane is depicted in Fig. 3.1(b), illustrating the distance r_z traveled along the beam axis during each optical cycle. The paths are shown for three distinct wavelengths of the incident beam $\lambda = 800$ nm , $\lambda = 1600$ nm and $\lambda = 3200$ nm. For shorter wavelengths (e.g., 800 nm), the electron's motion is more confined, while for longer wavelengths (e.g., 1600 nm and 3200 nm),

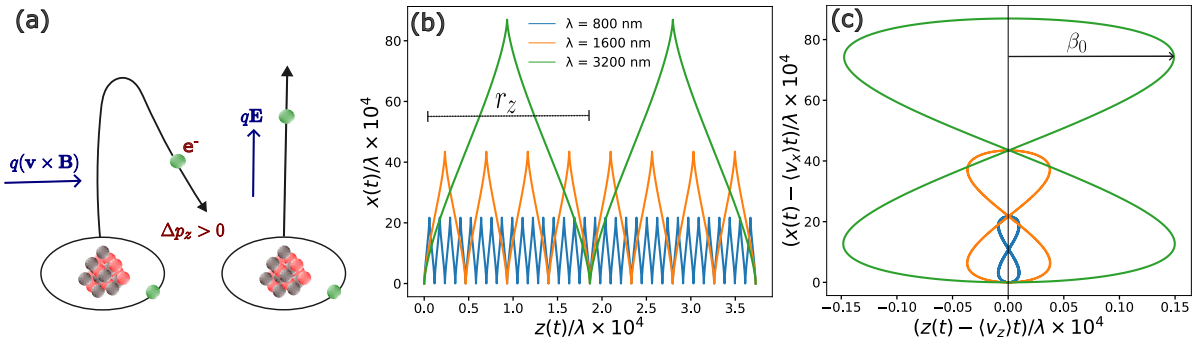

Figure 3.1: The influence of the Lorentz force on the dynamics of an electron released into the continuum is illustrated. (a) Upon being liberated from its parent ion into the continuum, the electron is accelerated within the transverse polarization plane by the electric field $\mathbf{E} = \mathbf{E}(\mathbf{r}, t)$. This acceleration results in a velocity $\mathbf{v}(t) = (v_x, v_y, 0)$. The classical Lorentz force, $\mathbf{F}_L = q[\mathbf{v}(t) \times \mathbf{B}(\mathbf{r}, t)]$, induces a longitudinal momentum shift Δp_z along the beam propagation direction. This shift becomes significant for electrons with sufficiently high velocities. (b) Trajectory of the photoelectron within the *reaction* plane, illustrating the distance r_z traveled along the beam axis during each optical cycle. The paths are depicted for two distinct wavelengths of the incident beam: $\lambda = 800$ nm (blue line), $\lambda = 1600$ nm (orange line) and $\lambda = 3200$ nm (green line) with a constant intensity at 10^{14}W/cm^2. (c) The characteristic *figure-eight motion* of the electron in the field, with an amplitude β_0 along the beam axis, after subtracting the constant average drift $\langle v_z \rangle t$. For amplitudes $\beta_0 \gtrsim a_0$, the influence of the Lorentz force becomes significant, necessitating a quantum mechanical treatment.

the electron travels a greater distance along the propagation axis. This wavelength dependence highlights the role of the laser field's temporal and spatial structure in shaping the electron's trajectory.

The characteristic *figure-eight motion* of the electron is observed when the constant average drift $\langle v_z \rangle t$ is subtracted from the motion, as shown in Fig. 3.1(c). The amplitude of this motion along the beam axis is characterized by the parameter β_0. For small amplitudes ($\beta_0 \ll a_0$), the motion is dominated by the electric field, and the dipole approximation remains valid. However, for larger amplitudes ($\beta_0 \gtrsim a_0$), the influence of the Lorentz force becomes significant, leading to a breakdown of the dipole approximation. In this regime, the electron's motion exhibits a pronounced figure-eight pattern, with the major axis aligned with the electric field's polarization direction and the lobes extending along the propagation axis. This behavior underscores the importance of considering the full electromagnetic nature of the laser field in high-intensity regimes. The deviation from the dipole approximation's unidirectional motion can be quantified using the parameter β_0, which characterizes the amplitude of the electron's motion along the propagation axis due to the magnetic field. This parameter is defined as:

$$\beta_0 \approx \frac{U_P}{2c\omega} = \frac{I}{8c\omega^3}, \tag{3.34}$$

where $U_P = I/4\omega^2$ is the ponderomotive energy, I is the laser intensity, and ω is the angular frequency of the laser field. When $\beta_0 \approx 1$ atomic unit (a.u.), the effects of the magnetic field become significant, leading to the breakdown of the dipole approximation. This regime is particularly relevant in high-intensity laser experiments, where the electron's motion is no longer confined to the polarization axis, and the figure-eight trajectory becomes pronounced. The parameter β_0 thus serves as a critical indicator of the validity of the dipole approximation and the onset of magnetic field effects in laser-matter interactions.

In high-intensity laser fields, the electron's velocity can approach relativistic values, making the condition $v/c \ll 1$ invalid. Under these circumstances, the magnetic field's influence becomes non-negligible, and the dipole approximation fails to accurately describe the electron dynamics. The figure-eight trajectory observed in such regimes highlights the importance of considering the full electromagnetic nature of the laser field, particularly in experiments involving strong-field ionization, high-harmonic generation, and laser-driven electron acceleration. Understanding these effects is crucial for interpreting experimental results and developing theoretical models that go beyond the dipole approximation.

3.3.3 *Extensions to Nondipole Effects*

To accurately incorporate nondipole effects within the SFA, it is necessary to express the vector potential of the driving laser field as a function of both position $\mathbf{r}$ and time t. This spatial and temporal dependence introduces additional complexities, as the laser field now includes both electric and magnetic field components. Such a formulation is essential for a precise description of the laser field's influence on electron dynamics in the strong-field regime. When a laser field propagates with an angular frequency ω along the wave vector direction $\mathbf{k} = \frac{\omega}{c}\hat{k}$, the vector potential can be expressed as a superposition of plane-wave components

$$\begin{aligned} \mathbf{A}(\mathbf{r},t) &= \int d^3\mathbf{k}\, \mathbf{A}(\mathbf{k},t), \\ \mathbf{A}(\mathbf{k},t) &= \mathrm{Re}\left\{\mathbf{a}(\mathbf{k})e^{i(\mathbf{k}\cdot\mathbf{r}-\omega_{\mathbf{k}}t)}\right\}. \end{aligned} \tag{3.35}$$

Here, $\mathbf{a}(\mathbf{k})$ represents the complex Fourier coefficient of the vector potential. This formalism allows us to describe the continuum state solution, as presented in Ref. [105], in the form of a modified Volkov state

$$\chi_{\mathbf{p}}(\mathbf{r},t) = \frac{1}{(2\pi)^{\frac{3}{2}}} e^{-i(\epsilon_p t - \mathbf{p}\cdot\mathbf{r})} e^{-i\Gamma(\mathbf{r},t)}, \tag{3.36}$$

where $\mathbf{p}$ is the electron's momentum, and $\Gamma(\mathbf{r},t)$ is the modified Volkov phase. This phase accounts for the interaction between the electron and the electromagnetic field, incorporating the spatial and temporal variations of the field. The modified Volkov state provides a coherent description of the electron's trajectory and energy evolution under the influence of the external field.

The modified Volkov phase, as derived in Ref. [105], can be expressed as

$$\begin{aligned}
\Gamma(\mathbf{r},t) \;=\; & \int d^3\mathbf{k}\, \rho(\mathbf{k}) \sin(\mathrm{u}(\mathbf{k}) + \theta(\mathbf{k})) \\
& + \int d^3\mathbf{k} \int d^3\mathbf{k}' \Big[\alpha^+(\mathbf{k},\mathbf{k}') \sin(\mathrm{u}(\mathbf{k}) + \mathrm{u}(\mathbf{k}') + \theta^+(\mathbf{k},\mathbf{k}')) \\
& \quad + \alpha^-(\mathbf{k},\mathbf{k}') \sin(\mathrm{u}(\mathbf{k}) - \mathrm{u}(\mathbf{k}') + \theta^-(\mathbf{k},\mathbf{k}')) \Big] \\
& + \frac{1}{2} \int d^3\mathbf{k} \int d^3\mathbf{k}' \sigma(\mathbf{k},\mathbf{k}') \rho(\mathbf{k}) \left(\frac{\sin(\mathrm{u}(\mathbf{k}) + \mathrm{u}(\mathbf{k}') + \theta(\mathbf{k}) + \xi(\mathbf{k},\mathbf{k}'))}{\eta(\mathbf{k}) + \eta(\mathbf{k}')} \right. \\
& \quad \left. + \frac{\sin(\mathrm{u}(\mathbf{k}) - \mathrm{u}(\mathbf{k}') + \theta(\mathbf{k}) - \xi(\mathbf{k},\mathbf{k}'))}{\eta(\mathbf{k}) - \eta(\mathbf{k}')} \right).
\end{aligned} \tag{3.37}$$

In this formulation, $\rho(\mathbf{k})$, $\theta(\mathbf{k})$, $\sigma(\mathbf{k},\mathbf{k}')$, and $\xi(\mathbf{k},\mathbf{k}')$ are projection operators that depend on the Fourier components of the vector potential $\mathbf{a}(\mathbf{k})$ and the electron's momentum $\mathbf{p}$. These operators describe how $\mathbf{p}$ and the wave vector $\mathbf{k}$ project onto the momentum-space representation of the field $\mathbf{A}(\mathbf{k}',t)$. The terms $\alpha^{\pm}(\mathbf{k},\mathbf{k}')$ represent ponderomotive contributions associated with each mode, proportional to the inner product of the Fourier coefficients, $[\mathbf{a}(\mathbf{k}) \cdot \mathbf{a}(\mathbf{k}')]$. Detailed definitions of these operators are provided in Appendix B, where we also introduce $\eta(\mathbf{k}) = \mathbf{p}\cdot\mathbf{k} - \omega(\mathbf{k})$.

For a few-cycle pulse with spatial dependence, the vector potential can be expressed as a sum of plane waves

$$\mathbf{A}(\mathbf{r},t) = \sum_{j=0}^{2} \frac{\mathcal{A}_j}{\sqrt{1+\epsilon^2}} \left[\cos(u_j + \phi_{\mathrm{cep}})\mathbf{e}_x + \epsilon\Lambda \sin(u_j + \phi_{\mathrm{cep}})\mathbf{e}_y \right], \tag{3.38}$$

where $u_j = \mathbf{k}_j \cdot \mathbf{r} - \omega_j t$ is a shorthand notation. Using this vector potential, the modified Volkov phase can be solved by performing the time integration

$$\begin{aligned}
\Gamma(\mathbf{r}, t) &= \sum_{j=0}^{2} \frac{\mathcal{A}_j^2}{4} \frac{u_j}{\eta_j(\mathbf{k})} + \frac{1-\epsilon^2}{1+\epsilon^2} \sum_{j=0}^{2} \frac{\mathcal{A}_j^2}{8\eta_j(\mathbf{k})} \sin(2u_j + 2\phi_{\text{cep}}) \\
&+ \sum_{i=0}^{1} \sum_{j=i+1}^{2} \frac{\mathcal{A}_i \mathcal{A}_j}{2(\eta_i(\mathbf{k}) - \eta_j(\mathbf{k}))} \sin(u_i - u_j) \\
&+ \frac{1-\epsilon^2}{1+\epsilon^2} \sum_{i=0}^{1} \sum_{j=i+1}^{2} \frac{\mathcal{A}_i \mathcal{A}_j}{2(\eta_i(\mathbf{k}) + \eta_j(\mathbf{k}))} \sin(u_i + u_j + 2\phi_{\text{cep}}) \\
&+ \frac{p_x}{\sqrt{1+\epsilon^2}} \sum_{j=0}^{2} \frac{\mathcal{A}_j}{\eta_j(\mathbf{k})} \sin(u_j + \phi_{\text{CEP}}) \\
&- \epsilon\Lambda \frac{p_y}{\sqrt{1+\epsilon^2}} \sum_{j=0}^{2} \frac{\mathcal{A}_j}{\eta_j(\mathbf{k})} \cos(u_j + \phi_{\text{CEP}}). \qquad (3.39)
\end{aligned}$$

The obtained solution closely resembles the one derived in the dipole approximation (Eq. 3.32), with the primary distinction being the inclusion of spatial dependence through the terms u_j and $\eta_j(\mathbf{k})$. This spatial dependence accounts for the nondipole effects, providing a more comprehensive description of the electron's interaction with the laser field.

In this chapter, we introduced the Strong-Field Approximation and derived the corresponding Volkov phase for pulsed laser fields, building on the field descriptions established earlier. We examined both the dipole and non-dipole regimes of the SFA, presenting explicit derivations of the Volkov phase in each case. In the next chapter, we will leverage this framework to compute the final transition amplitude within the SFA formalism. Additionally, we will introduce the necessary mathematical tools to evaluate key physical observables, enabling a comprehensive analysis of strong-field processes.

4

MATHEMATICAL TOOLS AND TECHNIQUES FOR STRONG FIELD IONIZATION

The quantum mechanical description of strong-field ionization revolves around calculating transition amplitudes between the initial bound state of an electron and its final Volkov continuum state in the laser field. Building on the derived Volkov phases for dipole and nondipole regimes (Chapter 3), we now address the core computational challenge: evaluating the time-dependent transition amplitude

$$T_0(\mathbf{p}) = -i \int_{-\infty}^{\infty} \mathrm{d}\tau \, \langle \chi_{\mathbf{p}}(\tau) | V_{\mathrm{le}}(\mathbf{r}, \tau) | \psi_0(\tau) \rangle, \tag{4.1}$$

where $\chi_{\mathbf{p}}(\tau)$ is the Volkov state with asymptotic momentum $\mathbf{p}$, $\psi_0(\tau)$ is the initial bound state, and $V_{\mathrm{le}}(\mathbf{r}, \tau)$ represents the laser-electron interaction potential. The oscillatory nature of the Volkov states encoded in their explicit time-dependent phase $e^{iS(\mathbf{p},\tau)}$ renders the integral highly oscillatory, demanding specialized analytical and numerical methods for practical evaluation. As the operator $V_{le} = H_{le} - H_A + V(\mathbf{r})$, we can further simplify the direct amplitude by performing the integration by parts. Since the vector potential is nonzero within some interval $t_i \leq t \leq t_f$, together with the operator V_{le}, the original equation 4.1 is modified to a more simplified form as

$$\begin{aligned} T_0(\mathbf{p}) = & -i \int_{t_i}^{t_f} d\tau \left(\langle \chi_{\mathbf{p}}(\tau) | \frac{\overleftarrow{\partial}}{\partial \tau} + \frac{\vec{\partial}}{\partial \tau} | \psi_0(\tau) \rangle \right) \\ & - i \int_{t_i}^{t_f} d\tau \langle \chi_{\mathbf{p}}(\tau) | V(\mathbf{r}) | \psi_0(\tau) \rangle \\ = & - \langle \chi_{\mathbf{p}}(\tau) | \psi_0(\tau) \rangle |_{t_i}^{t_f} - i \int_{t_i}^{t_f} d\tau \langle \chi_{\mathbf{p}}(\tau) | V(\mathbf{r}) | \psi_0(\tau) \rangle. \end{aligned} \tag{4.2}$$

This chapter develops the mathematical infrastructure to compute $T_0(\mathbf{p})$. Mainly we discuss two main approaches

- *Jacobi-Anger expansion*: Decomposes trigonometric nonlinearities in the Volkov phase into Bessel function series, isolating harmonic contributions.

- *Saddle point approximation*: Identifies dominant contributions to the integral from critical timescales in the complex plane.

The analysis of strong-field ionization processes requires sophisticated mathematical tools to handle the oscillatory integrals appearing in quantum transition amplitudes. Among these, the Jacobi-Anger expansion stands out as a particularly powerful technique for dealing with the trigonometric nonlinearities inherent in Volkov phase solutions.

4.1 JACOBI-ANGER EXPANSION

The Jacobi-Anger expansion provides a harmonic decomposition of complex exponential with trigonometric arguments. At its core, the expansion converts the oscillatory phase factor $e^{iz\sin\theta}$ and $e^{iz\cos\theta}$ into an infinite series of angular harmonics weighted by Bessel functions of the first kind:

$$e^{\pm iz\sin\theta} = \sum_{n=-\infty}^{\infty} J_n(z)e^{\pm in\theta}, \qquad e^{\pm iz\cos\theta} = \sum_{n=-\infty}^{\infty} (\pm i)^n J_n(z)e^{in\theta} \tag{4.3}$$

This transformation proves invaluable when working with the plane wave Volkov phase given in Equation 3.32, where multiple frequency components interact through their trigonometric dependencies. The Bessel functions $J_n(z)$ that appear as coefficients in this expansion possess several crucial properties that make them physically meaningful. Their asymptotic behavior for large orders shows that only certain photon number channels contribute significantly to the quantum dynamics, with the most important terms clustered around $n \approx z$ in the strong-field regime.

The convergence properties of this series deserve special attention. Unlike Taylor expansions, the Jacobi-Anger series converges absolutely for all arguments z and phases θ. This robust convergence behavior stems from the rapid decay of Bessel functions when the order n exceeds the magnitude of the argument $|z|$. From a physical perspective, this mathematical property ensures that the infinite series can be safely truncated in practical calculations while maintaining controlled accuracy - a crucial feature for numerical implementations.

4.1.1 *Implementation for Plane Wave in Dipole Approximation*

When applied to the plane wave Volkov phase of Equation 3.32, the Jacobi-Anger expansion must address several distinct types of trigonometric terms. The linear polarization components proportional to $\sin(\omega_i t)$ generate standard Bessel series expan-

sions, while the elliptical polarization terms involving $\cos(\omega_i t)$ require phase-shifted versions of the expansion. The cross-frequency terms present additional complexity, as they produce coupled expansions where different frequency components interact. The exponential $e^{iS(\mathbf{p},t)}$ in the dipole case can be expanded using the Jacobi-Anger formula as

$$
\begin{aligned}
e^{-iS(\mathbf{p},t)} = \exp\left(-i\left(\frac{1}{2}\mathbf{p}^2 t + \frac{t}{4}\sum_{i=0}^{2}\mathcal{A}_i^2\right)\right) \\
&\times \prod_{i=0}^{2}\sum_{n_i=-\infty}^{\infty} J_{n_i}\left(\frac{1-\epsilon^2}{1+\epsilon^2}\frac{\mathcal{A}_i^2}{8\omega_i}\right) e^{-in_i(2\omega_i t+2\phi_{\text{CEP}})} \\
&\times \prod_{i=0}^{1}\prod_{j=i+1}^{2}\sum_{m_{ij}=-\infty}^{\infty} J_{m_{ij}}\left(\frac{\mathcal{A}_i\mathcal{A}_j}{2(\omega_i-\omega_j)}\right) e^{-im_{ij}(\omega_i-\omega_j)t} \\
&\times \prod_{i=0}^{1}\prod_{j=i+1}^{2}\sum_{k_{ij}=-\infty}^{\infty} J_{k_{ij}}\left(\frac{1-\epsilon^2}{1+\epsilon^2}\frac{\mathcal{A}_i\mathcal{A}_j}{2(\omega_i+\omega_j)}\right) e^{-ik_{ij}[(\omega_i+\omega_j)t+2\phi_{\text{CEP}}]} \\
&\times \prod_{i=0}^{2}\sum_{\ell_i=-\infty}^{\infty} J_{\ell_i}\left(\frac{p_x\mathcal{A}_i}{\sqrt{1+\epsilon^2}\omega_i}\right) e^{-i\ell_i(\omega_i t+\phi_{\text{CEP}})} \\
&\times \prod_{i=0}^{2}\sum_{q_i=-\infty}^{\infty} (-i)^{q_i} J_{q_i}\left(\epsilon\Lambda\frac{p_y\mathcal{A}_i}{\sqrt{1+\epsilon^2}\omega_i}\right) e^{iq_i(\omega_i t+\phi_{\text{CEP}})}.
\end{aligned}
\tag{4.4}
$$

This expansion dissolves the trigonometric functions in the exponent and makes it easier to carry the integration. Thus after inserting above expression in Eq. 4.2 and then applying the integration within the duration of the pulse $[0, \tau_p]$ we arrive at the final expression of the direct transition amplitude as

$$
\begin{aligned}
T_0^D(\mathbf{p}) = \prod_{i=1}^{15}\Big\{(-i)^{n_i\Theta(i-12)} \quad & \sum_{n_i=-\infty}^{\infty} J_{n_i}(x_i^D)\left(\frac{\langle\mathbf{p}|V(\mathbf{r})|\Psi_0\rangle}{\epsilon_p+U_p+\Omega_{n_i}^D+I_p}+\langle\mathbf{p}|\Psi_0\rangle\right) \\
& \times\left(1-e^{i\left[\left(\epsilon_p+U_p+\Omega_{n_i}^D+I_p\right)\tau_p+\Phi_i^D\right]}\right)\Big\},
\end{aligned}
\tag{4.5}
$$

where $\Theta(x)$ is the Heaviside step function which ensures that the extra factor i^{n_i} appears only for the last three terms ($i \geq 13$), while it remains absent for the first 12 terms ($i \leq 12$). Here we redefined the frequencies and phases in terms of Ω and Φ respectively and including x_i they are defined in the Appendix A. The superscript D is introduced to distinguish this transition amplitude from ones that will be derived later in the nondipole case. The pondermotive energy U_p is given by $U_p = \frac{\mathcal{A}_j^2}{4}$ for $j = 0:2$. To approximate the expansion coefficients effectively, the argument of each Bessel function imposes a natural cut-off for the corresponding index n_i. Beyond this limit, the Bessel function exhibits an exponential decline, following the relation $J_{n_i}(x) \sim e^{-n_i}$ for values where $|n_i| > |x| = n_{i,\max}$. Consequently, the fifteen originally

infinite summations can be truncated within the range $-n_{i,\max} \leq n_i \leq n_{i,\max}$, providing a reliable approximation. The resulting expression reveals how different photon number channels contribute to the overall transition amplitude. Specifically, the p_x-coupled terms produce Bessel functions whose arguments depend on the electron momentum component along the polarization axis, while the p_y terms incorporate ellipticity effects through modified arguments.

4.1.2 *Implementation for Plane Wave in Nondipole Approximation*

By following the same approach, we obtain the complete solution for the transition amplitude in the nondipole case, expressed as

$$T_0^{ND}(\mathbf{p}) = \prod_{i=1}^{15} \Big\{ (-i)^{n_i \Theta(i-12)} \sum_{n_i=-\infty}^{\infty} J_{n_i}(x_i^{ND}) \left(\frac{\langle \mathbf{p}_{n_i} | V(\mathbf{r}) | \Psi_0 \rangle}{\epsilon_p + U_p + \Omega_{n_i}^{ND} + I_p} + \langle \mathbf{p}_{n_i} | \Psi_0 \rangle \right) \times \left(1 - e^{i\left[\left(\epsilon_p + U_p + \Omega_{n_i}^{ND} + I_p \right) \tau_p + \Phi_{n_i}^{ND} \right]} \right) \Big\}. \tag{4.6}$$

as before we have $\Theta(x)$ as the Heaviside step function which ensures that the extra factor i^{n_i} appears only for the last three terms ($i \geq 13$), while it remains absent for the first 12 terms ($i \leq 12$). Similarly, we redefined the frequencies and phases in terms of Ω and Φ respectively and including x_i and $\mathbf{p}_i$ are defined in the Appendix B. Similarly, the pondermotive energy U_p is given by $U_p = \sum_j \frac{\mathcal{A}_j^2}{4\eta_j}$ for $j = 0:2$.

The situation becomes considerably more complex when dealing with twisted light fields described by Equation 3.33. Here, the phase structure contains not only multiple frequency components but also spatial phase modulations carrying orbital angular momentum. Each cosine and sine term in the twisted phase requires individual expansion, with the azimuthal phase dependence introducing additional angular momentum conservation constraints.

4.2 SADDLE POINT APPROXIMATION

The saddle point approximation (SPA) serves as a cornerstone technique for evaluating oscillatory integrals that emerge in the path integral formulation of strong-field ionization [106]. Within the framework of the SFA, the transition amplitude between bound and continuum states involves highly oscillatory integrals whose exact evaluation proves computationally prohibitive. The SPA provides an asymptotically exact method for approximating these integrals by identifying dominant contributions from critical points in the complex-time plane [107].

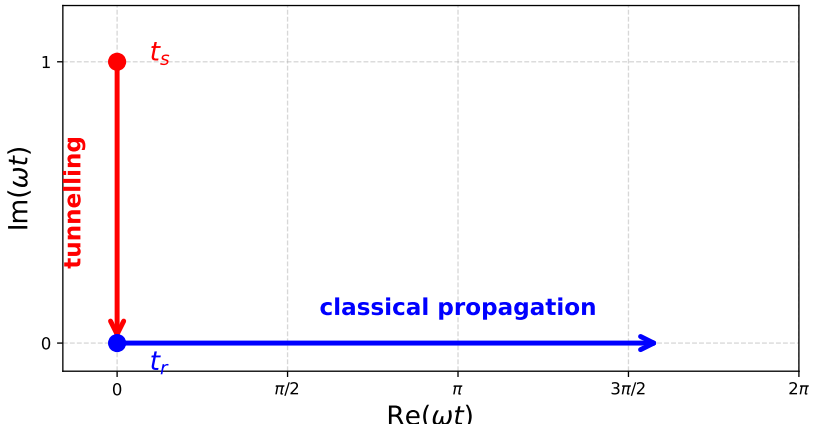

Figure 4.1: The standard contour in complex time describes the electron dynamics, starting from the complex ionization instant t_s, evolving toward its real component $t_r = \Re(t_s)$, and subsequently propagating along the real-time axis until detection at $t_f \to +\infty$.

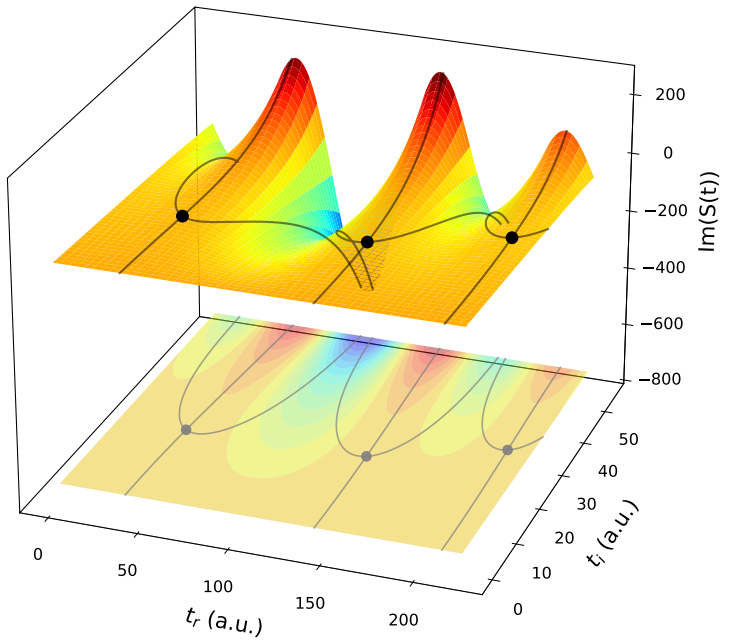

Figure 4.2: 3D Landscape of the time-dependent action $S(t')$ and it projection computed numerically for the strong-field ionization. Height map shows $\Im[S(t')]$ controlling the amplitude $|e^{-iS(t')}| = e^{\Im[S(t')]}$ of the quantum mechanical phase factor. Black curves depict steepest descent contours where $\Re[S(t')] = \text{const.}$, orthogonal to the $\Im[S(t')]$ gradient. Black markers indicate saddle points t_s satisfying $S'(t_s) = 0$, which dominate the temporal integration path. The plotted solution corresponds to field parameters: $\epsilon = 1.0$, $\lambda = 800$ nm, $I = 5 \times 10^{14}$ W/cm^2, $n_p = 2$ cycles, $I_p = 15.6$ eV.

Mathematically, the method relies on the analytic continuation of the time variable into the complex plane, where the integration contour can be deformed to pass through saddle points along paths of steepest descent [108–110]. The complex-time landscape shown in Fig. 4.2 provides crucial insights into strong-field ionization dynamics. The saddle point approximation's physical intuition becomes evident through this visualization: dominant contributions emerge from specific critical points, while the steepest descent paths guide contour deformation. This approach not only clarifies the quantum dynamics but also enables efficient computational implementation by isolating physically relevant spacetime regions. This approach captures both the quantum tunneling dynamics (through imaginary time components) and classical trajectory propagation (through real time components), as shown in Fig. 4.1. The approximation becomes exact in the semiclassical limit ($\hbar \to 0$), making it particularly suitable for strong-field physics where the action is typically large compared to $\hbar$.

4.2.1 *Introduction to the Stationary Phase Method*

The stationary phase method provides the mathematical foundation for evaluating integrals of the form [111]

$$\mathcal{I} = \int_{-\infty}^{\infty} f(t)\, e^{i\phi(t)/\zeta}\, dt, \tag{4.7}$$

where $f(t)$ denotes a slowly varying amplitude function, $\phi(t)$ represents the rapidly oscillating phase, and ζ serves as a small asymptotic parameter. In the context of strong-field ionization, ζ corresponds to the reduced Planck constant $\hbar$, while $\phi(t)$ embodies the classical action $S(\mathbf{p}, t)$. As shown in Fig. 4.3, the rapid oscillations of $\Re[e^{iS(\mathbf{p},t)}]$ (shown for $\epsilon_p = 5\omega$) justify the need for such asymptotic methods. The stationary points of $\phi(t)$ determine the dominant contributions to $\mathcal{I}$, analogous to how saddle points in the complex-time plane govern the ionization dynamics. The critical insight derives from the Riemann-Lebesgue lemma [112], which establishes that contributions away from stationary points vanish in the limit $\zeta \to 0$ due to destructive interference. The stationary phase points t_s satisfy

$$\left.\frac{d\phi}{dt}\right|_{t=t_s} = 0. \tag{4.8}$$

For analytic functions, we can expand the phase about each stationary point to second order

$$\phi(t) \approx \phi(t_s) + \frac{1}{2}\phi''(t_s)(t - t_s)^2 + O((t - t_s)^3). \tag{4.9}$$

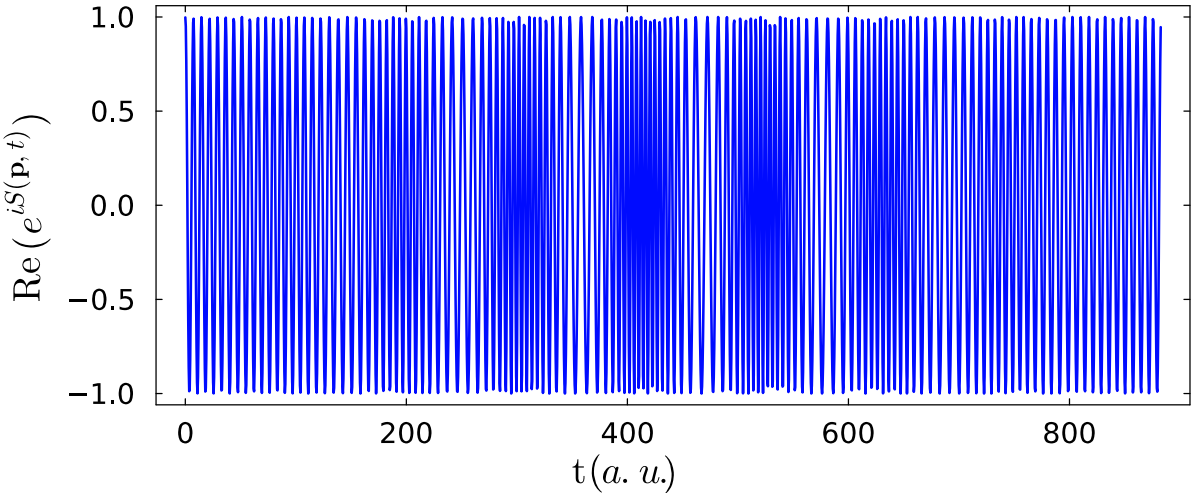

Figure 4.3: Real part of the Volkov phase, $\Re[e^{iS(\mathbf{p},t)}]$, as a function of real time, exhibiting rapid oscillations. The calculation assumes a photoelectron energy $\epsilon_p = 5\omega$ in a circularly polarized, 8-cycle laser pulse with a peak intensity of 5×10^{14} W/cm^2 and a wavelength of 800 nm.

Substituting this expansion into the integral yields

$$\mathcal{I} \approx f(t_s) e^{i\phi(t_s)/\epsilon} \int_{-\infty}^{\infty} \exp\left(\frac{i\phi''(t_s)}{2\zeta}(t - t_s)^2\right) dt. \tag{4.10}$$

The Gaussian integral evaluates exactly to

$$\mathcal{I} \approx f(t_s) \sqrt{\frac{2\pi i\zeta}{\phi''(t_s)}} e^{i\phi(t_s)/\zeta}. \tag{4.11}$$

When multiple isolated saddle points contribute, the total integral becomes a coherent sum

$$\mathcal{I} \approx \sum_n f(t_s^{(n)}) \sqrt{\frac{2\pi i\zeta}{\phi''(t_s^{(n)})}} e^{i\phi(t_s^{(n)})/\zeta}. \tag{4.12}$$

The interference between these terms generates characteristic patterns in the resulting momentum distributions observable in photoelectron spectra.

4.2.2 *Complex-Time Solutions and their Physical Meaning*

In the theory of strong-field ionization, the electron dynamics are governed by semi-classical saddle-point equations derived from the quantum mechanical amplitude

[113, 114]. The dominant contribution to the ionization amplitude arises from solutions to the saddle-point equation

$$\frac{[\mathbf{p} + \mathbf{A}(t_s)]^2}{2} + I_p = 0, \tag{4.13}$$

where $\mathbf{p}$ represents the asymptotic drift momentum. Under the strong-field approximation, which neglects the Coulomb potential after tunneling, this equation admits exclusively complex-valued solutions of the form $t_s = t_r + it_i$. The real part t_r corresponds to the ionization phase within the laser cycle when the electron emerges from the barrier, typically occurring near the field maximum ($\omega t_r \approx \pi/2$ for a cosine pulse). The imaginary part t_i quantifies the tunneling duration through the relation

$$\tau_{\text{tun}} \approx \frac{\sqrt{2I_p}}{E_0 |\sin(\omega t_r)|}, \tag{4.14}$$

where E_0 represents the peak electric field strength. This expression follows the under-the-barrier flight time [13, 115], considering the barrier width $d \sim I_p/E(t_r)$ and the characteristic velocity $v \sim \sqrt{2I_p}$ derived from energy conservation, with the instantaneous field given by $E(t_r) = E_0 \sin(\omega t_r)$. It should be emphasized that the saddle-point time t_s is a complex quantity. Its real part, $t_r = \text{Re}(t_s)$, denotes the physical ionization (emission) time at which the electron exits the tunneling barrier and enters the continuum, while its imaginary part, $t_i = \text{Im}(t_s)$, does not correspond to an observable time but rather characterizes the under-the-barrier motion and governs the exponential suppression of the ionization probability. The time variable appearing in Eq. 4.14 therefore refers to the real emission time $\text{Re}(t_s)$, which is used for the subsequent classical propagation of the electron in the continuum.

The complex exit momentum $\mathbf{v}(t_s) = \mathbf{p} + \mathbf{A}(t_s)$ determines the initial conditions for subsequent continuum propagation. The real part $\text{Re}[\mathbf{v}(t_s)]$ yields the observable drift momentum corresponding to classical trajectories, while the imaginary component $\text{Im}[\mathbf{v}(t_s)]$ reflects the quantum momentum uncertainty inherent to the tunneling process [116].

The solution formalism implies that the electron follows a complex spacetime trajectory, spending an imaginary time interval t_i under the barrier before emerging at real time t_r [117]. This interpretation provides a natural explanation for several quantum phenomena: the finite probability of ionization below the classical barrier height , the phase-dependent nature of ionization rates encoded in t_r, and the initial momentum spread manifested through non-zero values of $\text{Im}[\mathbf{v}(t_s)]$. This complex-time formalism maintains consistency with three key experimental and theoretical frameworks: the attoclock measurements of tunneling time [118], the imaginary-time method em-

ployed in instanton physics [119], and the quantum-classical correspondence principle in the high-field limit. The approach bridges the gap between fully quantum mechanical treatments and intuitive semiclassical pictures of strong-field processes.

4.2.3 *Validity and Limitations of the Saddle Point Approximation*

The saddle point approximation maintains validity under specific physical conditions. The primary requirement is the existence of a small parameter ζ such that the phase varies rapidly compared to the amplitude. In atomic units, this translates to the condition $S/\hbar \gg 1$ which typically holds for strong laser fields and high ionization potentials. The approximation remains accurate when the laser field dominates the atomic potential during the tunneling process, expressed mathematically as $\kappa E_0 \gg \frac{Z}{r_{\text{tun}}^2}$ where $\kappa = \sqrt{2I_p}$ and $r_{\text{tun}} = I_p/E_0$ represents the tunneling exit point. Several physical regimes challenge the validity of the standard saddle point approximation. In the multiphoton ionization regime characterized by the Keldysh parameter $\gamma \gg 1$, the discrete photon absorption channels render the semiclassical treatment inadequate. The Coulomb potential introduces significant corrections when $\frac{Z}{r_{\text{tun}}} \gtrsim U_p$ where U_p denotes the ponderomotive energy. In such cases, the long-range Coulomb interaction modifies both the saddle point positions and the resulting momentum distributions [70, 120].

When multiple saddle points approach each other in the complex plane, the simple Gaussian approximation fails and requires extension through uniform asymptotic expansions [108, 121]. The critical case occurs when two saddle points coalesce, leading to a divergence in the prefactor $\sqrt{2\pi i\zeta/\phi''(t_s)}$. This situation necessitates Airy function expansions to properly describe the transition region.

Despite these limitations, the saddle point approximation remains the most powerful analytical tool for understanding strong-field ionization dynamics. Its ability to provide both quantitative predictions and qualitative physical insight makes it indispensable for interpreting attosecond-scale electron dynamics in intense laser fields.

4.3 NUMERICAL IMPLEMENTATION

The numerical solution of saddle point equations in strong-field ionization requires careful consideration of complex analysis, nonlinear root-finding, and convergence criteria. This section presents a comprehensive implementation framework using Julia's numerical computing capabilities [122–124].

4.3.1 *Root-Finding Algorithms for Saddle Points*

The saddle point equation for strong-field ionization takes the form:

$$f(t_s; \mathbf{p}) = \frac{1}{2}[\mathbf{p} + \mathbf{A}(t_s)]^2 + I_p = 0 \tag{4.15}$$

where $t_s \in \mathbb{C}$ and $\mathbf{p} \in \mathbb{R}^3$. For a monochromatic field with frequency ω and amplitude E_0, the initial guesses are distributed across laser cycles

$$t_s^{(0)} = \frac{2\pi n}{\omega} + i\frac{I_p}{E\left|i\sqrt{2I_p}\right|}, \quad n \in \mathbb{Z} \tag{4.16}$$

The algorithm for generates these initial estimates is shown below

Algorithm 1 Generation of Initial Guesses for Saddle Point Solutions

Require: Ionization potential I_p, electric field $\mathbf{E}(t)$, frequency ω, number of cycles n_{cycle}

Ensure: Array of complex initial guesses $t_s^{(0)}$

Initialize empty array guesses $\leftarrow \emptyset$
Calculate cycle duration $T \leftarrow 2\pi/\omega$
▷ Find electric field maxima
Sample times $t_{\text{samples}} \leftarrow \text{linspace}(0, n_{\text{cycle}}T, 1000)$
Evaluate field $E_{\text{samples}} \leftarrow \mathbf{E}(t_{\text{samples}})$
Find peaks peak_indices $\leftarrow$ find_local_maxima$(|E_{\text{samples}}|)$
Extract peak times $t_{\text{peaks}} \leftarrow t_{\text{samples}}$[peak_indices]
▷ Generate guesses per half-cycle
for $n \leftarrow 0$ to $n_{\text{cycle}} - 1$ **do**
    for $k \leftarrow 1$ to num_per_half_cycle **do**
        $t_{\text{re}} \leftarrow nT + \frac{(k-1)T}{2\times\text{num\_per\_half\_cycle}}$
        $t_{\text{im}} \leftarrow \sqrt{2I_p}/\max(|\mathbf{E}(t_{\text{re}})|, 0.1)$
        $t_0 \leftarrow t_{\text{re}} + it_{\text{im}}$
        guesses.append(t_0)
    end for
end for
▷ Add extra guesses near peaks
for t_p in t_{peaks} **do**
    for α in $[0.5, 1.0, 1.5]$ **do**
        $t_{\text{im}} \leftarrow \alpha\sqrt{2I_p}/\max(|\mathbf{E}(t_p)|, 0.1)$
        guesses.append$(t_p + it_{\text{im}})$
    end for
end for
return guesses

4.3.2 *Newton-Raphson and Iterative Methods*

The Newton-Raphson method [125] in the complex plane requires careful handling of the Jacobian [126]

$$t_s^{(k+1)} = t_s^{(k)} - J^{-1}(t_s^{(k)})f(t_s^{(k)}) \tag{4.17}$$

where the Jacobian $J(t_s) = \partial f/\partial t_s = (\mathbf{p} + \mathbf{A}(t_s)) \cdot \mathbf{E}(t_s)$. The implementation uses automatic differentiation for numerical stability as shown below

Algorithm 2 Complex Newton-Raphson Solver

Require: Function f, initial guess z_0, tolerance tol $= 1 \times 10^{-10}$, maximum iterations max_iter $= 100$, step size $h = 1 \times 10^{-8}$, minimum derivative min_derivative $= 1 \times 10^{-12}$

Ensure: Approximate root z satisfying $|f(z)| <$ tol

$z \leftarrow \text{complex}(z_0)$
Initialize empty history list history $\leftarrow [\,]$
for $i \leftarrow 1$ to max_iter **do**
    $f_z \leftarrow f(z)$
    Append $(z, |f_z|)$ to history
    if $|f_z| <$ tol **then**
        return z
    end if
    ▷ Finite difference derivative with fallback
    Try:
        $f'_z \leftarrow \frac{f(z+h)-f(z-h)}{2h}$
    Catch:
        $f'_z \leftarrow \frac{f(z+h)-f(z)}{h}$
    if $|f'_z| <$ min_derivative **then**
        Try:
            $f'_z \leftarrow \frac{\text{imag}(f(z+ih))}{h}$
        if $|f'_z| <$ min_derivative **then**
            $z \leftarrow z + 0.1 \times (\text{randn}() + i \times \text{randn}())$
            continue
        end if
    end if
    $\Delta z \leftarrow \frac{f_z}{f'_z}$
    $z_{\text{new}} \leftarrow z - \Delta z$
    if $|\Delta z| > 10^6$ **then**
        warn "Large step detected, scaling down"
        $\Delta z \leftarrow \frac{\Delta z}{|\Delta z| \times 10^3}$
        $z_{\text{new}} \leftarrow z - \Delta z$
    end if
    if $|\Delta z| <$ tol **then**
        return z_{new}
    end if
    $z \leftarrow z_{\text{new}}$
end for
warn "Maximum iterations reached without convergence"
return z

4.3.3 *Stability and Convergence of Complex-Time Roots*

The numerical solution of saddle point equations in complex time presents unique convergence challenges governed by the local analytic properties of the Volkov phase functional. The convergence behavior is characterized by the Lipschitz continuity condition of the Jacobian [127]

$$\|J(t_s) - J(t_s')\| \leq L\|t_s - t_s'\|^{\alpha} \tag{4.18}$$

where L is the Lipschitz constant and $\alpha \in (0, 1]$ quantifies the Hölder continuity of the Jacobian matrix $J(t_s) = \partial f / \partial t_s$. For the saddle point equation $f(t_s; \mathbf{p})$, the Jacobian exhibits quasi-periodic behavior with $L \sim E_0\sqrt{I_p}$ and $\alpha = 1$ in the tunneling regime ($\gamma < 1$), transitioning to $\alpha \approx 0.5$ in the multiphoton regime ($\gamma > 3$). The implementa-

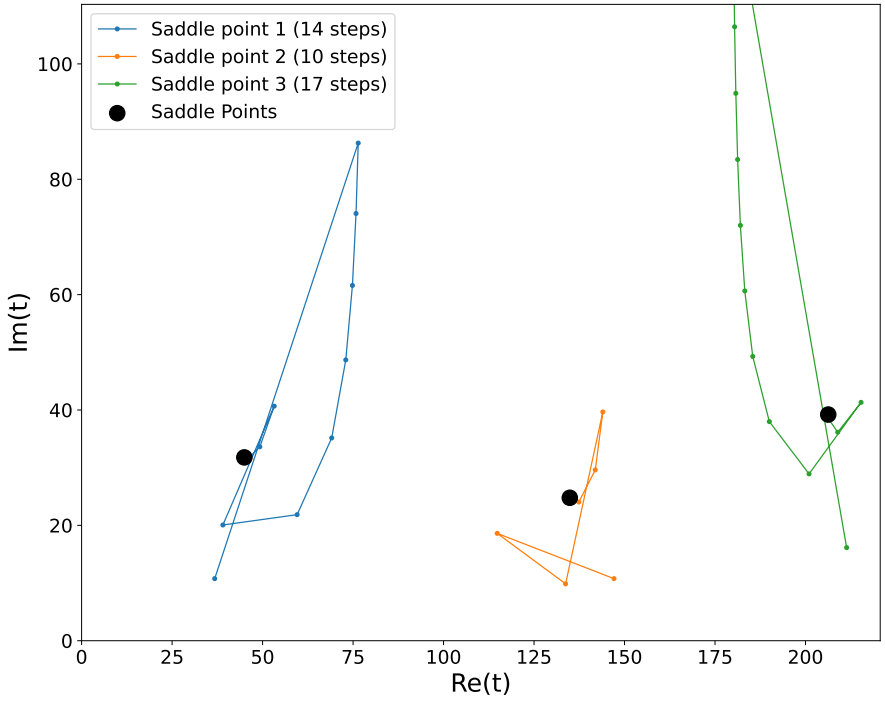

Figure 4.4: Convergence paths of Newton-Raphson iterations in the complex time plane for saddle point solutions. Markers show the progression of iterations (small dots) with final converged saddle points indicated by black circles. The paths represent solutions to the saddle point equation $f(t_s; \mathbf{p}) = 0$ where $\Re(t) \in (0, T_p)$ and $\Im(t) > 0$. Numbers indicate the iteration count for each convergence path. The other parameters are same as in Fig. 4.2.

tion employs dual-number automatic differentiation to maintain numerical stability

$$J(t_s) = \mathrm{Im}\left(\frac{f(t_s + \epsilon(1+i))}{\epsilon}\right), \quad \epsilon = 10^{-20} \tag{4.19}$$

This approach provides machine-precision accuracy (relative error $< 10^{-14}$) while avoiding cancellation errors inherent in finite-difference methods. The residual decay follows the theoretical quadratic convergence pattern until reaching machine precision, as shown in the inset of Fig. 4.4.

4.4 COMPUTATION OF MOMENTUM DISTRIBUTIONS

The ionization dynamics can be quantitatively described through the transition amplitude from the bound state to the continuum. With the integral now approximated in terms of dominant saddle-point contributions, we obtain the semiclassical expression for the transition amplitude [95]

$$T_0^{\mathrm{SP}}(\mathbf{p}) = \sum_{t_s} V^x(\mathbf{p}, t_s) \sqrt{\frac{2\pi i}{\mathbf{E}(t_s) \cdot [\mathbf{p} + \mathbf{A}(t_s)]}} e^{i[S(\mathbf{p}, t_s) + I_p t_s]}, \tag{4.20}$$

and the factor

$$V^x(\mathbf{p}, t_s) = \begin{cases} \langle \mathbf{p} | V_{le}^x | \Psi_0 \rangle & (x = \mathrm{V}), \\ \langle \mathbf{p} + \mathbf{A}(t_s) | V_{le}^x | \Psi_0 \rangle & (x = \mathrm{L}), \end{cases} \tag{4.21}$$

depends on the choice of gauge. The sum runs over all relevant saddle-point solutions t_s which are part of the integration contour. This expression reveals several key physical insights. The prefactor $V^x(\mathbf{p}, t_s)$ represents the projection of the bound state $|\Psi_0\rangle$ onto the continuum state $|\mathbf{p}\rangle$ through the interaction potential V_{le}^x. The denominator $\mathbf{E}(t_s) \cdot (\mathbf{p} + \mathbf{A}(t_s))$ encodes the laser field strength at the ionization instant t_s. The exponential term $e^{i(S(\mathbf{p}, t_s) + I_p t_s)}$ captures the quantum phase accumulated during the ionization process, where $S(\mathbf{p}, t_s)$ is the classical action and I_p is the ionization potential. Each term in the saddle-point sum corresponds to a distinct quantum trajectory contributing to the ionization process, with the prefactor weighting the relative importance of each pathway.

Building on our derivation of the nondipole Volkov state in Section 3.3.3, which incorporates both electric and magnetic field components of the laser interaction, we now implement the saddle-point method for the complete nondipole case. The treatment requires careful separation of the purely temporal and spatiotemporal components of the Volkov phase.

To achieve this separation systematically, we employ a Taylor expansion of the relevant trigonometric functions around $\mathbf{k}\cdot\mathbf{r} = 0$. Consider the general sinusoidal function

$$\sin(\mathbf{k}\cdot\mathbf{r} - \omega t + \phi) = \sin(f(\mathbf{r}, t)), \tag{4.22}$$

where $f(\mathbf{r}, t) \equiv \mathbf{k}\cdot\mathbf{r} - \omega t + \phi$. The Taylor expansion about $\mathbf{k}\cdot\mathbf{r} = 0$ yields

$$\sin(f) \approx \sin(-\omega t+\phi)+\cos(-\omega t+\phi)(\mathbf{k}\cdot\mathbf{r})-\frac{\sin(-\omega t+\phi)}{2}(\mathbf{k}\cdot\mathbf{r})^2+O((\mathbf{k}\cdot\mathbf{r})^3). \tag{4.23}$$

This expansion maintains excellent convergence for typical experimental parameters where $|\mathbf{k}\cdot\mathbf{r}| \ll 1$. The separation can be performed either before or after momentum integration without significant loss of accuracy, as demonstrated in [128].

The key insight from this expansion is that the nondipole Volkov phase can be decomposed into separable temporal and spatial components

$$\Gamma(\mathbf{r}, t) = \Gamma_1(t) + \mathbf{r}\cdot\mathbf{\Gamma}_2(t), \tag{4.24}$$

where the temporal component $\Gamma_1(t)$ contains all purely time-dependent terms, and the spatial component $\mathbf{\Gamma}_2(t) = -\partial_t\Gamma_1(t)\frac{\mathbf{k}}{\omega_\mathbf{k}}$ couples the spatial and temporal dynamics. This separation leads to a compact expression for the nondipole Volkov state:

$$\chi_\mathbf{p}(\mathbf{r}, t) = \frac{1}{(2\pi)^{3/2}}\exp\left[i\left(\mathbf{p} - \mathbf{\Gamma}_2(t)\right)\cdot\mathbf{r}\right]\exp\left[-i(\epsilon_p t + \Gamma_1(t))\right], \tag{4.25}$$

where $\epsilon_p = p^2/2$ is the kinetic energy of the freed electron. Here we only consider the solution in the velocity gauge. Using the vector potential defined in Eq. 3.38, we can explicitly evaluate the temporal phase component $\Gamma_1(t)$. The complete expression contains several physically distinct contributions:

$$\begin{aligned}
\Gamma_1(t) &= \sum_{j=0}^{2}\frac{\mathcal{A}_j^2}{4}\frac{-\omega_j t}{\eta_j(\mathbf{k})} + \frac{1-\epsilon^2}{1+\epsilon^2}\sum_{j=0}^{2}\frac{\mathcal{A}_j^2}{8\eta_j(\mathbf{k})}\sin(-2\omega_j t + 2\phi_{\text{cep}}) \\
&+ \sum_{i=0}^{1}\sum_{j=i+1}^{2}\frac{\mathcal{A}_i\mathcal{A}_j}{2(\eta_i(\mathbf{k}) - \eta_j(\mathbf{k}))}\sin(-(\omega_i - \omega_j)t) \\
&+ \frac{1-\epsilon^2}{1+\epsilon^2}\sum_{i=0}^{1}\sum_{j=i+1}^{2}\frac{\mathcal{A}_i\mathcal{A}_j}{2(\eta_i(\mathbf{k}) + \eta_j(\mathbf{k}))}\sin(-(\omega_i + \omega_j)t + 2\phi_{\text{cep}}) \\
&+ \sqrt{\frac{p_x^2 + \epsilon^2 p_y^2}{1+\epsilon^2}}\sum_{j=0}^{2}\frac{\mathcal{A}_j}{\eta_j(\mathbf{k})}\sin(-\omega_j t + \phi_{\text{cep}} - \varphi_p^{(\epsilon)}),
\end{aligned} \tag{4.26}$$

where $\varphi_p^{(\epsilon)} = \arctan\left(\frac{\epsilon p_y}{p_x}\right)$ represents the ellipticity-dependent momentum angle, and $\eta_j(\mathbf{k}) = 1 - \mathbf{k}\cdot\mathbf{p}/\omega_j$ accounts for the nondipole correction to the effective frequency. The complete nondipole transition amplitude, incorporating magnetic field effects, takes the form

$$T_0^{\mathrm{NDSP}}(\mathbf{p}) = \sum_{t_s} \langle \mathbf{p} - \mathbf{\Gamma}_2(t_s)|V(\mathbf{r})|\Psi_0\rangle \sqrt{\frac{2\pi i}{\partial_{t_s}^2 \Gamma_1(t_s)}} e^{i(\epsilon_p t_s + \Gamma_1(t_s) + I_p t_s)}, \tag{4.27}$$

where the superscript NDSP emphasizes the inclusion of nondipole effects. Several important modifications appear compared to the dipole case:

- The momentum shift $\mathbf{\Gamma}_2(t_s)$ in the matrix element accounts for the laser magnetic field's influence on the electron's asymptotic momentum
- The second derivative $\partial_{t_s}^2 \Gamma_1(t_s)$ replaces the simpler dipole denominator, reflecting the more complex temporal structure in the nondipole regime
- The phase factor now includes the nondipole temporal phase $\Gamma_1(t_s)$

This expression provides the foundation for computing photoelectron momentum distributions while fully accounting for the laser's magnetic field component.

The numerical implementation employs a uniform momentum grid with step size $\Delta p = 0.01$ a.u. in all three dimensions, spanning the range $p_i \in [-p_{\max}, p_{\max}]$ where $p_{\max} = \sqrt{2(2U_p + I_p)}$. This choice provides sufficient resolution to capture interference structures while maintaining computational tractability. The grid boundaries are determined by the laser intensity through U_p, ensuring all relevant photoelectron momenta are included.

Saddle-point solutions t_s are obtained by solving the nonlinear equation $\partial_t S(\mathbf{p}, t) = 0$ using the complex-plane Newton-Raphson iteration algorithms, with initial guesses informed by the peaks of the electric field. Only solutions satisfying $\mathrm{Im}(t_s) > 0$ and $\mathrm{Re}(t_s) \in [0, T_p]$ are retained. The phase-space weighting factor for each solution includes both the Hessian determinant and tunneling exponent

$$w_s = \left|\frac{2\pi i}{\partial_t^2 S(\mathbf{p}, t_s)}\right|^{1/2} \exp\left(i[S(\mathbf{p}, t_s)]\right)$$

Parallel computation is implemented using Julia's multiprocessing capabilities, distributing momentum points across available CPU cores. The task distribution follows a static scheduling approach where each process handles a distinct subset of the momentum grid, with load balancing optimized for the typical distribution of saddle-point search times. Interprocess communication is minimized by having each worker

compute and store its partial results independently, with only final probability amplitudes being collected.

In this chapter, we employed advanced mathematical techniques to simplify the calculation of the final transition amplitude. Specifically, we utilized the Jacobi-Anger expansion and the saddle-point method , providing detailed algorithms for identifying saddle points in the integration. In the next chapter, we will implement the full methodology developed thus far and present numerical results obtained within this framework. A key focus will be the comparative analysis of the saddle-point approximation and the Jacobi-Anger approach, highlighting their respective advantages and limitations. Additionally, we will systematically contrast the dipole and non-dipole regimes to elucidate their distinct physical implications.

5

RESULTS AND DISCUSSION

This chapter presents a comprehensive analysis of strong-field ionization dynamics, with a focus on few-cycle and structured laser pulses. The results are organized into four core themes, each addressing distinct aspects of photoelectron behavior through theoretical modeling. Building on the framework established in earlier chapters, we systematically investigate:

- The interplay between ultrashort pulse durations and ionization yields, including energy and polarization dependencies (5.1) [129].
- Quantum interference signatures in above-threshold ionization (ATI) spectra and their linkage to Volkov phase dynamics (5.2) [130].
- Nondipole effects in high-intensity regimes, emphasizing wavelength scaling and pulse-cycle dependencies (5.3) [131, 132].
- The role of orbital angular momentum (OAM) in modifying ATI structures when using twisted beams (5.4) [133].

The findings collectively reveal how non-trivial laser fields—whether through temporal confinement, phase structuring, or OAM coupling—can be harnessed to control electron emission.

5.1 IONIZATION IN FEW-CYCLE PULSE

The ionization dynamics of argon atoms exposed to circularly polarized laser pulses are investigated through photoelectron momentum distributions (PMDs), computed using two distinct theoretical frameworks: the Jacobi-Anger (JA) expansion and the saddle-point (SP) approximation. Figure 5.1 presents a comparative analysis of these methods for varying pulse durations, revealing their respective strengths in modeling ionization phenomena.

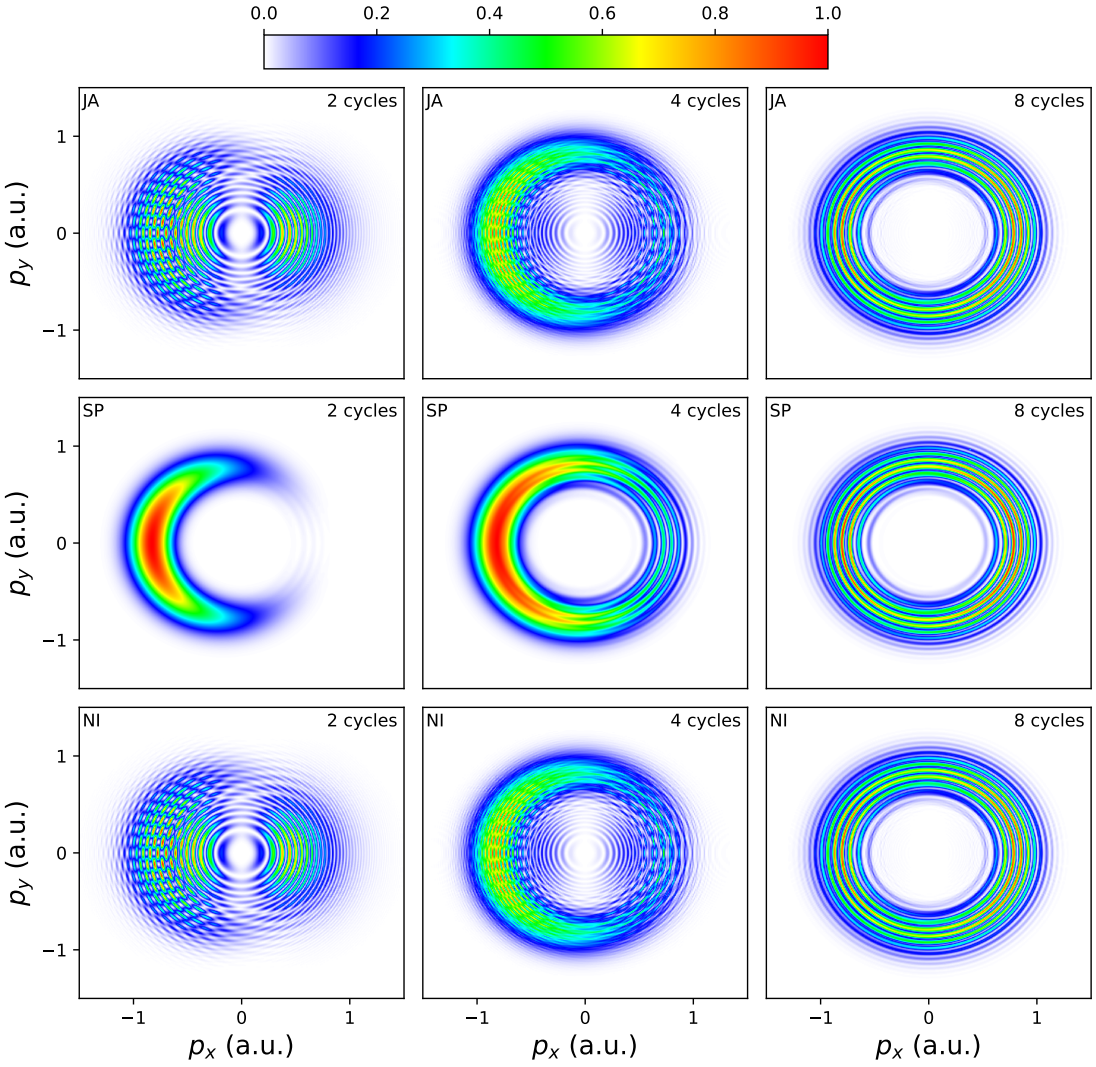

Figure 5.1: Photoelectron momentum distributions in the laser polarization plane for ionization of an argon atom by a circularly polarized laser pulse with a wavelength of 800 nm and peak intensity of 5×10^{14} W/cm^2. The top row (JA) presents results obtained using the Jacobi-Anger expansion, the middle row (SP) corresponds to the saddle-point method and the bottom row (NI) represents the results for numerical integration. Each column represents different pulse durations: two-cycle (left), four-cycle (middle), and eight-cycle (right) pulses. The color scale represents the normalized probability amplitude.

The interference structures observed in the PMDs are intrinsically linked to the spectral properties of the laser pulse (cf. [134]). As depicted in Fig. 2.2, the temporal profile and corresponding power spectrum of the pulse evolve significantly with duration. Shorter pulses (e.g., two cycles) exhibit a broad spectral distribution, facilitating numerous ionization pathways with comparable amplitudes. This spectral richness enhances quantum interference, leading to intricate oscillatory features in the momentum distributions. In contrast, longer pulses (four and eight cycles) pos-

sess a narrower frequency spectrum, resulting in more regular interference patterns, manifesting as distinct concentric rings.

The JA method (top row of Fig. 5.1) resolves fine interference structures, particularly for the two-cycle pulse, where high-frequency oscillations arise from coherent contributions of multiple ionization pathways. As the pulse extends to four and eight cycles, the PMDs transition into well-defined circular fringes, indicating reduced spectral broadening and more stable ionization dynamics.

In contrast, the SP method (bottom row of Fig. 5.1) emphasizes dominant ionization pathways by evaluating only the most significant saddle points. Consequently, it captures the gross features of the PMDs but omits finer interference details. For the two-cycle pulse, the distribution appears diffuse and lacks high-order oscillations seen in the JA results. With increasing pulse duration, the SP approximation produces clearer ring-like structures corresponding to dominant ionization phases.

The comparison reveals important trade-offs between computational accuracy and efficiency. While the JA expansion provides a complete quantum mechanical description including all interference effects, the SP method offers a computationally efficient alternative for identifying dominant ionization mechanisms. For the eight-cycle pulse, both methods converge to similar ring-like patterns, though the JA results retain weak interference features at low energies. This analysis underscores the need for method selection based on the desired balance between resolution and computational cost.

To directly compare the predictions of the JA and SP approaches, we also evaluated Eq. 4.1 by performing a full numerical integration using the Gauss–quadrature method. This calculation avoids the approximations inherent in either the JA expansion or the SP method, and therefore serves as a reference within the SFA framework. The resulting momentum distributions allow us to identify which features are preserved or lost in each approximation, and to assess the physical origin of the differences observed in Fig.5.1. The characteristic interference structures observed here are a hallmark of above-threshold ionization and are also visible in numerical solutions of the time-dependent Schrödinger equation [135]. However, in TDSE calculations these interference patterns appear rotated due to the influence of the Coulomb potential, an effect absent in the strong-field approximation. Moreover, Martiny *et al.* reported stronger interference at lower intensities compared to our results. This apparent discrepancy originates from the fact that they employ the peak intensity convention, with the vector potential amplitude defined as $A_0 = \sqrt{I_{\text{peak}}}/\omega$, whereas in our calculation the intensity is defined through the cycle-averaged relation $I(\mathbf{r}, t) = \frac{A_0^2 \omega^2 c}{8\pi}$. The difference between peak and cycle-averaged conventions leads to a discrepancy in the quoted intensities, which reconciles the results of the two approaches.

5.1.1 *Energy-Resolved Ionization Patterns in Strong Fields*

The characteristic energy distributions of ionized electrons are systematically examined through above-threshold ionization (ATI) spectra, calculated using two complementary theoretical approaches. Figure 5.2 displays these spectra as functions of normalized kinetic energy ε_p/ω, contrasting the saddle-point approximation (dashed red curves) with the full quantum mechanical treatment via Jacobi-Anger expansion (solid blue curves) for varying pulse durations and carrier-envelope phases.

The interplay between temporal confinement and spectral composition manifests distinctly in the calculated ATI patterns. For the shortest two-cycle pulses, the Jacobi-Anger results reveal intricate oscillatory features with characteristic energy spacings of 0.5 $\hbar\omega$ - a signature of broadband spectral interference that emerges from the pulse's substantial bandwidth. These quantum interference effects, while prominent in the complete theoretical treatment, are naturally absent in the saddle-point approximation due to its inherent focus on classical trajectory contributions.

As the interaction duration extends to four and eight optical cycles, both methods converge toward more regular peak structures, though with notable differences in spectral resolution. The gradual transition from complex interference patterns to distinct energy peaks reflects the narrowing spectral bandwidth with increasing pulse duration, as predicted by Fourier-transform relations. This evolution underscores the fundamental connection between temporal pulse characteristics and resulting electron energy distributions.

The carrier-envelope phase (CEP) demonstrates remarkable control over the ionization pathways, as evidenced by comparing $\varphi_{\text{cep}} = 0$ (upper panels) and π (lower panels) cases. The quantum mechanical treatment reveals CEP-dependent modifications to the interference structures, particularly for few-cycle pulses where the absolute phase strongly influences the temporal electric field profile.

Figure 5.3 provides mechanistic insight into these phase effects, showing how different CEP values modify the dominant ionization windows. At zero CEP, two primary saddle points contribute comparably to the ionization process, while at π CEP, a single dominant ionization channel emerges. This fundamental difference in strong-field dynamics explains the observed variations in spectral structure between the two phase conditions.

The Jacobi-Anger expansion comprehensively captures all quantum interference pathways, resolving subtle spectral features that emerge from coherent superposition of ionization amplitudes. This complete treatment proves particularly valuable for few-cycle pulses where broadband interference dominates the electron dynamics. Conversely, the saddle-point approximation provides a computationally efficient

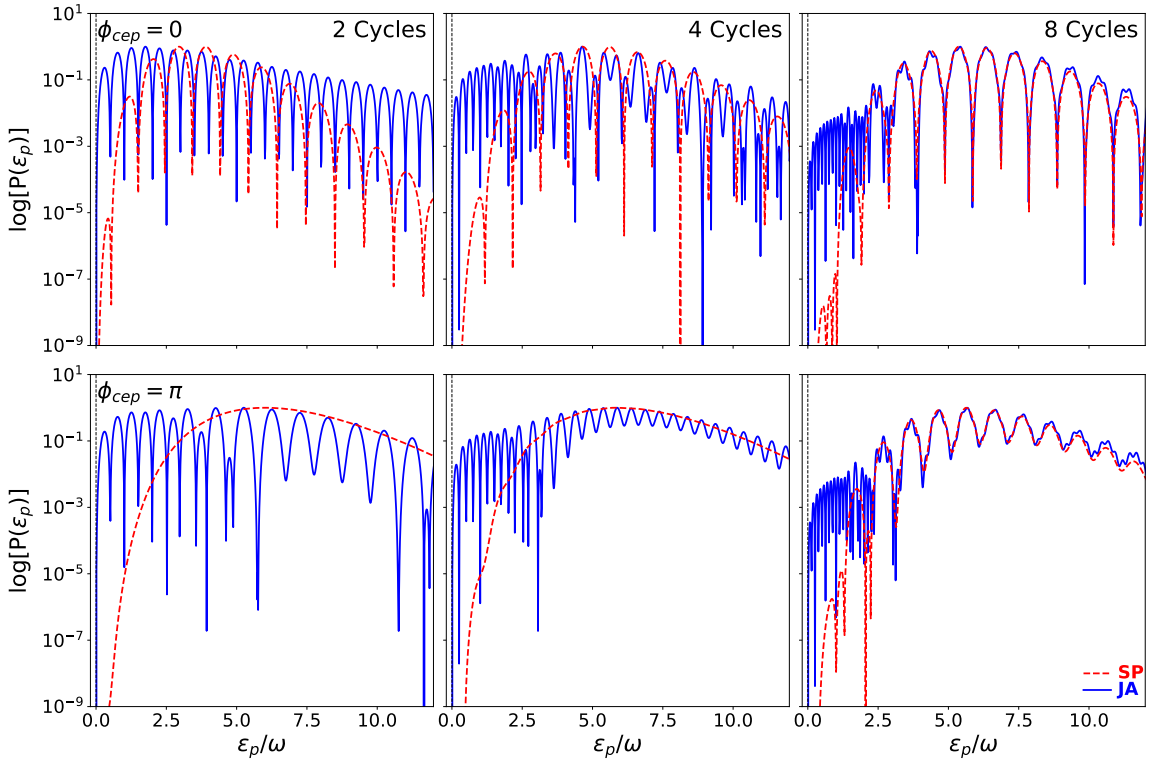

Figure 5.2: Energy-dependent ionization probability distributions for argon under 800 nm excitation (5×10^{14} W/cm^2). Top/bottom rows correspond to CEP values of $0/\pi$ respectively, while columns show increasing pulse durations from two cycles (left) to eight cycles (right). Solid blue curves represent complete quantum mechanical results (Jacobi-Anger), while dashed red curves show saddle-point approximation predictions.

framework that identifies dominant ionization mechanisms while naturally filtering out finer quantum interference effects. This approach yields satisfactory agreement for longer pulses where classical trajectory dominance emerges, though it necessarily misses the quantum mechanical subtleties apparent in the full treatment.

5.1.2 *Polarization-Dependent Electron Dynamics*

Figure 5.4 systematically examines how photoelectron momentum distributions (PMDs) transform as laser polarization transitions from linear to elliptical. The analysis focuses on a two-cycle pulse (800 nm, 5×10^{14} W/cm^2) interacting with argon atoms, with ellipticity ε varying from 0.0 (linear) to 0.75 (strongly elliptical).

For purely linear polarization ($\varepsilon = 0.0$), the PMD displays characteristic fringe patterns aligned with the polarization axis (p_x), arising from quantum interference between electron wave packets released at different field maxima. The saddle-point analysis in Fig. 5.6 identifies distinct ionization phases contributing to these patterns, with the asymmetric distribution reflecting the vectorial nature of the laser field.

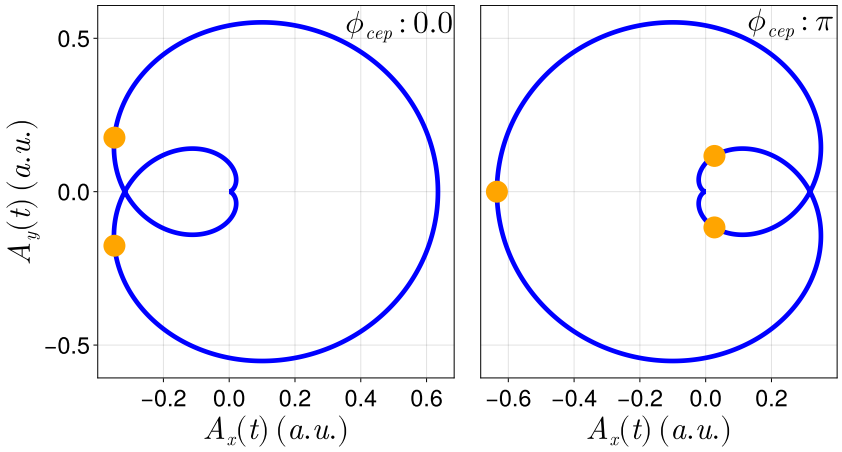

Figure 5.3: Temporal ionization dynamics for two-cycle pulses at constant kinetic energy of the photoelectron ($\epsilon_p = 5\omega$), showing vector potential profiles (black curves) and dominant saddle point locations (yellow markers) for (left) $\phi_{\text{CEP}} = 0$ and (right) π configurations. The distinct saddle point distributions explain the observed CEP-dependent spectral variations.

As ellipticity increases to $\varepsilon = 0.25$, the momentum distribution expands along the minor axis (p_y) while maintaining discernible interference structures. This evolution demonstrates how the introduction of orthogonal field components modifies electron trajectories without completely suppressing quantum coherence effects. The persistence of interference features indicates that multiple ionization pathways remain phase-correlated despite the altered field geometry.

At intermediate ellipticity ($\varepsilon = 0.5$), the PMD undergoes a qualitative transformation, splitting into two symmetric lobes that trace the polarization ellipse. This bifurcation marks the onset of classical-like behavior, where electron emission follows the instantaneous field direction rather than exhibiting pure quantum interference. The saddle-point analysis reveals that this transition corresponds to a decoherence effect, as phase relationships between different ionization times become disrupted by the rotating field vector.

For near-circular polarization ($\varepsilon = 0.75$), the momentum distribution collapses to two well-defined lobes aligned with the major polarization axis, completely lacking interference structures. This final state represents the classical limit where electron trajectories become fully determined by instantaneous field conditions rather than wave packet interference.

Figure 5.5 extends this analysis to the propagation plane, revealing how ellipticity affects out-of-plane electron dynamics. Under linear polarization, the (p_x, p_z) distribution shows clear interference fringes while the (p_y, p_z) plane remains rotationally symmetric - a direct consequence of the field's single-axis oscillation.

With increasing ellipticity, three key changes emerge:

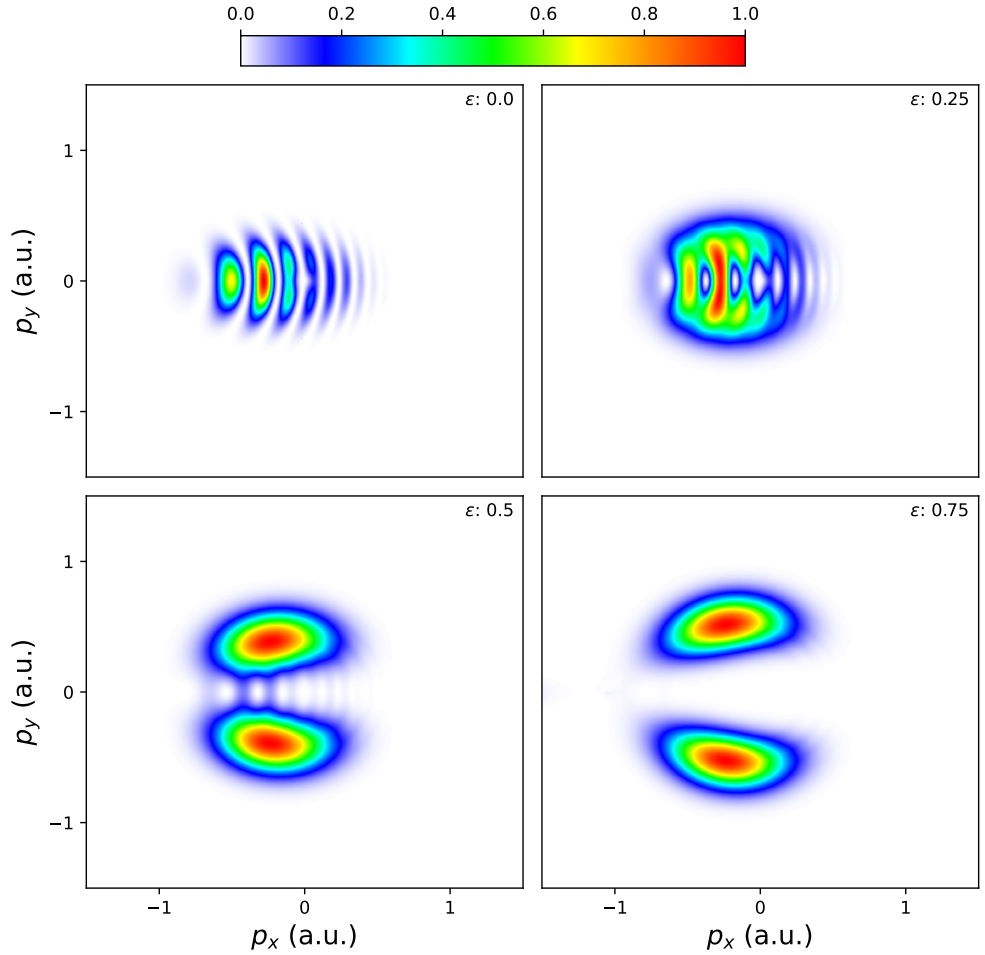

Figure 5.4: Photoelectron momentum distributions in the laser polarization plane for ionization of an argon atom by a two-cycle laser pulse with a wavelength of 800 nm and peak intensity of 5×10^{14} W/cm^2. The ellipticity ε of the laser field is varied from $\varepsilon = 0.0$ (top-left) to $\varepsilon = 0.75$ (bottom-right). The color scale represents the normalized probability amplitude.

- The (p_x, p_z) interference patterns gradually disappear as phase coherence diminishes
- The (p_y, p_z) distribution develops anisotropic features aligned with the polarization ellipse
- Both planes exhibit progressive momentum redistribution toward classical predictions

These observations collectively demonstrate how ellipticity serves as a control parameter for transitioning between quantum-interference-dominated and classical-trajectory-dominated strong-field ionization regimes.

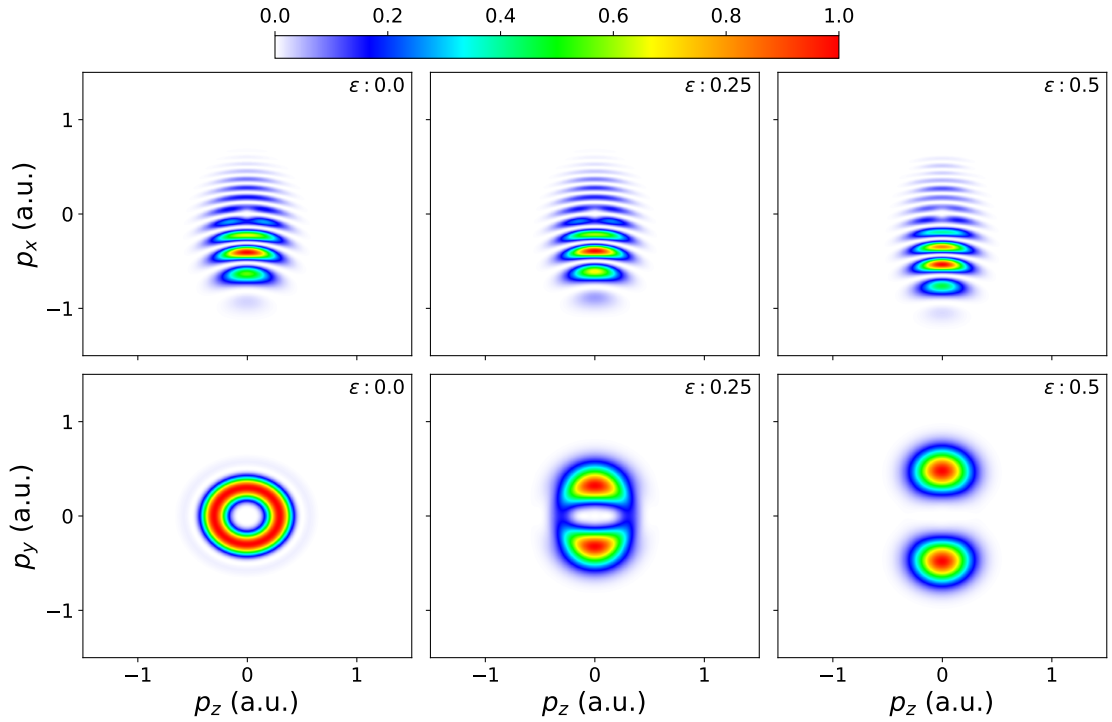

Figure 5.5: Photoelectron momentum distributions in the laser propagation plane for ionization of an argon atom by a two-cycle laser pulse with a wavelength of 800 nm and peak intensity of 5×10^{14} W/cm^2. The distributions are shown in the (p_x, p_z) plane (top row) and the (p_y, p_z) plane (bottom row), where the ellipticity ε of the laser field is varied from $\varepsilon = 0.0$ (left) to $\varepsilon = 0.5$ (right). The color scale represents the normalized probability amplitude.

5.2 NONLINEAR INTERFERENCE IN STRONG-FIELD IONIZATION

The phenomenon of nonlinear interference in strong-field ionization arises from the coherent superposition of multiple quantum pathways available to photoelectrons during the ionization process. When atoms interact with intense laser fields, electrons can be liberated through various temporal windows within the optical cycle, each acquiring distinct quantum phases during their subsequent propagation in the continuum. These phase differences lead to constructive and destructive interference patterns that manifest in both the energy and momentum distributions of the emitted photoelectrons. The interference structures contain rich information about the ionization dynamics, including the relative contributions of different temporal ionization windows, the accumulation of quantum phase during electron propagation, and the influence of laser parameters on the final electron state. In particular, the interplay between the laser's electric field oscillations and the pulse envelope creates complex interference patterns that evolve characteristically with pulse duration, as the number

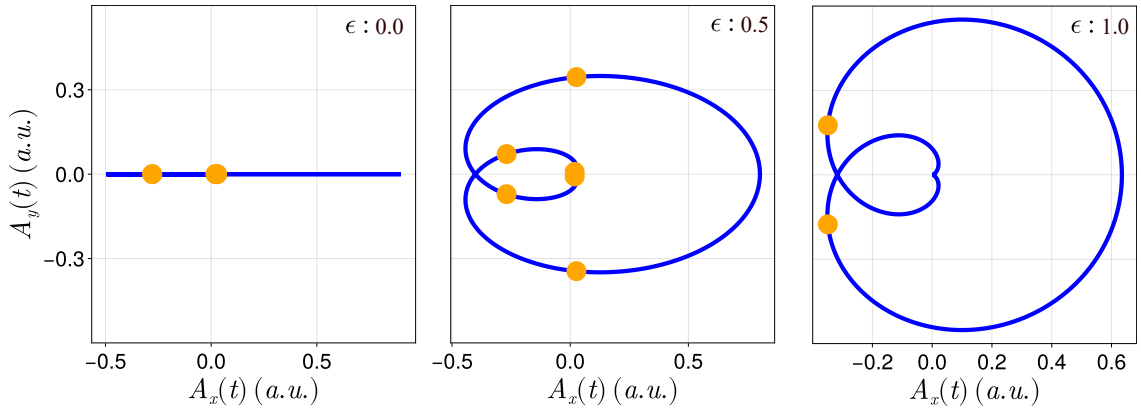

Figure 5.6: Vector potential for a two-cycle laser pulse at a fixed $\phi_{\text{CEP}} = 0$ while varying the ellipticity ϵ. The panels show ellipticity values of $\epsilon = 0.0$, $\epsilon = 0.5$, and $\epsilon = 1.0$, respectively. The yellow dots represent saddle-point solutions, indicating critical points for ionization that shift with changes in the ellipticity. The other parameters are same as Fig. 5.3

of contributing ionization pathways increases while their relative phase relationships become more intricate.

5.2.1 *Interference Patterns in ATI Peaks and Photoelectron Momentum Distributions*

Figure 5.7 presents a systematic investigation of photoelectron energy and momentum distributions for laser pulses comprising 2, 4, and 8 optical cycles. The ATI spectra reveal distinct peaks that correspond directly to concentric rings in the momentum distributions at $p_z = 0$, where inner rings represent low-energy photoelectrons and outer rings correspond to higher kinetic energies. These distributions predominantly feature photoelectrons with intermediate kinetic energies, as the extreme energy ranges typically exhibit lower emission probabilities.

The momentum distributions demonstrate significant evolution with increasing pulse duration. The inner ring structures rapidly dissipate as the number of cycles grows, while the outer rings undergo noticeable broadening. This behavior mirrors corresponding changes in the ATI spectra, where peak intensities decrease and widths increase with longer pulses. Notably, additional features emerge in the ATI spectra at higher photoelectron energies, characterized by broader peaks with superimposed oscillatory structures.

To elucidate these oscillations, we derive the Volkov state solution using the vector potential of a circularly polarized pulse ($\epsilon = 1.0$). Through Jacobi-Anger expansion of the Volkov phase, we obtain:

$$\chi_{\mathbf{p}}(\mathbf{r}, t) = (2\pi)^{-3/2} \prod_{i=1}^{5} \sum_{n_i=-\infty}^{\infty} J_{n_i}(x_i) e^{-i(E_N t - \mathbf{p}\cdot\mathbf{r} - \Phi_N)} \tag{5.1}$$

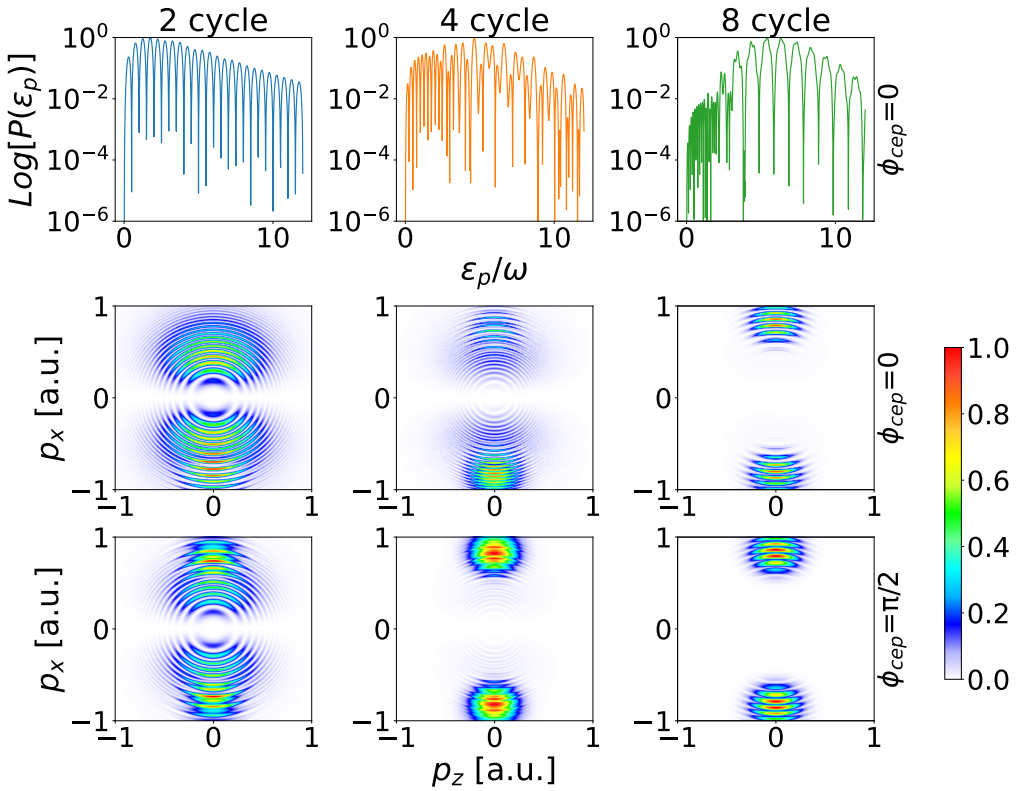

Figure 5.7: Photoelectron distributions for 800 nm laser pulses (5×10^{14} W/cm^2) interacting with argon ($I_p = 15.7596$ eV). Top row displays ATI spectra versus ϵ_p/ω at $p_z = 0$. Middle and bottom rows show (p_x, p_z) momentum distributions for CEP values of 0 and $\pi/2$ respectively. Columns represent pulse durations of 2 cycles (left), 4 cycles (middle), and 8 cycles (right).

The summation index n_i enumerates absorbed photons, while the Bessel function arguments x_1 through x_5 take specific forms: $x_1 = U_p n_p/2\omega$, $x_2 = U_p n_p/16\omega$, $x_3 = \rho_0/2$, $x_4 = -\rho_0/4(1 - 1/n_p)$, and $x_5 = -\rho_0/4(1 + 1/n_p)$. Here, $\rho_0 = A_0 p \sin\theta_p/\sqrt{2}\omega$ represents a scaled momentum parameter, and U_p denotes the ponderomotive energy. The modified photoelectron energy E_N incorporates multiple contributions:

$$E_N = \frac{\mathbf{p}^2}{2} + \frac{3U_p}{8} + \left(-\frac{n_1}{n_p} + \frac{2n_2}{n_p} + n_3 + n_4\left(1 - \frac{1}{n_p}\right) + n_5\left(1 + \frac{1}{n_p}\right)\right)\omega \tag{5.2}$$

Similarly, the modified phase ϕ_N depends on angular parameters:

$$\phi_N = (n_3 + n_4 + n_5)(\phi_{\text{CEP}} - \Lambda\varphi_p) \tag{5.3}$$

These relationships satisfy the energy conservation condition:

$$\left(\frac{-n_1 + 2n_2 - n_4 + n_5}{n_p} + n_3 + n_4 + n_5\right)\omega = N\omega \tag{5.4}$$

where N represents the net photon order. This equation fundamentally governs the final photoelectron kinetic energy, with $N\omega$ specifying the absorbed photon energy and the n_i parameters describing fractional photon contributions.

The complete energy conservation relation for ATI processes becomes:

$$\epsilon_p = N\omega - \left(\frac{3U_p}{8} + I_p\right) \tag{5.5}$$

The cyclical peaks in Fig. 5.7 emerge from this quantized energy absorption, modulated by Bessel function behavior in the Volkov state. While peak spacing generally reflects the photon energy ω, deviations occur due to the complex interplay between different absorption pathways, as detailed in our supplementary materials.

The ponderomotive energy U_p significantly influences peak positions through its dependence on field oscillations. Few-cycle pulses exhibit substantial U_p variations across cycles, leading to incoherent alignment of ionization amplitudes at different energies. This results in peak shifting - toward lower energies near field maxima and higher energies at lower intensities.

The Bessel parameters x_i reveal distinct physical mechanisms. Parameters x_1 and x_2 relate to pulse envelope energy, while x_{3-5} describe nonlinear response components. The envelope terms vary with optical cycle count, causing faster oscillations in longer pulses. The nonlinear terms additionally depend on photoelectron momentum, producing momentum-dependent interference effects. For few-cycle pulses, envelope effects dominate at lower energies (Fig. 5.7), while longer pulses exhibit enhanced interference from both mechanisms at higher energies.

Pulse duration also influences the spatial characteristics of the electron momentum distributions. As demonstrated in Fig. 5.8, the full width at half maximum (FWHM) of dominant interference rings decreases with increasing cycle number. This narrowing reflects the improved ability of electrons to adiabatically respond to field variations in longer pulses, leading to more localized momentum distributions. In contrast, few-cycle pulses produce broader and less distinct interference patterns due to the non-adiabatic nature of the electron dynamics under rapidly varying fields.

5.2.2 *Role of Volkov Phases in Interference Phenomena*

The dynamics of Volkov phases play a crucial role in shaping the interference patterns observed in strong-field ionization processes. Figure 5.9 illustrates how the phase evolution varies with electron momentum and laser pulse characteristics. At an intermediate momentum of $p = 0.5$ a.u., the Volkov phase exhibits pronounced oscillatory behavior, particularly near the extrema of the laser's vector potential. These oscillations

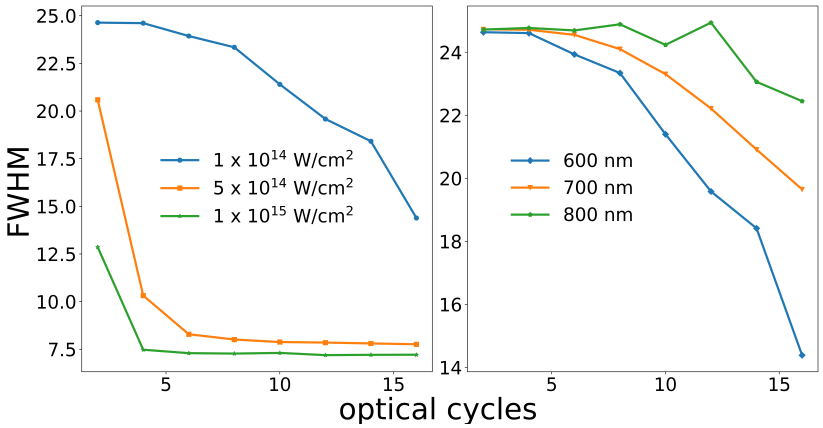

Figure 5.8: FWHM evolution of dominant momentum rings. Left: Fixed $\lambda = 600$ nm, varying intensity. Right: Fixed $I = 10^{14}$ W/cm^2, varying wavelength. Dashed lines indicate trends.

become increasingly intense as the pulse duration lengthens, reflecting the cumulative effect of the laser field on the electron's quantum phase over time.

For few-cycle pulses (e.g., 2 cycles), the phase structure is characterized by broad peaks, which arise due to the contributions of multiple frequency components in the short pulse spectrum. In contrast, longer pulses lead to sharper and more rapid phase oscillations, as the phase differences between different spectral components diminish, resulting in a more coherent accumulation of phase shifts.

At lower momenta ($p = 0.1$ a.u., Fig. 5.10), the phase evolution is dominated by the envelope energy of the laser pulse rather than the carrier frequency. This results in simpler temporal patterns, where the phase variations are primarily dictated by the slow modulation of the pulse envelope rather than the fast oscillations of the electric field.

The observed behavior under a $\sin^2$ envelope is likely generalizable to other trigonometric pulse shapes (e.g., cosine, trapezoidal), as these share similar discrete spectral properties. However, Gaussian envelopes, which possess a continuous frequency spectrum, would lead to qualitatively different interference effects. The absence of sharp spectral features in a Gaussian pulse reduces the contrast of interference fringes and introduces additional complexity in the analysis due to the smooth and broadened spectral distribution.

5.3 NONDIPOLE EFFECTS IN FEW-CYCLE PULSES

In the preceding sections, the analysis was restricted to the dipole approximation, where the laser field is treated as spatially uniform and only the electric component of

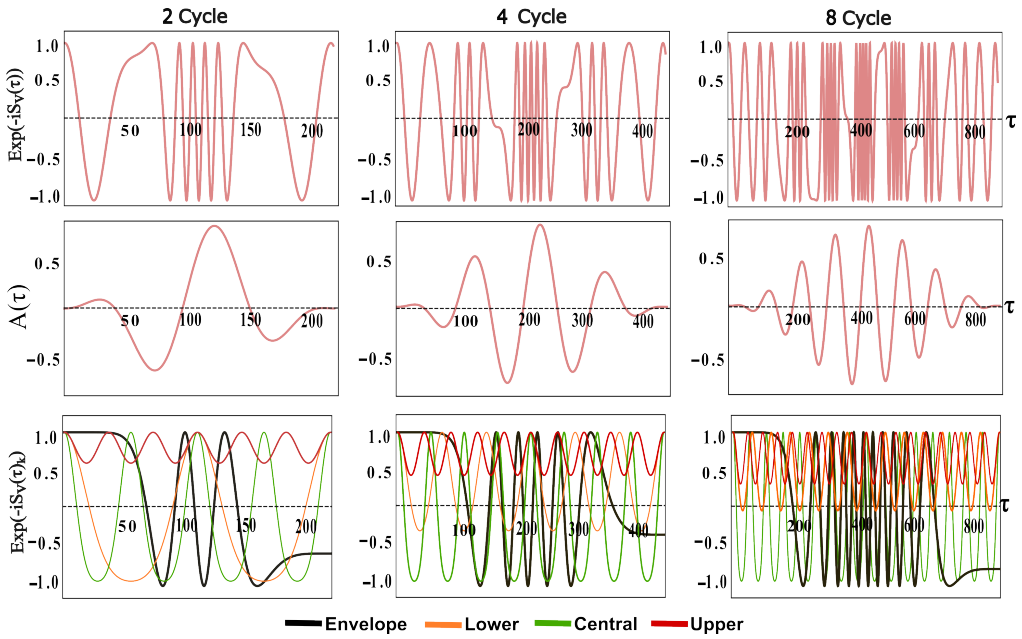

Figure 5.9: Volkov phase evolution at $p = 0.5$ a.u. for 800 nm pulses (5×10^{14} W/cm^2). Top row: complete phase. Bottom row: individual component contributions. Columns show 2, 4, and 8 cycle durations. Middle row displays vector potential profile (arbitrary units). Parameters: $\beta = 0$, $\theta_p = \pi/2$. The plotted quantity corresponds to the real part Re$[e^{S_v(\mathbf{p},t)}]$, which governs the interference structure in the photoelectron spectra.

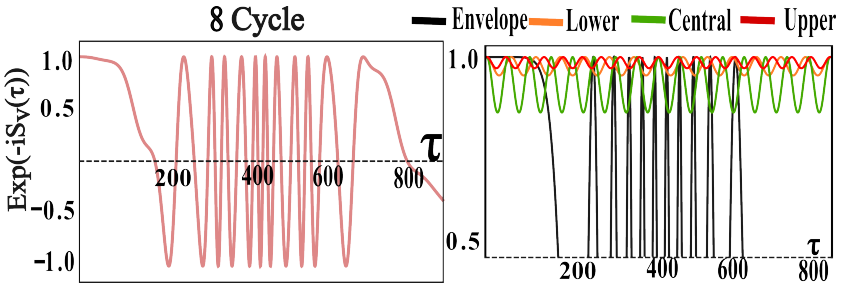

Figure 5.10: Temporal evolution of a Volkov phase for an 8-cycle pulse. The left panel shows the composite effect of the temporal evolution of Volkov phase within the laser pulse, while the right panel focuses on the contribution from the primary two terms. The laser parameters are the same as those in Fig. 5.9, except for the parameter p, which is set to 0.1 a.u. The plotted quantity corresponds to the real part Re$[e^{S_v(\mathbf{p},t)}]$, which governs the interference structure in the photoelectron spectra.

the field is considered. At high intensities and long wavelengths, however, the magnetic field and the spatial dependence of the laser vector potential begin to play a measurable role in the electron dynamics. These so-called nondipole effects lead to observable signatures such as momentum shifts along the laser propagation direction and asymmetries in the photoelectron momentum distributions. In this section, we investigate how such nondipole corrections manifest in above-threshold ionization by examining the peak displacement of the photoelectron spectra and comparing

it with predictions from both the dipole and nondipole strong-field approximations. The peak displacement (ΔP_z) observed in above-threshold ionization spectra arises from a complex interplay between laser parameters and atomic characteristics. This displacement magnitude correlates strongly with laser intensity, as stronger fields induce more pronounced electron-field interactions. As demonstrated in Fig. 5.11, comparative analysis between Argon and Neon reveals significant discrepancies between plane-wave theoretical predictions and experimental measurements, while pulsed-field models show improved agreement despite the limited data points shown in the visualization.

An important distinction between the present model and earlier nondipole theories lies in the treatment of the laser field. While most analytical formulations assume a monochromatic plane wave, the present work employs a finite, few-cycle pulse with an explicit spatial dependence of the field envelope, $\mathbf{A}(\mathbf{r},t) = \mathbf{A}(t-\mathbf{k}\cdot\mathbf{r}/\omega)f(\mathbf{r},t)$. This spatial $\mathbf{k}\cdot\mathbf{r}$ dependence of the envelope introduces a ponderomotive, or time-averaged, Lorentz-force correction that contributes an additional longitudinal force term,

$$\Delta F_{L,z} = -\frac{\partial U_p}{\partial z}, \tag{5.6}$$

where U_p is the ponderomotive energy. This term accounts for the envelope-induced momentum transfer along the propagation direction, which becomes particularly relevant for short pulses where the field intensity changes rapidly in space and time. Consequently, our predictions exhibit better agreement with experimental results compared to monochromatic nondipole theories, since the inclusion of the pulse envelope captures the realistic temporal and spatial structure of the driving field.

5.3.1 *Laser Parameter Dependencies*

The ATI spectrum exhibits substantial sensitivity to laser pulse characteristics including duration [136], intensity [137], and wavelength [57], with consequent effects on photoelectron angular distributions. Single-cycle pulses generate isotropic emission patterns since the brief interaction window prevents directional preference establishment. In contrast, multi-cycle pulses produce anisotropic distributions (Fig. 5.12) through sustained field interactions that impart directional bias to liberated electrons.

Spectral properties further influence emission patterns through wavelength-dependent effects. Short-wavelength radiation promotes anisotropic distributions via temporally concentrated field interactions, while long-wavelength excitation yields more isotropic patterns due to reduced temporal focusing. Intensity variations [138] introduce additional complexity, with higher intensities extending interaction durations and pro-

moting emission alignment with the electric field vector. These parameters interact through nonlinear mechanisms to determine the ultimate angular distribution characteristics.

Detailed examination of propagation-plane distributions (Fig. 5.12) reveals several key relationships between laser parameters and angular emission properties. Pulse duration emerges as particularly influential under high-intensity, wavelength at 800 nm conditions. At lower parameter values, dipole and non-dipole calculations produce nearly identical results (Fig. 5.12a), while elevated intensities reveal clear cycle-dependent variations (Fig. 5.12b-c). These effects become less pronounced at longer wavelengths (Fig. 5.12d).

Analysis conducted at peak photoelectron energies accounts for ATI peak splitting effects [139] that accompany pulse duration variations. The magnitude of these energy shifts demonstrates positive correlation with intensity and inverse correlation with wavelength. Non-dipole contributions remain remarkably stable across pulse duration variations, with magnetic field influences becoming negligible for extended pulses at either high intensities or long wavelengths. This observation aligns with established theoretical understanding [140] of monochromatic field ionization processes. The momentum-space asymmetry evident in Fig. 5.13 demonstrates unam-

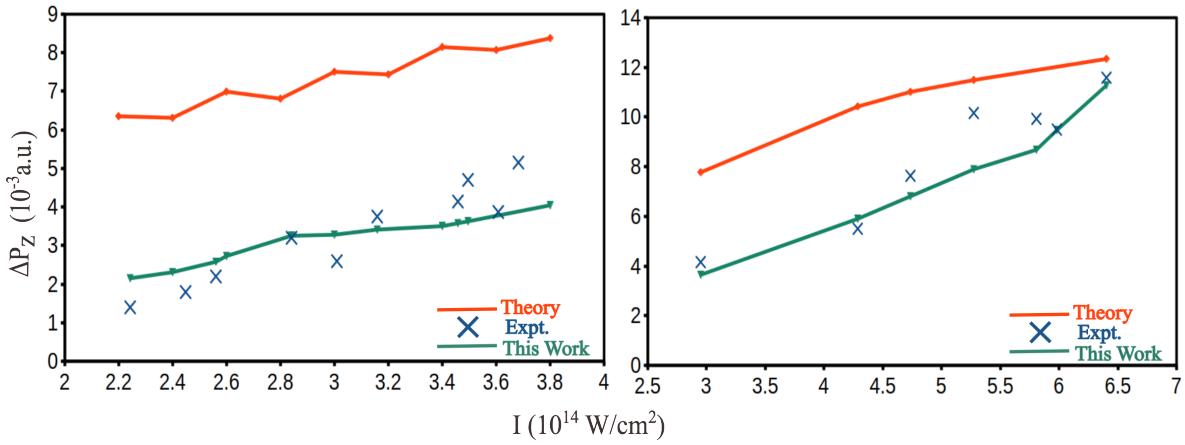

Figure 5.11: The peak shift ΔP_z of the maxima in ATI spectra are plotted as a function of laser intensity I for a circularly polarized 800 nm, 15 fs laser pulse. Results are shown for two different atomic targets, Ar (left) and Ne (right), and are compared to previous experimental (blue-crosses) and theoretical work: orange (Ref. [105]), blue (Ref. [96]), and green (this work).

biguous signatures of nondipole interactions during strong-field ionization, characterized by systematic photoelectron momentum shifts along the propagation axis. Comparative analysis of 800 nm and 1200 nm pulses reveals wavelength-dependent forward displacements (positive p_z values), with the longer wavelength exhibiting slightly enhanced deflection magnitude.

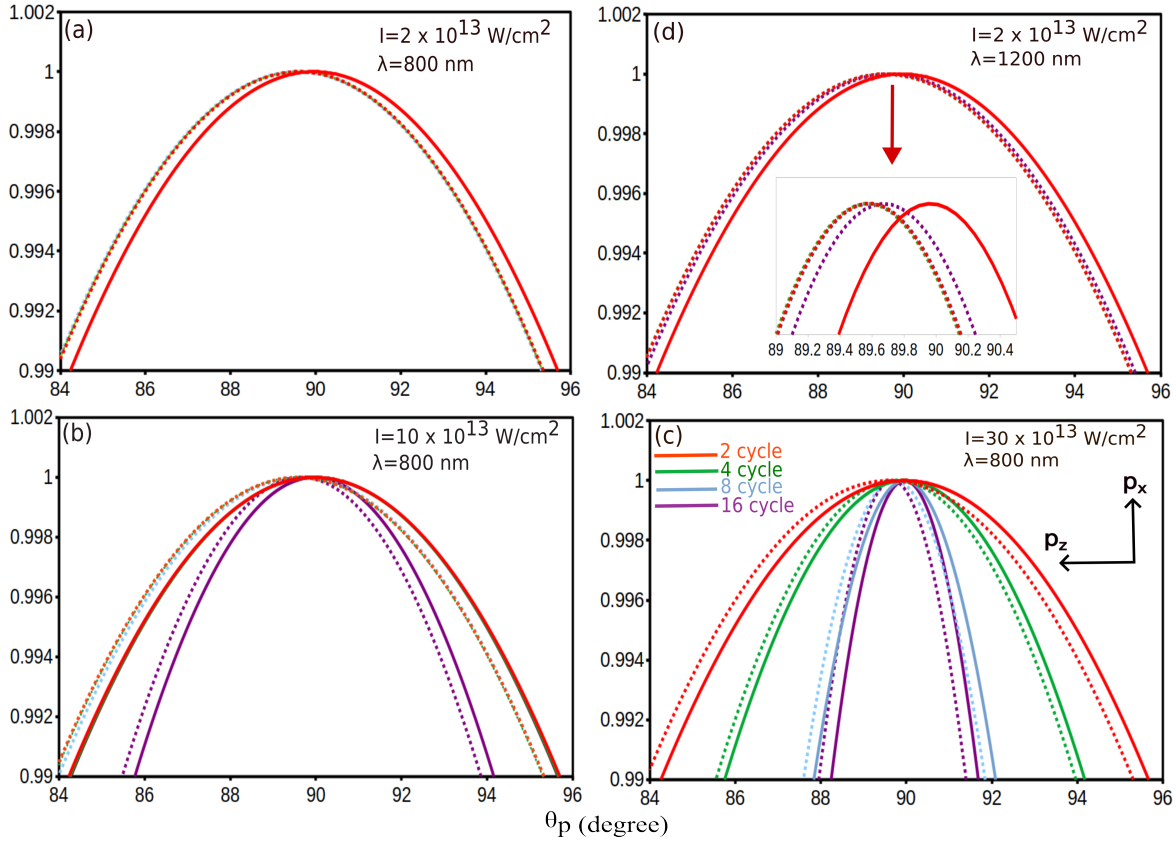

Figure 5.12: Normalized polar angular distribution (PAD) in the propagation ($p_x - p_z$) plane ($\varphi_p = 0$) for argon interacting with a circularly polarized sine-squared pulse. The laser wavelengths of 800 nm and 1200 nm are used with intensities ranging between $I = 2 \times 10^{13} - 30 \times 10^{13} \mathrm{W/cm^2}$. The pulse duration is varied with different numbers of optical cycles ($n_p = 2, 4, 8, 16$) and photoelectron energy ($\epsilon_{p,max}$), at which the maximum ionization probability occurs, is kept constant. The Lorentz force acts on the electron, causing it to be pushed in the direction of laser propagation. The results from both dipole (solid curve) and nondipole (dotted curve) computations are shown.

The right panel of Fig. 5.13 presents a quantitative examination of peak displacement (Δp_z) versus laser intensity, highlighting the critical role of nondipole phenomena. The Jacobi-Anger (JA) approach demonstrates remarkable agreement with experimental measurements across all intensity values, successfully reproducing both the absolute shift magnitudes and their intensity scaling. This correspondence validates the JA method's fundamental treatment of photon momentum transfer through its Bessel-function framework, which naturally incorporates wavelength dependence without requiring trajectory-based simplifications.

Conversely, the saddle-point approximation exhibits systematic deviations, particularly at lower intensities, where it underestimates the observed shifts. This shortcoming stems from the perturbative treatment of magnetic field effects within a classical

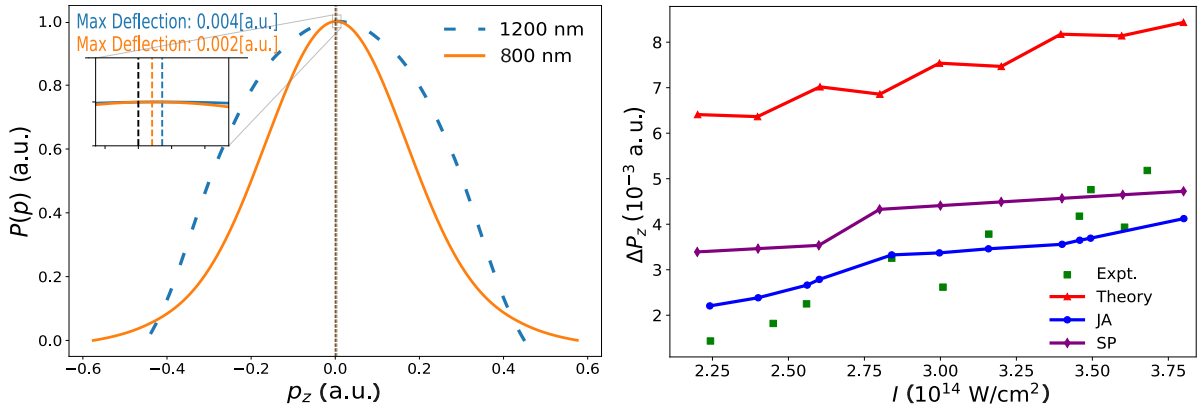

Figure 5.13: **Left:** Momentum-space ionization probability $P(\mathbf{p})$ for 2-cycle circularly polarized pulses at 800 nm (orange) and 1200 nm (blue), intensity 5×10^{14} W/cm^2. Wavelength-dependent forward shifts ($p_z > 0$) are apparent, with detailed structure shown in the inset. **Right:** Intensity dependence of Δp_z for 800 nm, 15 fs pulses, comparing JA and saddle-point methods with experimental data [96] and theoretical benchmarks [105].

trajectory framework, which becomes inadequate when the electron quiver motion approaches the laser wavelength scale.

5.3.2 *Wavelength-Scaling of Nondipole Phenomena*

Figure 5.14 offers detailed insight into wavelength-dependent nondipole effects during argon atom ionization by circularly polarized pulses. The comparative visualization of dipole and nondipole photoelectron momentum distributions (PMDs) demonstrates progressively stronger deviations with increasing wavelength, emphasizing the necessity of full nondipole treatments, especially in mid-infrared regimes.

The dipole approximation results (left panel, 3200 nm) exhibit perfect p_z symmetry, reflecting the assumed magnetic field negligibility that simplifies theoretical analysis. While valid for short wavelengths and moderate intensities, this assumption breaks down severely in longer-wavelength regimes, as evidenced by the middle and right panels (3200 nm and 4200 nm nondipole calculations).

The nondipole PMDs reveal two key phenomena, systematic positive p_z shifts reaching 0.1 a.u. at 4200 nm and radiation pressure effects that scale nonlinearly with wavelength. These effects originate from magnetic field-induced momentum transfer along the propagation axis, becoming increasingly dominant at mid-infrared wavelengths. The growing peak displacement from $p_z = 0$ provides direct evidence of radiation pressure influence on liberated electrons, with important implications for experimental interpretation in long-wavelength regimes.

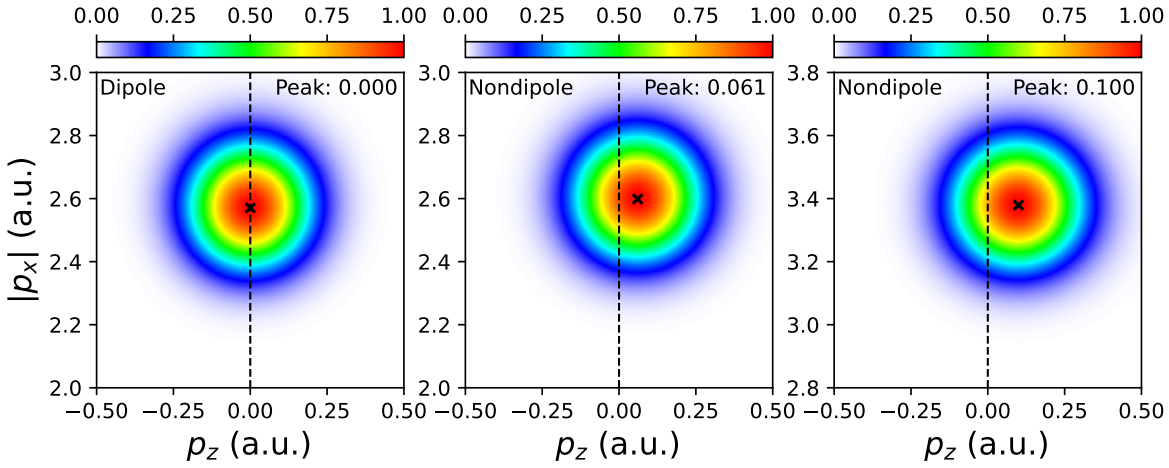

Figure 5.14: Dipole vs. nondipole PMD comparison for argon ionization by circularly polarized pulses ($5{\times}10^{14}$ W/cm^2), displayed in $(|p_x|, p_z)$ coordinates. Left: Dipole result at 3200 nm. Middle/Right: Nondipole results for 3200 nm and 4200 nm. Dashed lines indicate $p_z = 0$ reference, with crosses marking probability maxima. The color scale represents normalized probability density, highlighting the growing p_z displacement with wavelength under nondipole conditions.

5.3.3 *Pulse-Cycle Dependence in Non-Dipole ATI Dynamics*

In strong-field ionization, the number of optical cycles within a laser pulse critically governs the electron dynamics during and after ionization. Unlike the dipole approximation, where the magnetic field component is neglected, non-dipole ATI explicitly accounts for this interaction, leading to asymmetric photoelectron momentum distributions. This asymmetry manifests as a systematic shift (ΔP_z) of spectral peaks along the laser propagation direction, as quantified in Fig. 5.15.

The observed peak displacements arise from three interrelated physical mechanisms. First, the magnetic field component of the laser breaks the symmetry of the electron wave packet, imparting a directional bias to the photoelectron momentum. Second, with increasing pulse cycles, the liberated electron experiences prolonged interaction with the laser field, amplifying the asymmetry through cumulative momentum transfer. Third, quantum interference between electron wave packets generated in successive cycles modifies the spectral structure, as theoretically predicted in [100]. These effects collectively explain the intensity- and cycle-dependent shifts visible in Fig. 5.15.

Comparative analysis of krypton and argon targets reveals subtle but consequential differences in peak shift magnitudes. The atomic species dependence arises from variations in ionization potentials and electronic structure, which influence both the initial ionization step and subsequent laser-driven electron dynamics. Figure 5.15 isolates these target-specific effects while holding pulse parameters constant, thereby highlighting the role of optical cycles independent of other variables. The data demon-

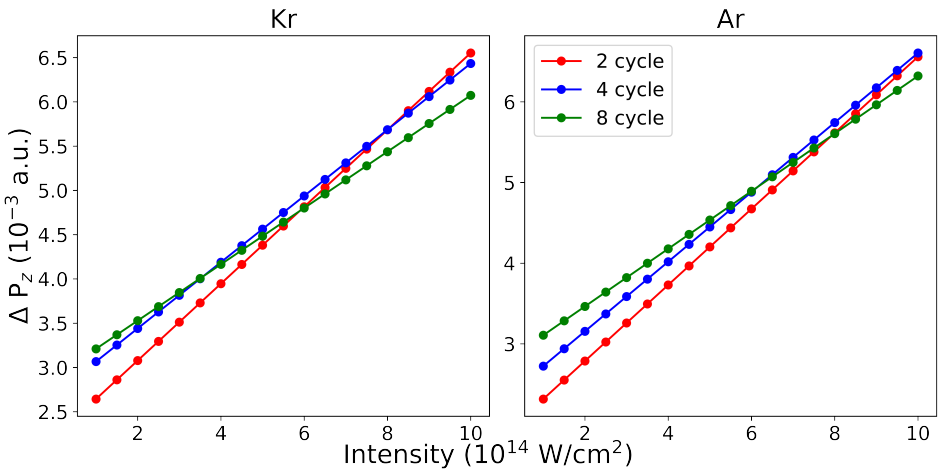

Figure 5.15: Measured peak shifts ΔP_z in ATI spectra as a function of laser intensity I for krypton (left) and argon (right) targets. The laser wavelength and intensity are maintained at 700 nm and 5×10^{14}W/cm^2, respectively..

strate that while the general trend of increasing ΔP_z with intensity is universal, its magnitude and fine structure are sensitive to the target atom.

5.4 STRONG-FIELD IONIZATION WITH TWISTED BEAMS

While previous sections employed the velocity gauge to describe strong-field ionization with plane-wave pulses, the analysis of twisted beams (e.g., Bessel pulses carrying orbital angular momentum, OAM) necessitates a switch to the length gauge. This choice is motivated by three key factors:

- **Physical Intuition in Non-Perturbative Regimes:** The length gauge's interaction term, $\mathbf{E}(t) \cdot \mathbf{r}$, directly couples the electric field to the electron's position, offering a clearer interpretation of tunneling ionization,a dominant process in SFI. For twisted beams, where the field has spatially varying phase (e.g., $e^{im_\gamma \phi}$) and intensity profiles, this gauge naturally captures the interplay between the OAM-induced structured field and the electron's escape dynamics.

- **Alignment with Stationary-Phase Methods:** The saddle-point analysis (Fig. 5.16) relies on identifying critical times t_s when the electron couples to the field to reach a final energy ϵ_p. The length gauge's explicit dependence on $\mathbf{r}$ simplifies the connection between saddle points and the **spatial structure** of twisted beams, particularly for the enhanced z-component observed at higher m_γ.

- **Gauge Consistency for Structured Fields:** Unlike plane waves, twisted beams exhibit non-trivial longitudinal fields (e.g., $E_z \neq 0$) and phase singularities. The velocity gauge's $\mathbf{p} \cdot \mathbf{A}$ interaction complicates momentum-space interpretations

due to artificial gauge shifts, while the length gauge avoids these ambiguities, ensuring a direct link to observable photoelectron distributions.

In the general formulation (Eq. 4.20), the transition amplitude was expressed via the saddle-point approximation as

$$T_0^{\mathrm{SP}}(\mathbf{p}) = \sum_{t_s} V^L(\mathbf{q}, t_s) \sqrt{\frac{2\pi i}{\mathbf{E}(t_s) \cdot [\mathbf{p} + \mathbf{A}(t_s)]}} e^{i[S(\mathbf{p}, t_s) + I_p t_s]}, \tag{5.7}$$

where $S(\mathbf{p}, t_s)$ is the classical action evaluated at saddle points t_s, and $V^L(\mathbf{p}, t_s)$ contains the pre-exponential factors including the dipole matrix element. Here we used short notation for $\mathbf{q} = \mathbf{p} + \mathbf{A}(t_s)$. However, for twisted beams with orbital angular momentum m_γ, the matrix elements develop singularities when

$$\langle \mathbf{q} | \mathbf{r} \cdot \mathbf{E}(\mathbf{r}) | \psi_0 \rangle \sim \int d^3r \, e^{-i\mathbf{q}\cdot\mathbf{r}} \mathbf{r} \cdot \mathbf{E}_{m_\gamma}(\mathbf{r}) \psi_0(\mathbf{r}) \tag{5.8}$$

where $\mathbf{E}_{m_\gamma}(\mathbf{r})$ contains phase singularities of the form $e^{i m_\gamma \phi} r^{|m_\gamma|}$ near the optical vortex ($r \to 0$). This necessitates modifications to the saddle point method such that the singularity vanishes. For the sake of simplicity, We employ the saddle point method adapted specifically to the hydrogenic 1s state as

$$T_0^{\mathrm{SP}}(\mathbf{p}) = -2^{-1/2} (2I_p)^{5/4} \sum_{t_s} \frac{\exp\left[iS(\mathbf{p}, t_s)\right]}{S''(\mathbf{p}, t_s)}, \tag{5.9}$$

where the sum runs over all relevant saddle points t_s that are part of the steepest-descent integration path. The detailed derivation are provided in the appendix.

5.4.1 *Electric Field Dynamics and Corresponding Saddle Points in Bessel Pulses*

The electric field components of a two-cycle Bessel pulse along the x, y, and z directions are presented in Figure 5.16, analyzed for various values of m_γ and θ_k. Critical interaction times $\tau = \mathrm{Re}\, t_s$, marked by orange indicators, correspond to moments when the electron must couple with the field to achieve a detector energy of $\epsilon_p = 5\omega$. A striking feature emerges for $m_\gamma = 2$, where the z-component exhibits substantial enhancement with increasing opening angle, signaling the activation of additional quantum pathways. These quantum paths, defined as stationary-phase trajectories contributing to the ionization amplitude, originate from new saddle points introduced by the z-component's influence. This phenomenon demonstrates how higher angular momentum states modify ionization dynamics through field-structure interactions. In contrast, the $m_\gamma = 1$ case shows no z-component contribution, making the opening

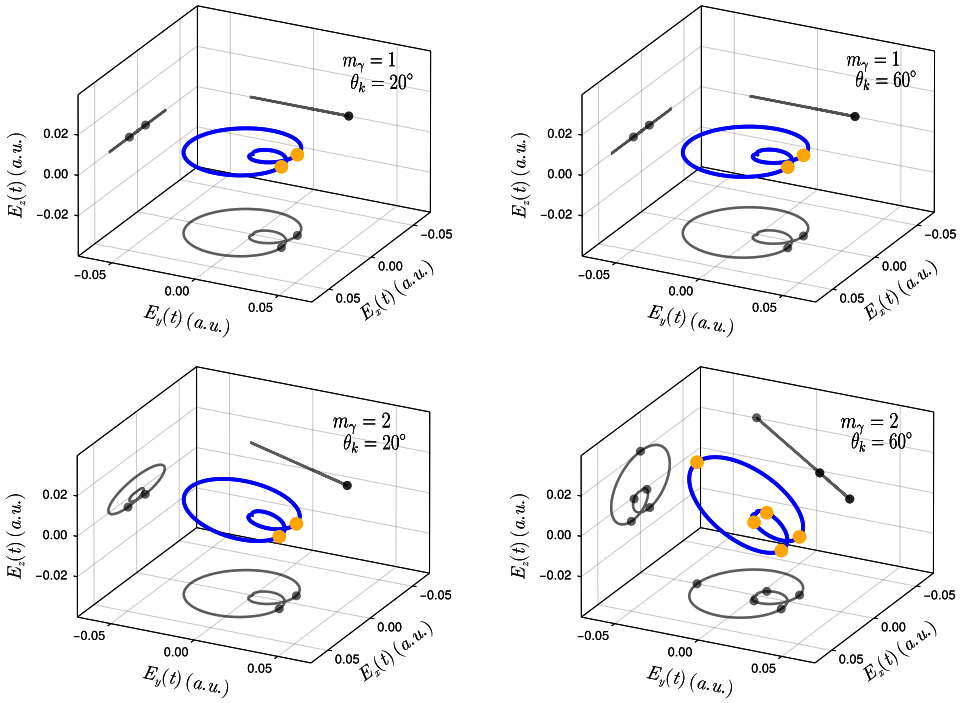

Figure 5.16: Electric field of a two-cycle Bessel pulse with saddle-point solutions (orange circles) for a laser intensity of $5{\times}10^{13}$ W/cm^2 and $\epsilon_p = 5\omega$. The TAM values $m_\gamma = 1, 2$ are shown from top to bottom, with a opening angle of $\theta_k = 20°$ and $60°$ left to right respectively. Grey plots represent the projections of the electric field on the xy, xz, and yz planes.

angle irrelevant to ionization dynamics and highlighting the crucial role of system symmetry in determining available quantum paths.

Figure 5.17 presents the Bessel pulse's electric field alongside corresponding saddle points (gray circles) across the energy range $0 \leq \epsilon_p \leq 20\omega$, comparing $m_\gamma = 1$ and $m_\gamma = 2$ configurations at opening angles of $20°$ and $60°$. The saddle points were computed using Julia's `NLsolve` package [122–124] with Newton-Raphson refinement. For $m_\gamma = 1$, the inward migration of saddle points with increasing photon energy reflects reduced electron-field interaction times, characteristic of direct ionization processes in lower angular momentum states. Conversely, $m_\gamma = 2$ displays outward-moving saddle points, indicating extended interaction durations necessary for effective ionization. The opening angle θ_k plays a particularly significant role for $m_\gamma = 2$, where larger values activate new quantum paths through z-component contributions. While these additional saddle points initially provide minor contributions to the temporal integral at small θ_k, their influence becomes dominant at larger opening angles. This transition occurs as saddle points beyond certain imaginary-time thresholds become negligible, revealing how pulse geometry and angular momentum jointly control ionization dynamics through saddle-point redistribution.

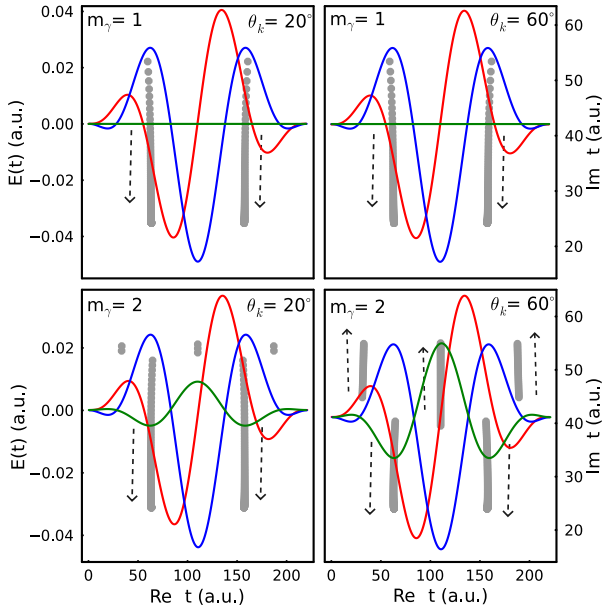

Figure 5.17: Electric field components of a two-cycle Bessel pulse with saddle-point solutions (gray circles) for a laser intensity of $5\times10^{13}\,\mathrm{W/cm^2}$ and ϵ_p ranging from $0 \leq \epsilon_p \leq 20\omega$. The colored lines represent the electric field components: red for E_x, blue for E_y, and green for E_z. The TAM values $m_\gamma = 1, 2$ are shown from left to right, with a fixed opening angle $\theta_k = 20°$ and 60°. θ_p and φ_p are kept constant at 90° and 0° respectively. Black dashed arrow-headed lines indicate the direction of the saddle point with increasing kinetic energy of the photoelectrons.

5.4.2 *Role of Orbital Angular Momentum in Ionization Dynamics*

The angular-resolved photoelectron momentum distribution (PMD) for a two-cycle Bessel pulse is shown in Figure 5.18, comparing m_γ values of 1, 2, and 3 under consistent laser parameters: wavelength $\lambda = 800\,\mathrm{nm}$, polar angle $\theta_p = 90°$, azimuthal angle $\varphi_p = 0°$, and intensity $I_\perp = 5\times10^{13}\,\mathrm{W/cm^2}$. Fringe shifting observed at larger opening angles, particularly for $m_\gamma \geq 2$, stems from enhanced coupling with the longitudinal field component along the z-axis. This z-component interaction elongates electron trajectories in momentum space, especially for higher total angular momentum projections. While Figure 5.16 demonstrates increasing z-component contributions with θ_k, similar fringe shifts occur for $m_\gamma = 1$ where no z-component exists. This dual behavior arises from the ponderomotive energy

$$U_p = \frac{3}{32}A_0^2\left(2\alpha_{-1}^2 + 2\alpha_{+1}^2 + \alpha_0^2\right),$$

where $\alpha_{\pm1}$ represent x- and y-field components and α_0 corresponds to the z-component. Since all terms depend on θ_k, the fringe shifts reflect combined contributions from both transverse and longitudinal field components.

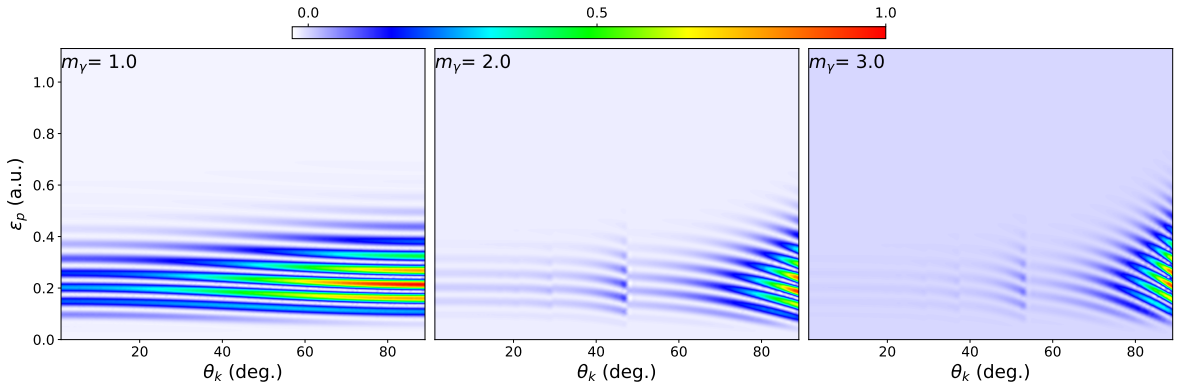

Figure 5.18: Photoelectron momentum distribution (PMD) resolved by opening angle for different m_γ values. The parameters are: wavelength $\lambda = 800\,\text{nm}$, polar angle $\theta_p = 90°$, azimuthal angle $\varphi_p = 0°$, helicity $\Lambda = +1$, and peak intensity $I_\perp = 5 \times 10^{13}\,\text{W/cm}^2$. The colorbar represents the normalized ionization probability.

The transverse momentum distributions in the p_x-p_y plane (Figure 5.19) reveal progressive confinement effects with increasing m_γ at fixed $\theta_k = 20°$. The $m_\gamma = 1$ distribution shows characteristic broad fringes from purely transverse field interactions, while higher m_γ values exhibit narrowing distributions due to growing longitudinal component influence. This confinement manifests as momentum-space "flipping" along p_y for $m_\gamma \geq 2$, demonstrating how angular momentum projection shapes the final electron momentum distribution.

Longitudinal effects become particularly evident in Figure 5.21, which examines the p_z-p_y plane for $m_\gamma = 2$ at $\theta_k = 5°$, 20°, and 40°. The transition from transverse-dominated dynamics at $\theta_k = 5°$ to longitudinal-driven behavior at $\theta_k = 40°$ occurs while maintaining symmetric double-peak structures. This evolution identifies critical θ_k thresholds where longitudinal field components begin dominating the ionization dynamics, providing clear evidence of geometry-dependent control over electron trajectories.

Collectively, these results demonstrate how Bessel pulse parameters govern strong-field ionization through three primary mechanisms: quantum path activation via longitudinal fields, saddle-point redistribution, and momentum-space confinement effects. The intricate relationship between pulse geometry and angular momentum components offers powerful tools for manipulating ionization processes through precise field parameter control.

The expansion of quantum pathways with increasing opening angle θ_k reveals fundamental aspects of Bessel pulse ionization dynamics. For higher m_γ values, the growing longitudinal (z) component of the Bessel pulse activates additional quantum paths through new saddle points, which manifest primarily in the lower and central energy

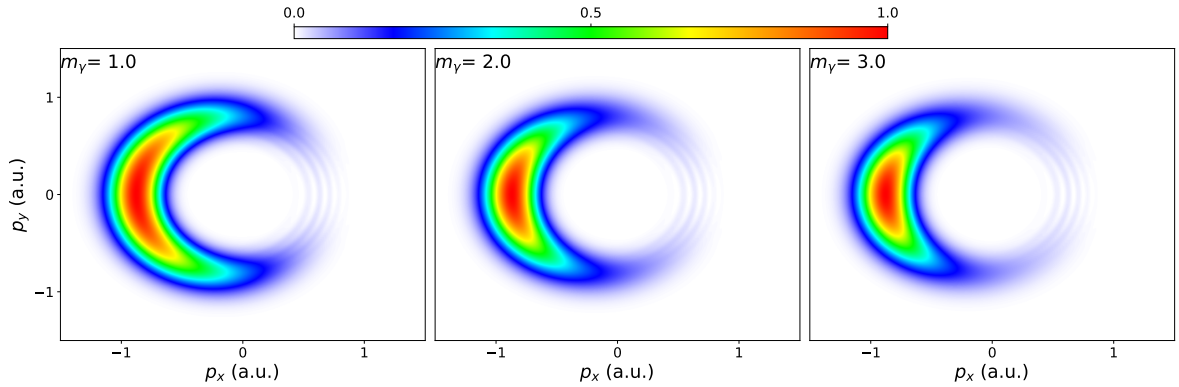

Figure 5.19: Photoelectron momentum distribution in the laser polarization $p_x - p_y$ plane for a laser intensity of 5×10^{13} W/cm^2. The laser parameters are identical to those in Fig. 5.18, with an opening angle of $\theta_k = 20°$. The colorbar represents the normalized ionization probability.

regions of the photoelectron momentum distribution (PMD). This activation mechanism explains the enhanced ionization probability observed at wider opening angles. The $m_\gamma = 1$ case presents qualitatively different behavior - with no z-component contribution, the ionization probability increases linearly, governed solely by transverse (x and y) field components. In contrast, higher m_γ values exhibit nonlinear probability enhancement from two concurrent effects: strengthening z-component contributions and the emergence of new quantum paths. These longitudinal-field-associated saddle points particularly amplify ionization in lower PMD energy regions, creating the observed accelerated ionization rate scaling for $m_\gamma \geq 2$.

Figure 5.19 presents transverse momentum distributions in the p_x-p_y plane for total angular momentum (TAM) values $m_\gamma = 1, 2, 3$ under a two-cycle Bessel pulse ($\theta_k = 20°$). The distributions, recorded in the polarization plane perpendicular to the propagation (z) axis, demonstrate how increasing TAM modifies electron dynamics. While the z-component doesn't directly affect transverse momentum, it significantly influences the overall ionization process. The characteristic semicircular patterns, consistent with short-pulse strong-field ionization, undergo progressive narrowing along both p_x and p_y directions as m_γ increases from 1 to 3.

This transverse confinement stems from the z-component's growing influence at higher m_γ, which redirects ionization dynamics along the propagation axis. The $m_\gamma = 1$ distribution (left panel) shows maximal transverse spread with distinct interference fringes, reflecting pure transverse-field driving. For $m_\gamma = 2$ (middle panel) and $m_\gamma = 3$ (right panel), the distributions exhibit pronounced confinement, appearing as compressed versions of the $m_\gamma = 1$ case with an apparent p_y-axis flip. This transformation directly correlates with the strengthening z-component, which increasingly dominates the ionization dynamics for higher angular momentum states. The progres-

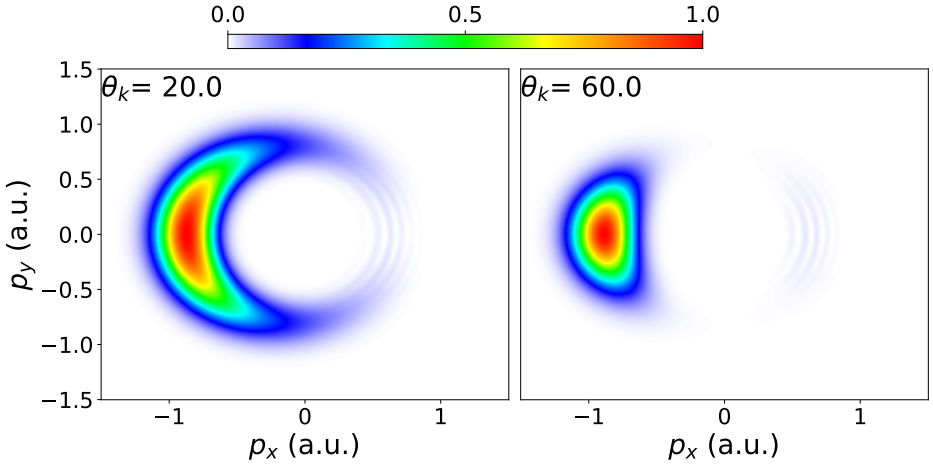

Figure 5.20: Photoelectron momentum distribution in the laser polarization $p_x - p_y$ plane for a laser intensity of 5×10^{13} W/cm^2. The laser parameters are identical to those in Fig. 5.18, with $m_\gamma = 2$ and an opening angle of $\theta_k = 20°$ and $\theta_k = 60°$. The colorbar represents the normalized ionization probability.

sive narrowing demonstrates how TAM projection controls the spatial distribution of ionized electrons through the competition between transverse and longitudinal field components.

The transition from transverse-dominated to longitudinally-influenced dynamics occurs through three identifiable stages: (1) For $m_\gamma = 1$, purely transverse fields create broad, symmetric distributions; (2) At $m_\gamma = 2$, emerging z-component effects initiate transverse compression; (3) The $m_\gamma = 3$ case shows fully developed longitudinal influence with maximally confined distributions. This evolution provides clear experimental signatures of how angular momentum projection shapes strong-field ionization outcomes through field-component interplay.

The momentum distribution for $m_\gamma = 3$ reveals particularly strong confinement along both p_x and p_y axes, demonstrating the dominant role of the longitudinal (z) field component at higher angular momentum states. This pronounced narrowing in the transverse plane directly results from the electron's motion being increasingly redirected along the propagation axis, with the z-component's influence growing substantially with m_γ. The complete ionization dynamics thus transitions from transverse-field dominance at lower m_γ to z-component control at higher values.

Figure 5.20 demonstrates the angular dependence of electron dynamics, where increasing θ_k from 20° to 60° transforms the PMD from a broad, fringe-rich distribution to a significantly narrower profile. This compression reflects the growing influence of the longitudinal field component, which reshapes the effective potential landscape experienced by the electron. The fringe compression toward the center indicates stronger transverse confinement at larger angles, as the three-dimensional momentum distri-

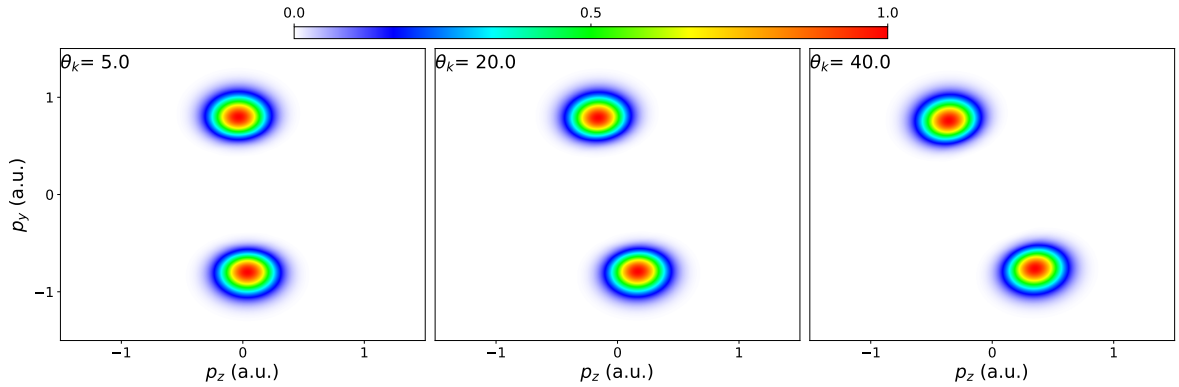

Figure 5.21: Photoelectron momentum distribution in the laser propagation $p_z - p_y$ plane for a laser intensity of 5×10^{13} W/cm^2. The laser parameters are identical to those in Fig. 5.18, with $m_\gamma = 2$ and an opening angle of $\theta_k = 5°$, 20°, and 40°. The colorbar represents the normalized ionization probability.

bution (peaked outside the p_x-p_y plane) projects into increasingly constrained transverse coordinates.

The longitudinal field's role becomes particularly evident in Figure 5.21, which examines the p_z-p_y plane for $m_\gamma = 2$ across three opening angles. At $\theta_k = 5°$, the symmetric double-peak structure centered at $p_z = 0$ confirms transverse-field dominance, with minimal longitudinal influence. The distribution maintains cylindrical symmetry about the propagation axis, characteristic of conventional strong-field ionization patterns.

Intermediate angles ($\theta_k = 20°$) reveal the onset of longitudinal effects through measurable p_z shifts, while remarkably preserving the transverse double-peak structure. This hybrid behavior demonstrates the competing influences of transverse and longitudinal field components during the ionization process. At $\theta_k = 40°$, the dramatic p_z separation confirms longitudinal-field dominance, though the persistent p_y symmetry indicates that transverse components still govern in-plane dynamics.

The complete angular progression reveals a clear transition threshold where longitudinal effects surpass transverse contributions. Below $\theta_k \approx 15°$, the dynamics remain transverse-dominated, while above $\theta_k \approx 30°$, the longitudinal component controls the overall electron trajectory. This transition manifests through three key signatures: (1) growing p_z momentum components, (2) transverse momentum narrowing, and (3) preserved in-plane symmetry - together providing comprehensive evidence of field-geometry-controlled ionization dynamics.

6

CONCLUSION AND OUTLOOK

6.1 SUMMARY OF KEY FINDINGS

This doctoral dissertation has presented a comprehensive theoretical investigation of strong-field ionization, with particular emphasis on above-threshold ionization phenomena and their momentum-resolved characteristics. Our work has systematically explored both fundamental aspects and advanced applications of SFI through a combination of analytical derivations and numerical simulations.

The theoretical framework developed in Chapter 2 and 3 established a rigorous foundation for understanding light-matter interactions in intense fields. We examined various electromagnetic field configurations ranging from conventional plane waves to ultrashort few-cycle pulses and twisted light beams carrying orbital angular momentum. The detailed analysis included both temporal and spectral characteristics of these pulses, along with a complete derivation of the strong field approximation from first principles. Special attention was given to gauge considerations, validity conditions, and the increasingly important nondipole effects that emerge in high-intensity, short-pulse regimes.

Chapter 4 presented the computational methodology that enabled our numerical investigations. The sophisticated implementation of saddle point approximation techniques, including their connection to stationary phase methods and the physical interpretation of complex-time solutions, formed the core of our approach. We developed robust numerical algorithms for root-finding in complex domains and momentum space discretization, complemented by strategies for computational efficiency in large-scale parameter space exploration.

The results presented in Chapter 5 revealed several significant insights into strong-field ionization dynamics. For few-cycle pulses, we demonstrated how pulse duration, carrier-envelope phase, and polarization state collectively influence ionization yields and electron emission patterns. Our analysis of quantum interference phenomena clarified how ATI peak structures arise from multipath interference governed by Volkov phases, with spectral features encoding valuable temporal information. The

investigation of nondipole regimes showed substantial magnetic field contributions at high intensities, with characteristic wavelength-dependent effects. Perhaps most innovatively, our work with twisted light beams revealed how OAM modifies angular momentum distributions and how phase singularities create distinct saddle point configurations.

6.2 FUTURE DIRECTIONS

The findings presented in this thesis open several promising avenues for further investigation. One natural extension would be to explore more complex laser field configurations beyond the current setup. The observed modifications to the potential barrier and vector potential dynamics, as illustrated in Fig. 6.1, suggest that introducing additional field components could yield richer control over electron dynamics. Specifically, incorporating a second field component with different polarization or frequency could enable finer manipulation of the ionization process and photoelectron emission patterns.

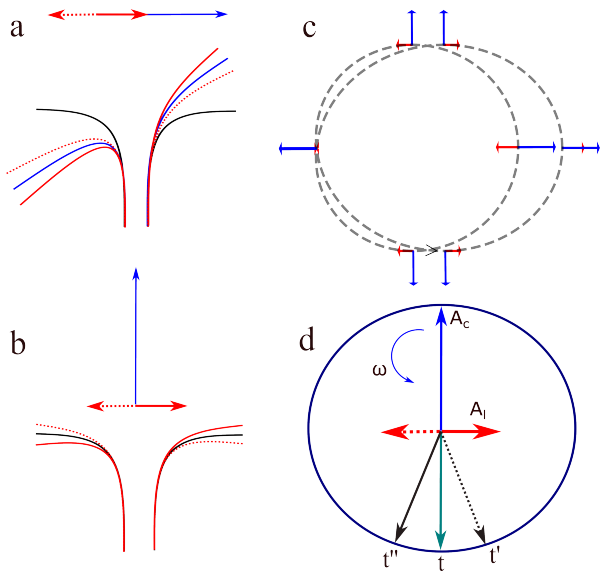

Figure 6.1: Schematic of a two-color laser field (strong CP + weak LP) showing: (a) Potential barrier modification by LP field (red) vs CP alone (blue); (b) Asymmetric potential from perpendicular LP component; (c) Polarization plane with rotating CP (blue arrows) and oscillating LP (red arrows); (d) Vector potentials $\mathbf{A}_C$ (blue), $\mathbf{A}_L$ (red), and the black lines show different ionization times t', t'' corresponding to total vector potential.

The phase-dependent effects demonstrated in Figs. 6.3 and 6.4 highlight the importance of temporal control in strong-field processes. Future studies could investigate these phenomena using few-cycle laser pulses, where the carrier-envelope phase becomes a critical parameter. This approach would allow for attosecond-scale control

of the ionization process, potentially leading to new methods for steering electron trajectories with unprecedented precision.

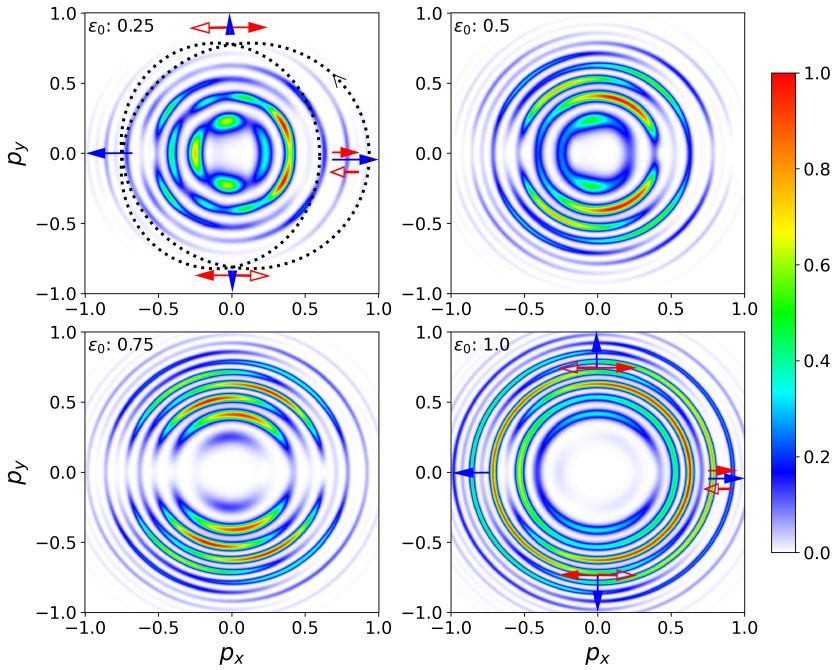

Figure 6.2: Photoelectron momentum distributions in the polarization plane (p_x, p_y) for a two-color field comprising a strong circularly polarized component and a weak linearly polarized component, shown for different ellipticities $\epsilon_0 = 0.25$, 0.5, 0.75, and 1.0. The color scale represents the normalized ionization probability, with red indicating the highest yield. As ϵ_0 increases from top-left to bottom-right, the field evolves from elliptical to circular polarization. The panels demonstrate how the angular distribution and interference structures become more symmetric and circular for higher ellipticity. Arrows denote the polarization directions of the field components, while dotted circles in the top-left panel guide the eye to interference ring structures. The rotation direction of the circular component is indicated by the curved arrow.

Further examination of ellipticity-dependent effects, as shown in Fig. 6.2, could provide deeper insights into the transition between linear and circular polarization regimes. Systematic studies varying the ellipticity across its full range while maintaining other parameters constant might reveal previously unidentified interference phenomena or symmetry-breaking effects. Such investigations could prove particularly valuable for understanding the fundamental limits of polarization control in strong-field ionization.

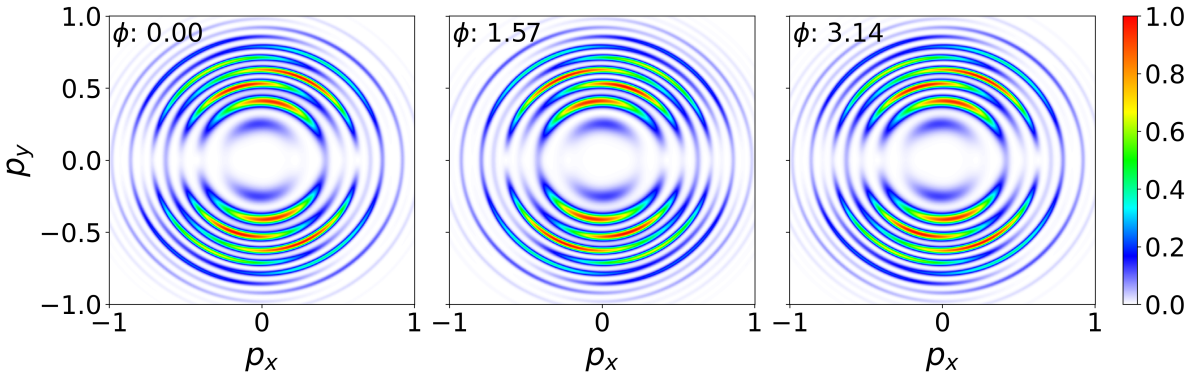

Figure 6.3: Photoelectron momentum distributions in the polarization plane (p_x, p_y) for a two-color laser field composed of a strong circularly polarized field and a weak linearly polarized field, with fixed ellipticity $\epsilon_0 = 0.75$. The panels correspond to different relative phases $\phi = 0$, $\phi = \pi/2$, and $\phi = \pi$ between the two field components. The color scale indicates the normalized ionization probability. Changing the phase modifies the interference pattern and symmetry in the momentum distribution, revealing how phase control can steer ionization pathways and influence electron emission directionality.

The trajectory analysis presented in Fig. 6.4 suggests opportunities for developing more sophisticated theoretical models. Future work could focus on classifying trajectory contributions to specific features in the momentum spectrum, potentially leading to a more comprehensive understanding of the relationship between laser parameters and recollision dynamics. This could involve developing new analytical tools or numerical methods to disentangle the complex interplay of various ionization pathways.

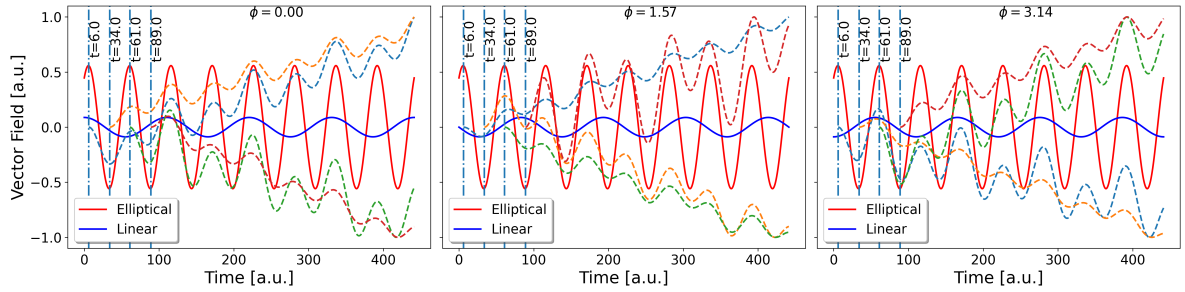

Figure 6.4: Time evolution of the vector potential components and corresponding electron trajectories for a two-color laser field composed of an elliptical (red, strong) and a linear (blue, weak) field, for three different relative phases: $\phi = 0$, $\phi = \pi/2$, and $\phi = \pi$. The panels display the field components (solid and dashed lines) and the calculated electron trajectories (dashed lines in green, orange, cyan and red) launched at specific ionization times (vertical dashed lines) corresponding to laser phases $\omega t = 60°, 120°$, and $180°$. The phase-dependent modulation of the total vector field affects the direction and curvature of the trajectories, highlighting the role of relative phase in steering photoelectrons in strong-field ionization.

Applications of these findings to material-specific systems represent another promising direction. The asymmetric potential barriers shown in Fig. 6.1 indicate that sim-

ilar approaches could be adapted for studying orientation-dependent ionization in aligned molecular systems or crystalline materials. Such investigations could bridge the gap between fundamental strong-field physics and practical applications in ultrafast spectroscopy or materials characterization.

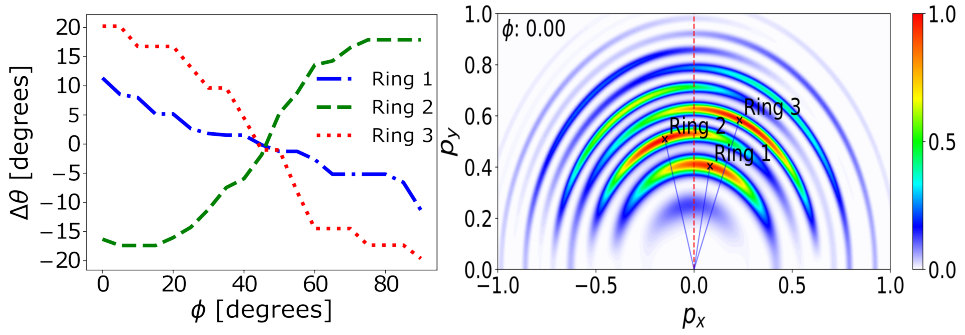

Figure 6.5: Phase-dependent angular shift of ATI peaks in the photoelectron momentum distribution. **Left:** Angular deviation $\Delta\theta$ of the first three ATI rings as a function of the relative phase ϕ (in degrees) between the circularly and linearly polarized components of the two-color laser field. The shifts are extracted from the maxima of the corresponding rings in the distribution and show opposite trends for different rings due to interference effects. **Right:** Polarization-plane momentum distribution at $\phi = 0$, highlighting the angular locations of the first three ATI rings (labeled Ring 1, Ring 2, and Ring 3). The red dashed line marks the polarization axis of the linear component. The black solid lines denote the measured angular positions used in the left panel. The observed shift in ring positions with changing ϕ provides insight into the nonlinear interference and trajectory reshaping in strong-field ionization.

Finally, extending these concepts to mid-infrared driving fields may enable attoclock measurements with improved energy resolution, as the larger cycle-averaged quiver amplitude would amplify the phase-dependent momentum shifts shown in Fig. 6.5. Such developments could bridge the gap between attosecond angular streaking and laser-induced electron diffraction, offering a unified framework for probing matter with combined attosecond temporal and angstrom spatial resolution.

Part I

APPENDIX

A

DERIVATIONS IN DIPOLE APPROXIMATION

This appendix presents the detailed mathematical derivations of two fundamental components in strong-field quantum dynamics: the Volkov phase and the transition amplitude, both treated within the dipole approximation. The dipole approximation, which neglects the spatial dependence of the laser field ($\mathbf{A}(\mathbf{r}, t) \approx \mathbf{A}(t)$), is valid when the electron's quiver amplitude is small compared to the laser wavelength.

A.1 PLANE WAVE PULSE

It is convenient to represent the electromagnetic field, particularly when working with time-varying fields or in situations where the electric and magnetic fields are orthogonal, in terms of a vector potential. For a sine-squared pulse envelope, the vector potential in the dipole approximation is given by:

$$\begin{aligned}\mathbf{A}(t) = \frac{A_0}{\sqrt{1+\epsilon^2}} f(t) \Big(& \cos(\omega t + \phi_{\text{CEP}})\mathbf{e}_x \\ & + \epsilon\Lambda \sin(\omega t + \phi_{\text{CEP}})\mathbf{e}_y \Big),\end{aligned} \tag{A.1}$$

where ϵ represents the ellipticity, Λ is the helicity ($\Lambda = \pm 1$), ω is the carrier frequency, ϕ_{CEP} is the carrier-envelope phase (CEP), and A_0 is the peak amplitude.

The envelope function $f(t)$, which describes the temporal shape of the pulse, is given by:

$$f(t) = \begin{cases} \sin^2\left(\frac{\omega t}{2n_p}\right), & 0 \le t \le \tau_p \\ 0, & \text{otherwise,} \end{cases} \tag{A.2}$$

where n_p is the number of optical cycles within the pulse duration $\tau_p = n_p T$ ($T = 2\pi/\omega$ being the optical period).

By expanding the trigonometric products and substituting (A.2) into (A.1), the vector potential can be expressed as:

$$\mathbf{A}(t) = \frac{A_0}{\sqrt{1+\epsilon^2}} \begin{bmatrix} -\frac{1}{4}\begin{pmatrix} \cos\left(\omega t\left(1-\frac{1}{n_p}\right)+\phi_{\text{CEP}}\right) \\ +\cos\left(\omega t\left(1+\frac{1}{n_p}\right)+\phi_{\text{CEP}}\right) \\ -2\cos\left(\omega t+\phi_{\text{CEP}}\right) \end{pmatrix}\mathbf{e}_x \\ -\frac{\epsilon\Lambda}{4}\begin{pmatrix} \sin\left(\omega t\left(1-\frac{1}{n_p}\right)+\phi_{\text{CEP}}\right) \\ +\sin\left(\omega t\left(1+\frac{1}{n_p}\right)+\phi_{\text{CEP}}\right) \\ -2\sin\left(\omega t+\phi_{\text{CEP}}\right) \end{pmatrix}\mathbf{e}_y \end{bmatrix}, \tag{A.3}$$

In a more compact form, the vector potential can be written as a sum over three frequency components:

$$\mathbf{A}(t) = \sum_{j=0}^{2} \frac{\mathcal{A}_j}{\sqrt{1+\epsilon^2}} \left[\cos(\omega_j t+\phi_{\text{CEP}})\mathbf{e}_x + \epsilon\Lambda\sin(\omega_j t+\phi_{\text{CEP}})\mathbf{e}_y\right], \tag{A.4}$$

where we have introduced the following notation for the frequencies and amplitudes:

$$\omega_j = \left(1-\frac{1}{n_p},\quad 1,\quad 1+\frac{1}{n_p}\right)\omega, \quad \text{and} \quad \mathcal{A}_j = \left(-\frac{1}{4},\quad \frac{1}{2},\quad -\frac{1}{4}\right)A_0. \tag{A.5}$$

A.2 DIPOLE VOLKOV PHASE FOR ELLIPTICALLY POLARIZED PLANE WAVE PULSE

The Volkov phase in the dipole approximation describes the quantum mechanical phase acquired by a free electron in an electromagnetic field. It is given by the time integral of the kinetic energy:

$$S(\mathbf{p},t) = \frac{1}{2}\int^{t} (\mathbf{p}+\mathbf{A}(\tau))^2\, d\tau. \tag{A.6}$$

where $\mathbf{p}$ is the canonical momentum and $\mathbf{A}(\tau)$ is the vector potential of the laser field. The integral in Eq. (A.6) can be decomposed into three distinct terms:

$$\begin{aligned} I &= \frac{1}{2}\int^t \mathbf{p}^2\, d\tau, \\ II &= \int^t \mathbf{p}\cdot\mathbf{A}(\tau)\, d\tau, \\ III &= \frac{1}{2}\int^t \mathbf{A}(\tau)\cdot\mathbf{A}(\tau)\, d\tau. \end{aligned} \tag{A.7}$$

The first term represents the free-electron kinetic energy contribution

$$I = \frac{\mathbf{p}^2}{2}t, \tag{A.8}$$

which is straightforward to evaluate. Using the vector potential from Eq. (A.4), we evaluate the second term

$$\begin{aligned} II &= \sum_{j=0}^{2} \frac{\mathcal{A}_j}{\sqrt{1+\epsilon^2}} \int^t \left[\cos(\omega_j\tau+\phi_{\text{CEP}})\mathbf{p}\cdot\mathbf{e}_x + \epsilon\Lambda\sin(\omega_j\tau+\phi_{\text{CEP}})\mathbf{p}\cdot\mathbf{e}_y\right] d\tau \\ &= \sum_{j=0}^{2} \frac{\mathcal{A}_j}{\sqrt{1+\epsilon^2}} \left[p_x\int^t \cos(\omega_j\tau+\phi_{\text{CEP}})\, d\tau + \epsilon\Lambda p_y\int^t \sin(\omega_j\tau+\phi_{\text{CEP}})\, d\tau\right] d\tau \\ &= \sum_{j=0}^{2} \frac{\mathcal{A}_j}{\sqrt{1+\epsilon^2}} \left[\frac{p_x}{\omega_j}\sin(\omega_j\tau+\phi_{\text{CEP}}) - \epsilon\Lambda\frac{p_y}{\omega_j}\cos(\omega_j\tau+\phi_{\text{CEP}})\right]. \end{aligned} \tag{A.9}$$

Now we can derive the third integral

$$III = \frac{1}{2}\int^t \mathbf{A}_i(\tau)\cdot\mathbf{A}_j(\tau)\, d\tau. \tag{A.10}$$

The third term represents the ponderomotive energy and requires more careful analysis. We separate it into two cases

CASE A: DIAGONAL TERMS $(i = j)$

$$
\begin{aligned}
III - A &= \frac{1}{2}\int^t \mathbf{A}_j^2(\tau)\, d\tau. \\
&= \frac{1}{2}\int^t \frac{\mathcal{A}_j^2}{1+\epsilon^2}\int^t [\cos^2(\omega_j\tau + \phi_{\text{CEP}}) + \epsilon^2 \sin^2(\omega_j\tau + \phi_{\text{CEP}})]\, d\tau \\
&= \frac{1}{2}\int^t \frac{\mathcal{A}_j^2}{1+\epsilon^2}\int^t [\frac{1}{2}\left(1 + \cos(2\omega_j\tau + 2\phi_{\text{CEP}})\right) + \frac{\epsilon^2}{2}\left(1 - \cos(2\omega_j\tau + 2\phi_{\text{CEP}})\right)]\, d\tau \\
&= \frac{\mathcal{A}_j^2}{4}\int^t d\tau + \frac{\mathcal{A}_j^2}{4}\frac{1-\epsilon^2}{1+\epsilon^2}\int^t \cos(2\omega_j\tau + 2\phi_{\text{CEP}})\, d\tau \\
&= \frac{\mathcal{A}_j^2}{4}t + \frac{\mathcal{A}_j^2}{8\omega_j}\frac{1-\epsilon^2}{1+\epsilon^2}\sin(2\omega_j t + 2\phi_{\text{CEP}}),
\end{aligned}
\tag{A.11}
$$

here, we used the identity $\cos^2\theta = \frac{1}{2}(1 + \cos 2\theta)$ and $\sin^2\theta = \frac{1}{2}(1 - \cos 2\theta)$.

CASE B: OFF-DIAGONAL TERMS $(i \neq j)$

$$
\begin{aligned}
III - B = \sum_{i=0}^{2}\sum_{j=0, j\neq i}^{2} \frac{\mathcal{A}_i\mathcal{A}_j}{2(1+\epsilon^2)}\int^t [&\cos(\omega_i\tau + \phi_{\text{CEP}})\cos(\omega_j\tau + \phi_{\text{CEP}}) \\
&+ \epsilon^2 \sin(\omega_i\tau + \phi_{\text{CEP}})\sin(\omega_j\tau + \phi_{\text{CEP}})]\, d\tau.
\end{aligned}
\tag{A.12}
$$

Now to further simplify we can use the following trigonometric identities

$$
\begin{aligned}
\cos(a)\cos(b) &= \frac{1}{2}(cos(a-b) + cos(a+b)) \quad \text{and} \\
\sin(a)\sin(b) &= \frac{1}{2}(cos(a-b) - cos(a+b)).
\end{aligned}
$$

To simplify our integral we will again divide it into two parts $III - B^1$ and $III - B^2$. Starting with the first part

$$
\begin{aligned}
III - B^1 &= \sum_{i=0}^{2}\sum_{j=0, j\neq i}^{2} \frac{\mathcal{A}_i\mathcal{A}_j}{2(1+\epsilon^2)}\int^t \frac{1}{2}[\cos((\omega_i - \omega_j)\tau) + \cos((\omega_i + \omega_j)\tau + 2\phi_{\text{CEP}})]d\tau \\
&= \sum_{i=0}^{2}\sum_{j=0, j\neq i}^{2} \frac{\mathcal{A}_i\mathcal{A}_j}{4(1+\epsilon^2)}\left[\frac{\sin((\omega_i - \omega_j)t)}{\omega_i - \omega_j} + \frac{\sin((\omega_i + \omega_j)t + 2\phi_{\text{CEP}})}{\omega_i + \omega_j}\right]
\end{aligned}
\tag{A.13}
$$

similarly the second part will become

$$\begin{aligned} III - B^2 &= \sum_{i=0}^{2}\sum_{j=0,j\neq i}^{2} \frac{\mathcal{A}_i\mathcal{A}_j}{2(1+\epsilon^2)} \int^t \frac{\epsilon^2}{2}[\cos((\omega_i-\omega_j)\tau) - \cos((\omega_i+\omega_j)\tau + 2\phi_{\text{CEP}})]d\tau \\ &= \sum_{i=0}^{2}\sum_{j=0,j\neq i}^{2} \frac{\mathcal{A}_i\mathcal{A}_j}{4(1+\epsilon^2)}\epsilon^2 \left[\frac{\sin((\omega_i-\omega_j)t)}{\omega_i-\omega_j} - \frac{\sin((\omega_i+\omega_j)t+2\phi_{\text{CEP}})}{\omega_i+\omega_j}\right] \end{aligned} \tag{A.14}$$

Noting that the double sum over $i \neq j$ can be written more efficiently as $2\sum_{i=0}^{1}\sum_{j=i+1}^{2}$, we combine these results

$$\begin{aligned} III - B = &\sum_{i=0}^{1}\sum_{j=i+1}^{2} \frac{\mathcal{A}_i\mathcal{A}_j}{2(\omega_i-\omega_j)} \sin((\omega_i-\omega_j)t) \\ &\frac{1-\epsilon^2}{1+\epsilon^2}\sum_{i=0}^{1}\sum_{j=i+1}^{2} \frac{\mathcal{A}_i\mathcal{A}_j}{2(\omega_i+\omega_j)} \sin((\omega_i+\omega_j)t+2\phi_{\text{CEP}}) \end{aligned} \tag{A.15}$$

Combining all terms, we arrive at the complete expression for the Volkov phase in the dipole approximation

$$\begin{aligned} S(\mathbf{p},t) \;=\; & \frac{1}{2}\mathbf{p}^2 t + \frac{t}{4}\sum_{i=0}^{2}\mathcal{A}_i^2 + \frac{1-\epsilon^2}{1+\epsilon^2}\sum_{i=0}^{2}\frac{\mathcal{A}_i^2}{8\omega_i}\sin(2\omega_i t + 2\phi_{\text{CEP}}) \\ &+ \sum_{i=0}^{1}\sum_{j=i+1}^{2} \frac{\mathcal{A}_i\mathcal{A}_j}{2(\omega_i-\omega_j)} \sin((\omega_i-\omega_j)t) \\ &+ \frac{1-\epsilon^2}{1+\epsilon^2}\sum_{i=0}^{1}\sum_{j=i+1}^{2} \frac{\mathcal{A}_i\mathcal{A}_j}{2(\omega_i+\omega_j)} \sin((\omega_i+\omega_j)t+2\phi_{\text{CEP}}) \\ &+ \frac{p_x}{\sqrt{1+\epsilon^2}}\sum_{i=0}^{2}\frac{\mathcal{A}_i}{\omega_i}\sin(\omega_i t + \phi_{\text{CEP}}) \\ &- \epsilon\Lambda\frac{p_y}{\sqrt{1+\epsilon^2}}\sum_{i=0}^{2}\frac{\mathcal{A}_i}{\omega_i}\cos(\omega_i t + \phi_{\text{CEP}}). \end{aligned} \tag{A.16}$$

This expression captures all essential physics of the electron dynamics in the laser field, including the free electron motion, ponderomotive energy contributions, and field-dressing effects.

A.3 TRANSITION AMPLITUDE IN DIPOLE APPROXIMATION

For a hydrogen-like 1s wave function, the initial bound state can be effectively approximated using a modified ionization potential I_p. This allows us to express the time-dependent wave function as

$$|\Psi_0(t)\rangle = |\Psi_0\rangle e^{iI_p t} = \frac{(2I_p)^{3/2}}{\sqrt{\pi}} e^{-\sqrt{2I_p}r} e^{iI_p t}. \tag{A.17}$$

This expression represents the bound state, where the wave function maintains an exponential decay in space and an oscillatory phase factor in time due to the ionization potential I_p.

Together with Eq. A.6 and Eq. A.17 we can write the direct transition amplitude in velocity gauge as

$$T_0(\mathbf{p}) = -\langle \mathbf{p}|\Psi_0\rangle e^{-i(S(\mathbf{p},t)+I_p t)}\Big|_0^{\tau_p} - i\langle \mathbf{p}|V(\mathbf{r})|\Psi_0\rangle \int_0^{\tau_p} dt\, e^{-i(S(\mathbf{p},t)+I_p t)}. \tag{A.18}$$

The matrix element of the Coulomb potential and the initial wave function in momentum space can be expressed as

$$\langle \mathbf{p}|V(\mathbf{r})|\Psi_0\rangle = -\frac{2^{\frac{3}{2}} I_p^{\frac{5}{4}}}{\pi} \frac{1}{\epsilon_p + I_p}. \tag{A.19}$$

Similarly, the initial wave function in momentum space is given by:

$$\langle \mathbf{p}|\Psi_0\rangle = \frac{(2I_p)^{\frac{5}{4}}}{\pi\sqrt{2}} \frac{1}{\left(\epsilon_p + I_p\right)^2}. \tag{A.20}$$

Now the remaining task is to evaluate the time integral in the second part of equation A.18. Such a integral is not easy to solve because of the phase factor given in

the equation A.16. The exponential $e^{-iS(\mathbf{p},t)}$ can be expanded using the Jacobi-Anger expansion, yielding:

$$
\begin{aligned}
e^{-iS(\mathbf{p},t)} = \exp\left(-i\left(\frac{1}{2}\mathbf{p}^2 t + \frac{t}{4}\sum_{i=0}^{2}\mathcal{A}_i^2\right)\right) \\
\times \prod_{i=0}^{2}\sum_{n_i=-\infty}^{\infty} J_{n_i}\left(\frac{1-\epsilon^2}{1+\epsilon^2}\frac{\mathcal{A}_i^2}{8\omega_i}\right) e^{-in_i(2\omega_i t + 2\phi_{\text{CEP}})} \\
\times \prod_{i=0}^{1}\prod_{j=i+1}^{2}\sum_{m_{ij}=-\infty}^{\infty} J_{m_{ij}}\left(\frac{\mathcal{A}_i\mathcal{A}_j}{2(\omega_i-\omega_j)}\right) e^{-im_{ij}(\omega_i-\omega_j)t} \\
\times \prod_{i=0}^{1}\prod_{j=i+1}^{2}\sum_{k_{ij}=-\infty}^{\infty} J_{k_{ij}}\left(\frac{1-\epsilon^2}{1+\epsilon^2}\frac{\mathcal{A}_i\mathcal{A}_j}{2(\omega_i+\omega_j)}\right) e^{-ik_{ij}((\omega_i+\omega_j)t + 2\phi_{\text{CEP}})} \\
\times \prod_{i=0}^{2}\sum_{\ell_i=-\infty}^{\infty} J_{\ell_i}\left(\frac{p_x\mathcal{A}_i}{\omega_i\sqrt{1+\epsilon^2}}\right) e^{-i\ell_i(\omega_i t + \phi_{\text{CEP}})} \\
\times \prod_{i=0}^{2}\sum_{q_i=-\infty}^{\infty} (-i)^{q_i} J_{q_i}\left(\frac{\epsilon\Lambda p_y\mathcal{A}_i}{\omega_i\sqrt{1+\epsilon^2}}\right) e^{iq_i(\omega_i t + \phi_{\text{CEP}})},
\end{aligned}
\tag{A.21}
$$

where $J_n(\cdot)$ are Bessel functions of the first kind, and the expansion has been applied to each oscillatory term in $S(\mathbf{p},t)$. Now the integral is more straight forward as we got rid of the trigonometric functions in terms of Bessel function which are time independent. The integral of the exponents are now straight forward using the general way that $\int e^{kx}dx = \frac{e^{kx}}{k}$. Thus applying the expansion and general defination of integrals we can derive the final transition amplitude as

$$
\begin{aligned}
T_0^D(\mathbf{p}) = \prod_{i=1}^{15}\Bigg\{(-i)^{n_i\Theta(i-12)}\sum_{n_i=-\infty}^{\infty} J_{n_i}(x_i^D) \quad \left(\frac{\langle\mathbf{p}|V(\mathbf{r})|\Psi_0\rangle}{\epsilon_p + U_p + \Omega_{n_i}^D + I_p} + \langle\mathbf{p}|\Psi_0\rangle\right) \\
\left(1 - e^{i\left[\left(\epsilon_p + U_p + \Omega_{n_i}^D + I_p\right)\tau_p + \Phi_i^D\right]}\right)\Bigg\},
\end{aligned}
\tag{A.22}
$$

where $\Theta(x)$ is the Heaviside step function which ensures that the extra factor i^{n_i} appears only for the last three terms ($i \geq 13$), while it remains absent for the first 12 terms ($i \leq 12$).The D in the superscript represents the Dipole case and the arguments of the Bessel function in the transition amplitude A.22 include terms involving the squared vector potential amplitudes, their respective frequencies, and interaction terms be-

tween different frequency components, adjusted by the ellipticity factor. These terms are explicitly given as

$$\begin{aligned} x^D \;=\; \Bigg(& \frac{1-\epsilon^2}{1+\epsilon^2}\frac{\mathcal{A}_0^2}{8\omega_0}, \frac{1-\epsilon^2}{1+\epsilon^2}\frac{\mathcal{A}_1^2}{8\omega_1}, \frac{1-\epsilon^2}{1+\epsilon^2}\frac{\mathcal{A}_2^2}{8\omega_2}, \frac{\mathcal{A}_0\mathcal{A}_1}{2(\omega_0-\omega_1)}, \frac{\mathcal{A}_0\mathcal{A}_2}{2(\omega_0-\omega_2)}, \frac{\mathcal{A}_1\mathcal{A}_2}{2(\omega_1-\omega_2)}, \\ & \frac{1-\epsilon^2}{1+\epsilon^2}\frac{\mathcal{A}_0\mathcal{A}_1}{2(\omega_0+\omega_1)}, \frac{1-\epsilon^2}{1+\epsilon^2}\frac{\mathcal{A}_0\mathcal{A}_2}{2(\omega_0+\omega_2)}, \frac{1-\epsilon^2}{1+\epsilon^2}\frac{\mathcal{A}_1\mathcal{A}_2}{2(\omega_1+\omega_2)}, \\ & \frac{p_x}{\sqrt{1+\epsilon^2}}\frac{\mathcal{A}_0}{\omega_0}, \frac{p_x}{\sqrt{1+\epsilon^2}}\frac{\mathcal{A}_1}{\omega_1}, \frac{p_x}{\sqrt{1+\epsilon^2}}\frac{\mathcal{A}_2}{\omega_2}, \\ & \epsilon\Lambda\frac{p_y}{\sqrt{1+\epsilon^2}}\frac{\mathcal{A}_0}{\omega_0}, \epsilon\Lambda\frac{p_y}{\sqrt{1+\epsilon^2}}\frac{\mathcal{A}_1}{\omega_1}, \epsilon\Lambda\frac{p_y}{\sqrt{1+\epsilon^2}}\frac{\mathcal{A}_2}{\omega_2}, \Bigg), \end{aligned} \tag{A.23}$$

where the first set of terms represents the contributions from individual frequency components, while the remaining terms describe cross-interactions between them. The modified frequency and phase, essential for describing the transition dynamics, are defined as

$$\begin{aligned} \Omega^D \;=\; & (2n_1\omega_0 + 2n_2\omega_1 + 2n_3\omega_2 + n_4(\omega_0-\omega_1) + n_5(\omega_0-\omega_2) + n_6(\omega_1-\omega_2) \\ & + n_7(\omega_0+\omega_1) + n_8(\omega_0+\omega_2) + n_9(\omega_1+\omega_2) + n_{10}\omega_0 + n_{11}\omega_1 + n_{12}\omega_2 \\ & + n_{13}\omega_0 + n_{14}\omega_1 + n_{15}\omega_2) \end{aligned} \tag{A.24}$$

$$\begin{aligned} \Phi^D \;=\; & \big(2n_1\phi_{\text{cep}} + 2n_2\phi_{\text{cep}} + 2n_3\phi_{\text{cep}} + 2n_7\phi_{\text{cep}} + 2n_8\phi_{\text{cep}} + 2n_9\phi_{\text{cep}} + n_{10}\phi_{\text{cep}} \\ & + n_{11}\phi_{\text{cep}} + n_{12}\phi_{\text{cep}} + n_{13}\phi_{\text{cep}} + n_{14}\phi_{\text{cep}} + n_{15}\phi_{\text{cep}}\big). \end{aligned} \tag{A.25}$$

These expressions account for the summation and combination of different frequency components and their respective phase contributions.

A.4 DIPOLE VOLKOV PHASE FOR A BESSEL PULSE

The Bessel beam carries orbital angular momentum (OAM) and thus has a non-vanishing z-component. The Bessel pulse can be generalized by multiplying the envelope function (as we did before in the plane wave case) to the Bessel beam as shown previously in equation 2.32. The resulting vector potential can be expanded similarly by expanding the trigonometric functions. The remaining task is to evaluate the phase integral, which is identical to our previous calculation in Section A.2. The final solution is given by

$$S(\tilde{\mathbf{p}}, \tau) = \xi t + \sum_{j=1}^{9} \gamma_j \cos\left(\phi_j^{(c)} - \omega_j^{(c)} t\right) + \sum_{l=1}^{13} \sigma_l \sin\left(\phi_l^{(s)} - \omega_l^{(s)} t\right). \tag{A.26}$$

The coefficients are defined as:

$$\xi = \frac{p^2}{2} + \frac{3}{32}A_0^2(2\alpha_{-1}^2 + 2\alpha_{+1}^2 + \alpha_0^2), \tag{A.27}$$

$$\gamma = \frac{A_0}{2\omega}\left(-p_y\alpha_{+1}, p_z\alpha_0, p_y\alpha_{-1}, \frac{n_p p_y\alpha_{+1}}{2(n_p-1)}, -\frac{n_p p_z\alpha_0}{2(n_p-1)}, \right.$$
$$\left. -\frac{n_p p_y\alpha_{-1}}{2(n_p-1)}, \frac{n_p p_y\alpha_{+1}}{2(n_p+1)}, -\frac{n_p p_z\alpha_0}{2(n_p+1)}, -\frac{n_p p_y\alpha_{-1}}{2(n_p+1)}\right), \tag{A.28}$$

$$\sigma = \frac{A_0}{2\omega}\left(-\frac{A_0 n_p}{4}\left(2\alpha_{+1}^2 + 2\alpha_{-1}^2 + \alpha_0^2\right), \frac{A_0 n_p}{32}\left(2\alpha_{+1}^2 + 2\alpha_{-1}^2 + \alpha_0^2\right), \right.$$
$$-p_x\alpha_{+1}, \frac{3A_0}{32}\left(\alpha_0^2 - 4\alpha_{-1}\alpha_{+1}\right), -p_x\alpha_{-1}, \frac{A_0 n_p}{8(2n_p-1)}\left(4\alpha_{-1}\alpha_{+1} - \alpha_0^2\right),$$
$$\frac{n_p p_x\alpha_{+1}}{2(n_p-1)}, \frac{A_0 n_p}{64(n_p-1)}\left(\alpha_0^2 - 4\alpha_{-1}\alpha_{+1}\right), \frac{n_p p_x\alpha_{-1}}{2(n_p-1)}, \frac{A_0 n_p}{64(n_p+1)}\left(\alpha_0^2 - 4\alpha_{-1}\alpha_{+1}\right),$$
$$\left.\frac{n_p p_x\alpha_{+1}}{2(n_p+1)}, \frac{n_p p_x\alpha_{-1}}{2(n_p+1)}, \frac{A_0 n_p}{8(2n_p+1)}\left(4\alpha_{-1}\alpha_{+1} - \alpha_0^2\right)\right). \tag{A.29}$$

The phases and frequencies are defined as:

$$\omega^c = \omega\left(1, 1, 1, \frac{n_p-1}{n_p}, \frac{n_p-1}{n_p}, \frac{n_p-1}{n_p}, \frac{n_p+1}{n_p}, \frac{n_p+1}{n_p}, \frac{n_p+1}{n_p}\right), \tag{A.30}$$

$$\omega^s = \omega\left(-\frac{1}{n_p}, -\frac{2}{n_p}, 1, 2, 1, \frac{2n_p-1}{n_p}, \frac{n_p-1}{n_p}, 2\frac{n_p-1}{n_p}, \frac{n_p-1}{n_p}, \right.$$
$$\left. 2\frac{n_p+1}{n_p}, \frac{n_p+1}{n_p}, \frac{n_p+1}{n_p}, \frac{2n_p+1}{n_p}\right), \tag{A.31}$$

$$\phi^c = \varphi_b\left(m_\gamma - 1, m_\gamma, m_\gamma + 1, m_\gamma - 1, m_\gamma, m_\gamma + 1, m_\gamma - 1, m_\gamma, m_\gamma + 1\right), \tag{A.32}$$

$$\phi^s = \varphi_b\left(0, 0, m_\gamma - 1, 2m_\gamma, m_\gamma + 1, 2m_\gamma, m_\gamma - 1, 2m_\gamma, m_\gamma + 1, 2m_\gamma, m_\gamma - 1, m_\gamma + 1, 2m_\gamma\right). \tag{A.33}$$

The coefficients in the above equations are given by:

$$\alpha_{-1} = \sqrt{\frac{\varkappa}{4\pi}}c_{-1}J_{m_\gamma+1}(\varkappa r), \tag{A.34}$$

$$\alpha_0 = \sqrt{\frac{\varkappa}{2\pi}}c_0 J_{m_\gamma}(\varkappa r), \tag{A.35}$$

$$\alpha_{+1} = \sqrt{\frac{\varkappa}{4\pi}}c_{+1}J_{m_\gamma-1}(\varkappa r), \tag{A.36}$$

$$\beta_{-1} = (m_\gamma - 1)\varphi_r + k_z z, \tag{A.37}$$

$$\beta_0 = m_\gamma\varphi_r + k_z z, \tag{A.38}$$

$$\beta_{+1} = (m_\gamma + 1)\varphi_r + k_z z. \tag{A.39}$$

In the above coefficients, $c_0 = \frac{\Lambda}{\sqrt{2}} \sin\theta_k$ and $c_{\pm 1} = \frac{1}{2}(1 \pm \Lambda \cos\theta_k)$. Here, Λ represents the corresponding helicity, and $\varkappa = k \sin\theta_k$ with $k = \omega/c$ (where c is the speed of light).

For small opening angles θ_k, one may refer to the orbital angular momentum $m_l = m_\gamma - \Lambda$ of the Bessel beam. The longitudinal wave number is given by $k_z = k \cos\theta_k$, and r in Cartesian coordinates is $r = \sqrt{x^2 + y^2}$. The parameter n_p represents the optical cycles of the pulse, and ω is the corresponding frequency.

B

DERIVATIONS IN NONDIPOLE APPROXIMATION

The time evolution of an electron under the influence of an external electromagnetic field is governed by the time-dependent Schrödinger equation (TDSE). When expressed in the velocity gauge formulation, the system's Hamiltonian incorporates minimal coupling between the electron and the field:

$$\hat{H}_{\mathrm{le}} = \frac{1}{2}\left(\mathbf{p} + \mathbf{A}(\mathbf{r},t)\right)^2 = \frac{1}{2}\mathbf{p}^2 + \mathbf{p}\cdot\mathbf{A}(\mathbf{r},t) + \frac{1}{2}\mathbf{A}^2(\mathbf{r},t). \tag{B.1}$$

In this expression, the first-order $\mathbf{A}$ term describes the electron-field coupling, while the second-order term corresponds to photon self-interaction. Note that in our real-space representation, the position operator $\hat{\mathbf{r}}$ simplifies to the coordinate $\mathbf{r}$. The dynamics of an electron interacting with a general vector potential in the velocity gauge are described by the minimal-coupling Hamiltonian:

$$i\partial_t \left|\chi_{\mathbf{p}}^{ND}(t)\right\rangle = \left[\frac{1}{2}\left(\mathbf{p} + \mathbf{A}(\mathbf{r},t)\right)^2\right]\left|\chi_{\mathbf{p}}^{ND}(t)\right\rangle. \tag{B.2}$$

This equation admits approximate analytical solutions that include first-order relativistic corrections, known as nondipole Volkov states

$$\langle\mathbf{r}|\chi_{\mathbf{p}}^{ND}(t)\rangle = \frac{1}{(2\pi)^{3/2}}\, e^{i\mathbf{p}\cdot\mathbf{r}}\, e^{-i\epsilon_p t + i\Gamma(\mathbf{r},t)}, \quad \text{with} \quad \epsilon_p = \frac{\mathbf{p}^2}{2}, \tag{B.3}$$

where the spatially dependent phase $\Gamma(\mathbf{r},t)$ encodes nondipole corrections arising from the full spatial dependence of the vector potential. The complete nondipole Volkov phase is defined as

$$\Gamma(\mathbf{r},t) = \sum_{i=1}^{5} \Gamma_i(\mathbf{r},t), \tag{B.4}$$

$$\Gamma_1(\mathbf{r},t) = \int \mathrm{d}^3\mathbf{k}\, \rho(\mathbf{k}) \sin\left(u(\mathbf{k}) + \theta(\mathbf{k})\right), \tag{B.5}$$

$$\begin{aligned}\Gamma_2(\mathbf{r},t) = \int \mathrm{d}^3\mathbf{k}\, \mathrm{d}^3\mathbf{k}' \Big[&\alpha^+(\mathbf{k},\mathbf{k}') \sin\left(u(\mathbf{k}) + u(\mathbf{k}') + \theta^+(\mathbf{k},\mathbf{k}')\right) \\ &+ \alpha^-(\mathbf{k},\mathbf{k}') \sin\left(u(\mathbf{k}) - u(\mathbf{k}') + \theta^-(\mathbf{k},\mathbf{k}')\right)\Big],\end{aligned} \tag{B.6}$$

$$\begin{aligned}\Gamma_3(\mathbf{r},t) = \sum_{\pm} \frac{1}{2} \int \mathrm{d}^3\mathbf{k}\, \mathrm{d}^3\mathbf{k}'\, \rho(\mathbf{k})\rho(\mathbf{k}') \\ \times \frac{\sin\left(u(\mathbf{k}) \pm u(\mathbf{k}') + \theta(\mathbf{k}) \pm \zeta(\mathbf{k},\mathbf{k}')\right)}{\eta(\mathbf{k}) \pm \eta(\mathbf{k}')},\end{aligned} \tag{B.7}$$

$$\begin{aligned}\Gamma_4(\mathbf{r},t) = \sum_{\pm} \int \mathrm{d}^3\mathbf{k}\, \mathrm{d}^3\mathbf{k}'\, \mathrm{d}^3\mathbf{k}''\, \sigma(\mathbf{k},\mathbf{k}')\alpha^+(\mathbf{k}',\mathbf{k}'') \\ \times \frac{\sin\left(u(\mathbf{k}) \pm u(\mathbf{k}') + u(\mathbf{k}'') + \theta^+(\mathbf{k}',\mathbf{k}'') \pm \xi(\mathbf{k},\mathbf{k}'')\right)}{\eta(\mathbf{k}) \pm \eta(\mathbf{k}') + \eta(\mathbf{k}'')},\end{aligned} \tag{B.8}$$

$$\begin{aligned}\Gamma_5(\mathbf{r},t) = \sum_{\pm} \int \mathrm{d}^3\mathbf{k}\, \mathrm{d}^3\mathbf{k}'\, \mathrm{d}^3\mathbf{k}''\, \sigma(\mathbf{k},\mathbf{k}')\alpha^-(\mathbf{k}',\mathbf{k}'') \\ \times \frac{\sin\left(u(\mathbf{k}) \pm u(\mathbf{k}') - u(\mathbf{k}'') + \theta^-(\mathbf{k}',\mathbf{k}'') \pm \xi(\mathbf{k},\mathbf{k}'')\right)}{\eta(\mathbf{k}) \pm \eta(\mathbf{k}') - \eta(\mathbf{k}'')}.\end{aligned} \tag{B.9}$$

where Eqs. (B.5) and (B.6) are associated with the particle-field and field-field contributions of the nondipole Volkov phase, respectively. Moreover, Eqs. (B.7)–(B.9) are interconnections of the geometric contribution with the respective particle-field and field-field contributions.

The nondipole phase $\Gamma(\mathbf{r},t)$ consists of several key contributions:

$$\mathbf{p}\cdot\mathbf{A}(\mathbf{k},t) = \lambda(\mathbf{k}) \cos(u(\mathbf{k}) + \theta(\mathbf{k})), \tag{B.10a}$$

$$\mathbf{a}(\mathbf{k})\cdot\mathbf{a}(\mathbf{k}')/4 = \Delta^+(\mathbf{k},\mathbf{k}')\, e^{i\theta^+(\mathbf{k},\mathbf{k}')}, \tag{B.10b}$$

$$\mathbf{a}(\mathbf{k})\cdot\mathbf{a}^*(\mathbf{k}')/4 = \Delta^-(\mathbf{k},\mathbf{k}')\, e^{i\theta^-(\mathbf{k},\mathbf{k}')}, \tag{B.10c}$$

$$-\mathbf{k}\cdot\mathbf{A}(\mathbf{k}',t) = \sigma(\mathbf{k},\mathbf{k}') \cos(u(\mathbf{k}') + \xi(\mathbf{k},\mathbf{k}')), \tag{B.10d}$$

$$\eta(\mathbf{k}) = \mathbf{p}\cdot\mathbf{k} - \omega(\mathbf{k}), \tag{B.10e}$$

$$\rho(\mathbf{k}) = \lambda(\mathbf{k})/\eta(\mathbf{k}), \tag{B.10f}$$

$$\alpha^{\pm}(\mathbf{k},\mathbf{k}') = \Delta^{\pm}(\mathbf{k},\mathbf{k}')/\left(\eta(\mathbf{k}) \pm \eta(\mathbf{k}')\right). \tag{B.10g}$$

For a rigorous derivation and comprehensive analysis, we refer to Refs. [141] and [142] (Chapter 4). For the vector potential given in Eq. (A.4), the system of equations

in Eq. (B.10) can be solved for each individual mode j, yielding the following solutions:

$$
\begin{aligned}
\lambda(\mathbf{k}) &= \frac{A_j(\mathbf{k})}{\sqrt{1+\epsilon^2}}\sqrt{\mathbf{p}_x^2+\epsilon^2\mathbf{p}_y^2}\,\delta(\mathbf{k}-\mathbf{k}_0),\\
\theta(\mathbf{k}) &= \phi_{\text{cep}} + \Lambda \arctan(\epsilon\tan\varphi_p),\\
\rho(\mathbf{k}) &= \frac{A_j(\mathbf{k})}{\sqrt{1+\epsilon^2}}\frac{\sqrt{\mathbf{p}_x^2+\epsilon^2\mathbf{p}_y^2}}{\eta_j(\mathbf{k})}\delta(\mathbf{k}-\mathbf{k}_0),\\
\Delta^+(\mathbf{k},\mathbf{k}') &= \frac{A_j(\mathbf{k})A_j(\mathbf{k}')}{4}\frac{1-\epsilon^2}{1+\epsilon^2}\delta(\mathbf{k}-\mathbf{k}_0)\delta(\mathbf{k}'-\mathbf{k}_0),\\
\Delta^-(\mathbf{k},\mathbf{k}') &= \frac{A_j(\mathbf{k})A_j(\mathbf{k}')}{4}\delta(\mathbf{k}-\mathbf{k}_0)\delta(\mathbf{k}'-\mathbf{k}_0),\\
\theta^+(\mathbf{k}) &= 2\phi_{\text{cep}}, \quad \theta^-(\mathbf{k}) = 0,\\
\sigma(\mathbf{k},\mathbf{k}') &= 0, \quad \xi(\mathbf{k},\mathbf{k}') = \phi_{\text{cep}},\\
\alpha^\pm(\mathbf{k},\mathbf{k}') &= \frac{A_j(\mathbf{k})A_j(\mathbf{k}')}{4}\frac{1\mp\epsilon^2}{1+\epsilon^2}\frac{1}{\eta_j(\mathbf{k})\pm\eta_j(\mathbf{k}')}\delta(\mathbf{k}-\mathbf{k}_0)\delta(\mathbf{k}'-\mathbf{k}_0),
\end{aligned}
\tag{B.11}
$$

where $\eta(\mathbf{k}) = \mathbf{p}\cdot\mathbf{k} - \omega_k$ and $\omega_k = kc$.

To compute the phase $\Gamma(\mathbf{r},t)$, we substitute Eq. (B.11) into Eq. (B.4). This leads to the explicit expression

$$
\begin{aligned}
\Gamma(\mathbf{r},t) = &\int \mathrm{d}^3\mathbf{k}\,\frac{A_j(\mathbf{k})}{\sqrt{1+\epsilon^2}}\frac{\sqrt{\mathbf{p}_x^2+\epsilon^2\mathbf{p}_y^2}}{\eta_j(\mathbf{k})}\sin\Big(u_j+\phi_{\text{cep}}+\Lambda\arctan(\epsilon\tan\varphi_p)\Big)\delta(\mathbf{k}-\mathbf{k}_0)\\
&+\int \mathrm{d}^3\mathbf{k}\int \mathrm{d}^3\mathbf{k}'\,\frac{A_j(\mathbf{k})A_j(\mathbf{k}')}{4}\frac{1-\epsilon^2}{1+\epsilon^2}\frac{1}{\eta_j(\mathbf{k})+\eta_j(\mathbf{k}')}\sin(u_j+u_j'+2\phi_{\text{cep}})\\
&\qquad\times\delta(\mathbf{k}-\mathbf{k}_0)\delta(\mathbf{k}'-\mathbf{k}_0)\\
&+\int \mathrm{d}^3\mathbf{k}\int \mathrm{d}^3\mathbf{k}'\,\frac{A_j(\mathbf{k})A_j(\mathbf{k}')}{4}\frac{1}{\eta_j(\mathbf{k})-\eta_j(\mathbf{k}')}\sin(u_j+u_j')\\
&\qquad\times\delta(\mathbf{k}-\mathbf{k}_0)\delta(\mathbf{k}'-\mathbf{k}_0).
\end{aligned}
\tag{B.12}
$$

The delta functions can be used to simplify these integrals, leading to Eq. (3.39). Note that the third integral vanishes because the wavevectors $\mathbf{k}$ are parallel to the laser propagation direction (z-axis), making $\sigma(\mathbf{k},\mathbf{k}') = 0$. In the above expression, one should note that we combined the terms depending on p_x and p_y, as in the equation 3.39, which give the factor $\arctan(\epsilon\tan\varphi_p)$ where $\varphi_p = \frac{p_y}{p_x}$.

C

MODIFIED SADDLE POINT METHOD FOR IONIZATION AMPLITUDES

The saddle-point method provides a powerful analytical tool for estimating strong-field ionization amplitudes in the high-intensity regime. However, as demonstrated by Milošević et al. [86], its applicability becomes questionable in the case of low-intensity fields and long-range binding potentials such as the Coulomb potential. The key limitation arises from the divergence of the matrix element $\mathbf{r} \cdot \mathbf{E}(t_s)$ at the saddle points t_s, signaling a breakdown of the conventional saddle-point approximation.

In this appendix, we present a systematic derivation of the modified saddle-point approach, with particular emphasis on few-cycle laser pulses. Our treatment follows the formalism developed in [86].

The matrix element for direct ionization in length gauge can be transformed through integration by parts. The derivation begins with the essential operator identity

$$[\mathbf{r} \cdot \mathbf{E}(t) + i\partial_t] \exp\{-i[\mathbf{p} + \mathbf{A}(t)] \cdot \mathbf{r}\} = 0 \tag{C.1}$$

This identity leads to the exact expression for the transition amplitude

$$T_0(\mathbf{p}) = i \int_0^{T_p} \mathrm{d}t\, \tilde{\psi}_0(\mathbf{p} + \mathbf{A}(t)) \frac{\mathrm{d}S(t)}{\mathrm{d}t} e^{iS(t)} - \tilde{\psi}_0(\mathbf{p} + \mathbf{A}(0)) \left[e^{iS(T_p)} - e^{iS(0)} \right] \tag{C.2}$$

where the classical action $S(t) \equiv S_{I_p,\mathbf{p}}(t)$ represents the time-integrated dynamical phase:

$$S(t) = \int_t^{T_p} \mathrm{d}t' \left[\frac{1}{2} (\mathbf{p} + \mathbf{A}(t'))^2 + I_p \right] \tag{C.3}$$

The Fourier-transformed ground state wavefunction appears as:

$$\tilde{\psi}_0(\mathbf{k}) = (2\pi)^{-3/2} \int \mathrm{d}^3\mathbf{r}\, e^{i\mathbf{k}\cdot\mathbf{r}} \psi_0(\mathbf{r}) \tag{C.4}$$

The transition amplitude consists of two distinct physical contributions. The first term involves integration over the entire pulse duration, representing the volumetric ion-

ization probability. The second term constitutes boundary contributions evaluated at the temporal endpoints of the laser interaction. For sufficiently long pulses where $\mathbf{A}(0) = \mathbf{A}(T_p) = 0$, these boundary terms become negligible in most physical scenarios.

The volumetric term contains the factor $\mathrm{d}S(t)/\mathrm{d}t$ which vanishes at saddle points t_s defined by:

$$\left.\frac{\mathrm{d}S(t)}{\mathrm{d}t}\right|_{t=t_s} = 0 \tag{C.5}$$

This suggests potential singular behavior in the integrand. However, the Fourier transform $\tilde{\psi}_0(\mathbf{p} + \mathbf{A}(t))$ provides compensating factors that regularize the expression.

For a coulomb potential with binding energy $I_p = \kappa^2/2$, the ground-state wavefunction in momentum space take particular forms

$$\tilde{\psi}_0(\mathbf{p}) = \frac{2^{3/2}\kappa^{5/2}}{\pi(\kappa^2 + \mathbf{p}^2)^2} = \frac{\kappa^{5/2}}{\sqrt{2\pi}\left(\frac{\mathrm{d}S}{\mathrm{d}t}\right)^2} \tag{C.6}$$

The different functional forms lead to distinct mathematical behavior when applying the saddle-point approximation. In the zero-range case, the $\mathrm{d}S/\mathrm{d}t$ dependence cancels exactly, while for Coulomb potentials a residual $(\mathrm{d}S/\mathrm{d}t)^{-1}$ factor remains. This residual singularity requires careful treatment through advanced contour integration techniques.

For Coulomb potentials, the amplitude expression becomes:

$$T_0(\mathbf{p}) = \frac{\sqrt{2}}{\pi}(2I_p)^{5/4}\left(\mathcal{I} - \left.\frac{\exp(iS)}{2\left(\frac{\mathrm{d}S}{\mathrm{d}t}\right)^2}\right|_0^{T_p}\right) \tag{C.7}$$

where the principal integral is

$$\mathcal{I} = \frac{i}{2}\int_0^{T_p} \mathrm{d}t \left(\frac{\mathrm{d}S}{\mathrm{d}t}\right)^{-1} \exp(iS) \tag{C.8}$$

The integration contour deforms into the complex plane to capture both endpoint contributions at $t = 0$ and $t = T_p$, along with saddle-point contributions at critical points t_s. The complete integral decomposes as:

$$\mathcal{I} \approx \mathcal{I}_{\text{endpoints}} + \sum_s \mathcal{I}_s \tag{C.9}$$

The endpoint contributions through integration by parts become:

$$\mathcal{J}_{\text{endpoints}} = \left.\frac{\exp(iS)}{2\left(\frac{\mathrm{d}S}{\mathrm{d}t}\right)^2}\right|_0^{T_p} + O\left(\frac{\mathrm{d}^2 S}{\mathrm{d}t^2}\right) \tag{C.10}$$

The dominant first term exactly cancels the boundary contribution in the amplitude expression. Near each saddle point t_s, the action expands as

$$S(t) \approx S(t_s) + \frac{1}{2}S''(t_s)(t - t_s)^2 \tag{C.11}$$

$$\frac{\mathrm{d}S}{\mathrm{d}t} \approx S''(t_s)(t - t_s) \tag{C.12}$$

The local integral transforms to:

$$\mathcal{J}_s = \frac{i}{2}[S''(t_s)]^{-1} e^{iS(t_s)} \int_{C_s} \frac{\mathrm{d}t}{t - t_s} \exp\left(\frac{i}{2}S''(t_s)(t - t_s)^2\right) \tag{C.13}$$

For $S''(t_s) = i|S''(t_s)|e^{i\alpha}$, the steepest descent path follows:

$$t - t_s = \rho e^{-i\alpha/2}, \quad \rho \in (-\infty, \infty) \tag{C.14}$$

Application of the Sokhotski-Plemelj theorem yields the saddle-point contribution

$$\mathcal{J}_s = -\frac{\pi}{2}\frac{\exp(iS(t_s))}{S''(t_s)} \tag{C.15}$$

Combining all contributions yields the physically meaningful result:

$$T_0(\mathbf{p}) = -2^{-1/2}(2I_p)^{5/4} \sum_s [S''(t_s)]^{-1} \exp(iS(t_s)) \tag{C.16}$$

This expression demonstrates that proper treatment of the apparent singularity leads to a well-defined result where each saddle-point contribution is weighted by the inverse curvature of the action.

BIBLIOGRAPHY

[1] P. A. Franken, A. E. Hill, C. W. Peters, and G. Weinreich. "Generation of Optical Harmonics." In: *Phys. Rev. Lett.* 7 (4 1961), pp. 118–119. DOI: 10.1103/PhysRevLett.7.118. URL: https://link.aps.org/doi/10.1103/PhysRevLett.7.118.

[2] Steven Chu, J. E. Bjorkholm, A. Ashkin, and A. Cable. "Experimental Observation of Optically Trapped Atoms." In: *Phys. Rev. Lett.* 57 (3 1986), pp. 314–317. DOI: 10.1103/PhysRevLett.57.314. URL: https://link.aps.org/doi/10.1103/PhysRevLett.57.314.

[3] T. W. Ebbesen, H. J. Lezec, H. F. Ghaemi, T. Thio, and P. A. Wolff. "Extraordinary optical transmission through sub-wavelength hole arrays." In: *Nature* 391 (1998), pp. 667–669. DOI: 10.1038/35570.

[4] E. Goulielmakis et al. "Single-Cycle Nonlinear Optics." In: *Science* 320 (2008), pp. 1614–1617. DOI: 10.1126/science.1157846.

[5] A. Assion, T. Baumert, M. Bergt, T. Brixner, B. Kiefer, V. Seyfried, M. Strehle, and G. Gerber. "Control of Chemical Reactions by Feedback-Optimized Phase-Shaped Femtosecond Laser Pulses." In: *Science* 282 (1998), pp. 919–922. DOI: 10.1126/science.282.5390.919.

[6] Albert Einstein. "Über einen die Erzeugung und Verwandlung des Lichtes betreffenden heuristischen Gesichtspunkt." In: *Annalen der Physik* 322.6 (1905). Translated title: "On a Heuristic Point of View Concerning the Production and Transformation of Light", pp. 132–148. DOI: 10.1002/andp.19053220607. URL: https://onlinelibrary.wiley.com/doi/abs/10.1002/andp.19053220607.

[7] P. A. M. Dirac. "The Quantum Theory of the Emission and Absorption of Radiation." In: *Proceedings of the Royal Society of London. Series A* 114.767 (1927), pp. 243–265. DOI: 10.1098/rspa.1927.0039. URL: https://royalsocietypublishing.org/doi/10.1098/rspa.1927.0039.

[8] P. Agostini and G. Petite. "Photoelectric effect under strong irradiation." In: *Contemporary Physics* 29.1 (1988), pp. 57–77. DOI: 10.1080/00107518808213751. URL: https://doi.org/10.1080/00107518808213751.

[9] T. H. Maiman. "Stimulated Optical Radiation in Ruby." In: *Nature* 187.4736 (1960), pp. 493–494. DOI: 10.1038/187493a0. URL: https://www.nature.com/articles/187493a0.

[10] G. S. Voronov and N. B. Delone. "Ionization of the Xenon Atom by the Electric Field of Ruby Laser Emission." In: *Pis'ma v ZhETF* 1.2 (1965), p. 42. URL: http://jetpletters.ru/ps/0/article_24398.shtml.

[11] P. Agostini, F. Fabre, G. Mainfray, G. Petite, and N. K. Rahman. "Free-Free Transitions Following Six-Photon Ionization of Xenon Atoms." In: *Phys. Rev. Lett.* 42 (17 1979), pp. 1127–1130. DOI: 10.1103/PhysRevLett.42.1127. URL: https://link.aps.org/doi/10.1103/PhysRevLett.42.1127.

[12] Guillaume Petite, Pierre Agostini, and François Yergeau. "Intensity, pulse width, and polarization dependence of above-threshold-ionization electron spectra." In: *Journal of the Optical Society of America B* 4.5 (May 1987), pp. 765–769. DOI: 10.1364/JOSAB.4.000765. URL: https://opg.optica.org/josab/abstract.cfm?URI=josab-4-5-765.

[13] L. V. Keldysh. "Ionization in the field of a strong electromagnetic wave." In: *Zhurnal Eksperimental'noi i Teoreticheskoi Fiziki* 47 (1964). English translation: L. V. Keldysh, 1965, "Ionization in the field of a strong electromagnetic wave," Sov. Phys.–JETP, vol. 20, p. 1307, p. 1945.

[14] H. Barry Bebb and Albert Gold. "Multiphoton Ionization of Hydrogen and Rare-Gas Atoms." In: *Phys. Rev.* 143 (1 1966), pp. 1–24. DOI: 10.1103/PhysRev.143.1. URL: https://link.aps.org/doi/10.1103/PhysRev.143.1.

[15] P. B. Corkum. "Plasma perspective on strong field multiphoton ionization." In: *Phys. Rev. Lett.* 71 (13 1993), pp. 1994–1997. DOI: 10.1103/PhysRevLett.71.1994. URL: https://link.aps.org/doi/10.1103/PhysRevLett.71.1994.

[16] Ferenc Krausz and Misha Ivanov. "Attosecond physics." In: *Rev. Mod. Phys.* 81 (1 2009), pp. 163–234. DOI: 10.1103/RevModPhys.81.163. URL: https://link.aps.org/doi/10.1103/RevModPhys.81.163.

[17] Lisa Torlina and Olga Smirnova. "Time-dependent analytical *R*-matrix approach for strong-field dynamics. I. One-electron systems." In: *Phys. Rev. A* 86 (4 2012), p. 043408. DOI: 10.1103/PhysRevA.86.043408. URL: https://link.aps.org/doi/10.1103/PhysRevA.86.043408.

[18] J. Javanainen, J. H. Eberly, and Qichang Su. "Numerical simulations of multiphoton ionization and above-threshold electron spectra." In: *Phys. Rev. A* 38 (7 1988), pp. 3430–3446. DOI: 10.1103/PhysRevA.38.3430. URL: https://link.aps.org/doi/10.1103/PhysRevA.38.3430.

[19] Shih-Da Jheng and Tsin-Fu Jiang. "Solving time-dependent Schrödinger equation in momentum space with application to strong-field problems." In: *Phys. Scr* 97.4 (2022), p. 045402. DOI: 10.1088/1402-4896/ac5697. URL: https://dx.doi.org/10.1088/1402-4896/ac5697.

[20] Dieter Bauer and Peter Koval. "Qprop: A Schrödinger-solver for intense laser–atom interaction." In: *Comput. Phys. Commun* 174.5 (2006), pp. 396–421. ISSN: 0010-4655. DOI: https://doi.org/10.1016/j.cpc.2005.11.001. URL: https://www.sciencedirect.com/science/article/pii/S0010465505005825.

[21] Stefan Pabst and Robin Santra. "Strong-Field Many-Body Physics and the Giant Enhancement in the High-Harmonic Spectrum of Xenon." In: *Phys. Rev. Lett.* 111 (23 2013), p. 233005. DOI: 10.1103/PhysRevLett.111.233005. URL: https://link.aps.org/doi/10.1103/PhysRevLett.111.233005.

[22] Yiqi Fang, Feng-Xiao Sun, Qiongyi He, and Yunquan Liu. "Strong-Field Ionization of Hydrogen Atoms with Quantum Light." In: *Phys. Rev. Lett.* 130 (25 2023), p. 253201. DOI: 10.1103/PhysRevLett.130.253201. URL: https://link.aps.org/doi/10.1103/PhysRevLett.130.253201.

[23] YanLan Wang, ShaoGang Yu, RenPing Sun, HuiPeng Kang, SongPo Xu, XuanYang Lai, Wei Quan, and XiaoJun Liu. "Timing Correlated-Electron Emission from Strong Field Atomic Double Ionization with Polarization-Gated Attoclock." In: *Phys. Rev. Lett.* 132 (22 2024), p. 223202. DOI: 10.1103/PhysRevLett.132.223202. URL: https://link.aps.org/doi/10.1103/PhysRevLett.132.223202.

[24] J. Itatani, J. Levesque, D. Zeidler, Hiromichi Niikura, H. Pépin, J. C. Kieffer, P. B. Corkum, and D. M. Villeneuve. "Tomographic imaging of molecular orbitals." In: *Nature* 432.7019 (Dec. 2004), pp. 867–871. ISSN: 1476-4687. DOI: 10.1038/nature03183. URL: https://doi.org/10.1038/nature03183.

[25] M. Lein, N. Hay, R. Velotta, J. P. Marangos, and P. L. Knight. "Role of the Intramolecular Phase in High-Harmonic Generation." In: *Phys. Rev. Lett.* 88 (18 2002), p. 183903. DOI: 10.1103/PhysRevLett.88.183903. URL: https://link.aps.org/doi/10.1103/PhysRevLett.88.183903.

[26] Olga Smirnova, Yann Mairesse, Serguei Patchkovskii, Nirit Dudovich, David Villeneuve, Paul Corkum, and Misha Yu. Ivanov. "High harmonic interferometry of multi-electron dynamics in molecules." In: *Nature* 460.7258 (Aug. 2009), pp. 972–977. ISSN: 1476-4687. DOI: 10.1038/nature08253. URL: https://doi.org/10.1038/nature08253.

[27] P. Agostini, G. Barjot, J. Bonnal, G. Mainfray, C. Manus, and J. Morellec. "Multiphoton ionization of hydrogen and rare gases." In: *IEEE Journal of Quantum Electronics* 4.10 (1968), pp. 667–669. DOI: 10.1109/JQE.1968.1074955.

[28] G Mainfray and G Manus. "Multiphoton ionization of atoms." In: *Reports on Progress in Physics* 54.10 (1991), p. 1333. DOI: 10.1088/0034-4885/54/10/002. URL: https://dx.doi.org/10.1088/0034-4885/54/10/002.

[29] G. Sansone et al. "Isolated Single-Cycle Attosecond Pulses." In: *Science* 314.5798 (2006), pp. 443–446. DOI: 10.1126/science.1132838. eprint: https://www.science.org/doi/pdf/10.1126/science.1132838. URL: https://www.science.org/doi/abs/10.1126/science.1132838.

[30] Juergen Grotemeyer and Edward W. Schlag. "Biomolecules in the Gas Phase: Multiphoton Ionization Mass Spectrometry." In: *Accounts of Chemical Research* 22.11 (Nov. 1989), pp. 399–406. ISSN: 0001-4842. DOI: 10.1021/ar00167a005. URL: https://doi.org/10.1021/ar00167a005.

[31] O. Echt, P. D. Dao, S. Morgan, and Jr. Castleman A. W. "Multiphoton ionization of ammonia clusters and the dissociation dynamics of protonated cluster ions." In: *The Journal of Chemical Physics* 82.9 (May 1985), pp. 4076–4085. ISSN: 0021-9606. DOI: 10.1063/1.448849. eprint: https://pubs.aip.org/aip/jcp/article-pdf/82/9/4076/18952927/4076_1_online.pdf. URL: https://doi.org/10.1063/1.448849.

[32] Ralph Howard Fowler and Lothar Nordheim. "Electron Emission in Intense Electric Fields." In: *Proceedings of the Royal Society of London A* 119.781 (1928), pp. 173–181. DOI: 10.1098/rspa.1928.0091. URL: https://doi.org/10.1098/rspa.1928.0091.

[33] J. R. Oppenheimer. "Three Notes on the Quantum Theory of Aperiodic Effects." In: *Phys. Rev.* 31 (1 1928), pp. 66–81.

[34] Maxim V. Ammosov, Nikolai B. Delone, and Vladimir P. Krainov. "Tunnel Ionization of Complex Atoms and Atomic Ions in Electromagnetic Field." In: *Proc. SPIE* 0664 (1986). ADK theory - Extended Keldysh formalism for complex atoms, High Intensity Laser Processes. DOI: 10.1117/12.938695. URL: https://doi.org/10.1117/12.938695.

[35] F H M Faisal. "Multiple absorption of laser photons by atoms." In: *Journal of Physics B: Atomic and Molecular Physics* 6.4 (1973), p. L89. DOI: 10.1088/0022-3700/6/4/011. URL: https://dx.doi.org/10.1088/0022-3700/6/4/011.

[36] Howard R. Reiss. "Effect of an intense electromagnetic field on a weakly bound system." In: *Phys. Rev. A* 22 (5 1980), pp. 1786–1813. DOI: 10.1103/PhysRevA.22.1786. URL: https://link.aps.org/doi/10.1103/PhysRevA.22.1786.

[37] I. Ivanov, A. Kheifets, J. Calvert, S. Goodall, X. Wang, D. Kielpinski, I. V. Litvinyuk, and R. T. Sang. "Transverse electron momentum distribution in tunneling and over the barrier ionization by laser pulses with varying ellipticity." In: *Scientific Reports* 6 (2016), p. 19002. DOI: 10.1038/srep19002. URL: https://doi.org/10.1038/srep19002.

[38] James S. Cohen. "Reexamination of over-the-barrier and tunneling ionization of the hydrogen atom in an intense field." In: *Phys. Rev. A* 64 (4 2001), p. 043412. DOI: 10.1103/PhysRevA.64.043412. URL: https://link.aps.org/doi/10.1103/PhysRevA.64.043412.

[39] Michael Spanner, Olga Smirnova, Paul B Corkum, and Misha Yu Ivanov. "Reading diffraction images in strong field ionization of diatomic molecules." In: *Journal of Physics B: Atomic, Molecular and Optical Physics* 37.12 (2004), p. L243. DOI: 10.1088/0953-4075/37/12/L02. URL: https://dx.doi.org/10.1088/0953-4075/37/12/L02.

[40] S. N. Yurchenko, S. Patchkovskii, I. V. Litvinyuk, P. B. Corkum, and G. L. Yudin. "Laser-Induced Interference, Focusing, and Diffraction of Rescattering Molecular Photoelectrons." In: *Phys. Rev. Lett.* 93 (22 2004), p. 223003. DOI: 10.1103/PhysRevLett.93.223003. URL: https://link.aps.org/doi/10.1103/PhysRevLett.93.223003.

[41] Y. Huismans et al. "Time-Resolved Holography with Photoelectrons." In: *Science* 331.6013 (2011), pp. 61–64. DOI: 10.1126/science.1198450. eprint: https://www.science.org/doi/pdf/10.1126/science.1198450. URL: https://www.science.org/doi/abs/10.1126/science.1198450.

[42] G. G. Paulus, W. Nicklich, Huale Xu, P. Lambropoulos, and H. Walther. "Plateau in above threshold ionization spectra." In: *Phys. Rev. Lett.* 72 (18 1994), pp. 2851–2854. DOI: 10.1103/PhysRevLett.72.2851. URL: https://link.aps.org/doi/10.1103/PhysRevLett.72.2851.

[43] B. Walker, B. Sheehy, L. F. DiMauro, P. Agostini, K. J. Schafer, and K. C. Kulander. "Precision Measurement of Strong Field Double Ionization of Helium." In: *Phys. Rev. Lett.* 73 (9 1994), pp. 1227–1230. DOI: 10.1103/PhysRevLett.73.1227. URL: https://link.aps.org/doi/10.1103/PhysRevLett.73.1227.

[44] Fang Liu, Zhangjin Chen, Toru Morishita, Klaus Bartschat, Birger Böning, and Stephan Fritzsche. "Single-cycle versus multicycle nonsequential double ionization of argon." In: *Phys. Rev. A* 104 (1 2021), p. 013105. DOI: 10.1103/PhysRevA.104.013105. URL: https://link.aps.org/doi/10.1103/PhysRevA.104.013105.

[45] Fang Liu, Shuqi Li, Zhangjin Chen, Birger Böning, and Stephan Fritzsche. "Nonsequential double ionization of Ne with elliptically polarized laser pulses." In: *Phys. Rev. A* 106 (4 2022), p. 043120. DOI: 10.1103/PhysRevA.106.043120. URL: https://link.aps.org/doi/10.1103/PhysRevA.106.043120.

[46] Anne Weber, Birger Böning, Björn Minneker, and Stephan Fritzsche. "Generation of elliptically polarized high-order harmonic radiation with bi-elliptical two-color laser beams." In: *Phys. Rev. A* 104 (6 2021), p. 063118. DOI: 10.1103/PhysRevA.104.063118. URL: https://link.aps.org/doi/10.1103/PhysRevA.104.063118.

[47] Björn Minneker, Birger Böning, Anne Weber, and Stephan Fritzsche. "Torus-knot angular momentum in twisted attosecond pulses from high-order harmonic generation." In: *Phys. Rev. A* 104 (5 2021), p. 053116. DOI: 10.1103/PhysRevA.104.053116. URL: https://link.aps.org/doi/10.1103/PhysRevA.104.053116.

[48] Willi Paufler, Birger Böning, and Stephan Fritzsche. "Coherence control in high-order harmonic generation with Laguerre-Gaussian beams." In: *Phys. Rev. A* 100 (1 2019), p. 013422. DOI: 10.1103/PhysRevA.100.013422. URL: https://link.aps.org/doi/10.1103/PhysRevA.100.013422.

[49] Birger Böning, Willi Paufler, and Stephan Fritzsche. "Attosecond streaking with twisted X waves and intense infrared pulses." In: *Phys. Rev. A* 96 (4 2017), p. 043423. DOI: 10.1103/PhysRevA.96.043423. URL: https://link.aps.org/doi/10.1103/PhysRevA.96.043423.

[50] P. Kruit, J. Kimman, H. G. Muller, and M. J. van der Wiel. "Electron spectra from multiphoton ionization of xenon at 1064, 532, and 355 nm." In: *Phys. Rev. A* 28 (1 1983), pp. 248–255. DOI: 10.1103/PhysRevA.28.248. URL: https://link.aps.org/doi/10.1103/PhysRevA.28.248.

[51] Ph. A. Korneev et al. "Interference Carpets in Above-Threshold Ionization: From the Coulomb-Free to the Coulomb-Dominated Regime." In: *Phys. Rev. Lett.* 108 (22 2012), p. 223601. DOI: 10.1103/PhysRevLett.108.223601. URL: https://link.aps.org/doi/10.1103/PhysRevLett.108.223601.

[52] W. Becker, F. Grasbon, R. Kopold, D.B. Milošević, G.G. Paulus, and H. Walther. "Above-Threshold Ionization: From Classical Features to Quantum Effects." In: ed. by Benjamin Bederson and Herbert Walther. Vol. 48. Advances In Atomic, Molecular, and Optical Physics. Academic Press, 2002, pp. 35–98. DOI: https://doi.org/10.1016/S1049-250X(02)80006-4. URL: https://www.sciencedirect.com/science/article/pii/S1049250X02800064.

[53] Noslen Suárez, Alexis Chacón, Marcelo F. Ciappina, Jens Biegert, and Maciej Lewenstein. "Above-threshold ionization and photoelectron spectra in atomic systems driven by strong laser fields." In: *Phys. Rev. A* 92 (6 2015), p. 063421. DOI: 10.1103/PhysRevA.92.063421. URL: https://link.aps.org/doi/10.1103/PhysRevA.92.063421.

[54] Guillaume Petite, Pierre Agostini, and François Yergeau. "Intensity, pulse width, and polarization dependence of above-threshold-ionization electron spectra." In: *J. Opt. Soc. Am. B* 4.5 (1987), pp. 765–769. DOI: 10.1364/JOSAB.4.000765. URL: https://opg.optica.org/josab/abstract.cfm?URI=josab-4-5-765.

[55] D. B. Milošević, E. Hasović, M. Busuladžić, A. Gazibegović-Busuladžić, and W. Becker. "Intensity-dependent enhancements in high-order above-threshold ionization." In: *Physical Review A* 76.5 (Nov. 2007), p. 053410. DOI: 10.1103/PhysRevA.76.053410. URL: https://link.aps.org/doi/10.1103/PhysRevA.76.053410.

[56] P. B. Corkum, N. H. Burnett, and F. Brunel. "Above-threshold ionization in the long-wavelength limit." In: *Phys. Rev. Lett.* 62 (11 1989), pp. 1259–1262. DOI: 10.1103/PhysRevLett.62.1259. URL: https://link.aps.org/doi/10.1103/PhysRevLett.62.1259.

[57] T Marchenko, H G Muller, K J Schafer, and M J J Vrakking. "Wavelength dependence of photoelectron spectra in above-threshold ionization." In: *Journal of Physics B: Atomic, Molecular and Optical Physics* 43.18 (2010), p. 185001. DOI: 10.1088/0953-4075/43/18/185001. URL: https://dx.doi.org/10.1088/0953-4075/43/18/185001.

[58] Haiying Yuan, Yujun Yang, Fuming Guo, Jun Wang, Jigen Chen, Wei Feng, and Zhiwen Cui. "Effect of pulse duration on the above-threshold ionization of a hydrogen atom irradiated by a 400 nm intense laser." In: *Opt. Express* 31.15 (2023), pp. 24213–24229. DOI: 10.1364/OE.495313. URL: https://opg.optica.org/oe/abstract.cfm?URI=oe-31-15-24213.

[59] Birger Böning and Stephan Fritzsche. "Partial-wave representation of the strong-field approximation. II. Coulomb asymmetry in the photoelectron angular distribution of many-electron atoms." In: *Phys. Rev. A* 107 (2 2023), p. 023108. DOI:

10.1103/PhysRevA.107.023108. URL: https://link.aps.org/doi/10.1103/PhysRevA.107.023108.

[60] D. Trabert, A. Geyer, N. Anders, M. Hofmann, M. S. Schöffler, L. Ph. H. Schmidt, T. Jahnke, M. Kunitski, R. Dörner, and S. Eckart. "Ideal two-color field ratio for holographic angular streaking of electrons." In: *Phys. Rev. Res.* 5 (4 2023), p. 043245. DOI: 10.1103/PhysRevResearch.5.043245. URL: https://link.aps.org/doi/10.1103/PhysRevResearch.5.043245.

[61] Kang Lin et al. "Photoelectron energy peaks shift against the radiation pressure in strong-field ionization." In: *Science Advances* 8.12 (2022), eabn7386. DOI: 10.1126/sciadv.abn7386. eprint: https://www.science.org/doi/pdf/10.1126/sciadv.abn7386. URL: https://www.science.org/doi/abs/10.1126/sciadv.abn7386.

[62] W. Quan et al. "Classical Aspects in Above-Threshold Ionization with a Mid-infrared Strong Laser Field." In: *Phys. Rev. Lett.* 103 (9 2009), p. 093001. DOI: 10.1103/PhysRevLett.103.093001. URL: https://link.aps.org/doi/10.1103/PhysRevLett.103.093001.

[63] E. Hasović and D. B. Milošević. "Strong-field approximation for above-threshold ionization of polyatomic molecules." In: *Physical Review A* 86.4 (Oct. 2012), p. 043429. ISSN: 1050-2947. DOI: 10.1103/PhysRevA.86.043429. URL: https://link.aps.org/doi/10.1103/PhysRevA.86.043429.

[64] D. B. Milošević and W. Becker. "Atom-Volkov strong-field approximation for above-threshold ionization." In: *Physical Review A* 99.4 (Apr. 2019), p. 043411. ISSN: 2469-9926. DOI: 10.1103/PhysRevA.99.043411. URL: https://link.aps.org/doi/10.1103/PhysRevA.99.043411.

[65] Dane R. Austin and Jens Biegert. "Strong-field approximation for the wavelength scaling of high-harmonic generation." In: *Phys. Rev. A* 86 (2 2012), p. 023813. DOI: 10.1103/PhysRevA.86.023813. URL: https://link.aps.org/doi/10.1103/PhysRevA.86.023813.

[66] D. Arbó, K. Tőkési, and J. Miraglia. "Limitations of the strong field approximation in ionization of the hydrogen atom by ultrashort pulses." In: *European Physical Journal D* 51 (2009), pp. 303–312. ISSN: 1434-6060. DOI: 10.1140/epjd/e2008-00267-y. URL: https://doi.org/10.1140/epjd/e2008-00267-y.

[67] D. Bauer, D. B. Milošević, and W. Becker. "On the validity of the strong field approximation and simple man's theory." In: *Journal of Modern Optics* 53.1–2 (2006), pp. 135–147. ISSN: 0950-0340. DOI: 10.1080/09500340500217258. URL: https://doi.org/10.1080/09500340500217258.

[68] N. I. Shvetsov-Shilovski, M. Lein, L. B. Madsen, E. Räsänen, C. Lemell, J. Burgdörfer, D. G. Arbó, and K. Tőkési. "Semiclassical two-step model for strong-field ionization." In: *Physical Review A* 94.1 (July 2016), p. 013415. ISSN: 2469-9926. DOI: 10.1103/PhysRevA.94.013415. URL: https://link.aps.org/doi/10.1103/PhysRevA.94.013415.

[69] Min Li, Ji-Wei Geng, Hong Liu, Yongkai Deng, Chengyin Wu, Liang-You Peng, Qihuang Gong, and Yunquan Liu. "Classical-Quantum Correspondence for Above-Threshold Ionization." In: *Phys. Rev. Lett.* 112 (11 2014), p. 113002. DOI: 10.1103/PhysRevLett.112.113002. URL: https://link.aps.org/doi/10.1103/PhysRevLett.112.113002.

[70] T. Rook, D. Habibović, L. Cruz Rodriguez, D. B. Milošević, and C. Figueira de Morisson Faria. "Impact of the continuum Coulomb interaction in quantum-orbit-based treatments of high-order above-threshold ionization." In: *Physical Review A* 109.3 (Mar. 2024), p. 033115. ISSN: 2469-9926. DOI: 10.1103/PhysRevA.109.033115. URL: https://link.aps.org/doi/10.1103/PhysRevA.109.033115.

[71] Shidong Yang, Xiaohong Song, Xiwang Liu, Hongdan Zhang, Guangluo Shi, Xianhuan Yu, Yajuan Tang, Jing Chen, and Weifeng Yang. "Coulomb-corrected strong-field approximation based on a genetic algorithm." In: *Laser Physics Letters* 17.9 (2020), p. 095301. DOI: 10.1088/1612-202X/aba196. URL: https://dx.doi.org/10.1088/1612-202X/aba196.

[72] Michael Klaiber, Jiří Daněk, Enderalp Yakaboylu, Karen Z. Hatsagortsyan, and Christoph H. Keitel. "Strong-field ionization via a high-order Coulomb-corrected strong-field approximation." In: *Physical Review A* 95.2 (Feb. 2017), p. 023403. ISSN: 2469-9926. DOI: 10.1103/PhysRevA.95.023403. URL: https://link.aps.org/doi/10.1103/PhysRevA.95.023403.

[73] Nicholas Werby, Andrew S. Maxwell, Ruaridh Forbes, Carla Figueira de Morisson Faria, and Philip H. Bucksbaum. "Probing two-path electron quantum interference in strong-field ionization with time-correlation filtering." In: *Phys. Rev. A* 106 (3 2022), p. 033118. DOI: 10.1103/PhysRevA.106.033118. URL: https://link.aps.org/doi/10.1103/PhysRevA.106.033118.

[74] Birger Böning and Stephan Fritzsche. "Partial-wave representation of the strong-field approximation." In: *Phys. Rev. A* 102 (5 2020), p. 053108. DOI: 10.1103/PhysRevA.102.053108. URL: https://link.aps.org/doi/10.1103/PhysRevA.102.053108.

[75] Birger Böning and Stephan Fritzsche. "Partial-wave representation of the strong-field approximation. II. Coulomb asymmetry in the photoelectron angular distribution of many-electron atoms." In: *Phys. Rev. A* 107 (2 2023), p. 023108. DOI: 10.1103/PhysRevA.107.023108. URL: https://link.aps.org/doi/10.1103/PhysRevA.107.023108.

[76] James Clerk Maxwell. "A Dynamical Theory of the Electromagnetic Field." In: *Philosophical Transactions of the Royal Society of London* 155 (1865), pp. 459–512. DOI: 10.1098/rstl.1865.0008.

[77] John David Jackson. *Classical Electrodynamics*. 3rd ed. Hoboken, New Jersey: John Wiley & Sons, 1999. ISBN: 978-0-471-30932-1.

[78] Bahaa E. A. Saleh and Malvin Carl Teich. *Fundamentals of Photonics*. 1st ed. Wiley Series in Pure and Applied Optics. New York: John Wiley & Sons, 1991. ISBN: 978-0-471-83965-1.

[79] Emilio Pisanty, Daniel D Hickstein, Benjamin R Galloway, Charles G Durfee, Henry C Kapteyn, Margaret M Murnane, and Misha Ivanov. "High harmonic interferometry of the Lorentz force in strong mid-infrared laser fields." In: *New Journal of Physics* 20.5 (2018), p. 053036. DOI: 10.1088/1367-2630/aabb4d. URL: https://dx.doi.org/10.1088/1367-2630/aabb4d.

[80] Stephan Fritzsche and Birger Böning. "Lorentz-force shifts in strong-field ionization with mid-infrared laser fields." In: *Phys. Rev. Res.* 4 (3 2022), p. 033031. DOI: 10.1103/PhysRevResearch.4.033031. URL: https://link.aps.org/doi/10.1103/PhysRevResearch.4.033031.

[81] O Matula, A G Hayrapetyan, V G Serbo, A Surzhykov, and S Fritzsche. "Atomic ionization of hydrogen-like ions by twisted photons: angular distribution of emitted electrons." In: *Journal of Physics B: Atomic, Molecular and Optical Physics* 46.20 (2013), p. 205002. DOI: 10.1088/0953-4075/46/20/205002. URL: https://dx.doi.org/10.1088/0953-4075/46/20/205002.

[82] A. Surzhykov, D. Seipt, and S. Fritzsche. "Probing the energy flow in Bessel light beams using atomic photoionization." In: *Phys. Rev. A* 94 (3 2016), p. 033420. DOI: 10.1103/PhysRevA.94.033420. URL: https://link.aps.org/doi/10.1103/PhysRevA.94.033420.

[83] G. F. Quinteiro, D. E. Reiter, and T. Kuhn. "Formulation of the twisted-light–matter interaction at the phase singularity: Beams with strong magnetic fields." In: *Phys. Rev. A* 95 (1 2017), p. 012106. DOI: 10.1103/PhysRevA.95.012106. URL: https://link.aps.org/doi/10.1103/PhysRevA.95.012106.

[84] Willi Paufler, Birger Böning, and Stephan Fritzsche. "Strong-field ionization with twisted laser pulses." In: *Phys. Rev. A* 97 (4 2018), p. 043418. DOI: 10.1103/PhysRevA.97.043418. URL: https://link.aps.org/doi/10.1103/PhysRevA.97.043418.

[85] Birger Böning, Willi Paufler, and Stephan Fritzsche. "Above-threshold ionization by few-cycle Bessel pulses carrying orbital angular momentum." In: *Phys. Rev. A* 98 (2 2018), p. 023407. DOI: 10.1103/PhysRevA.98.023407. URL: https://link.aps.org/doi/10.1103/PhysRevA.98.023407.

[86] D. B. Milošević, G. G. Paulus, D. Bauer, and W. Becker. "Above-threshold ionization by few-cycle pulses." In: *Journal of Physics B: Atomic, Molecular and Optical Physics* 39.14 (July 2006), R203. ISSN: 0953-4075. DOI: 10.1088/0953-4075/39/14/R01. URL: https://dx.doi.org/10.1088/0953-4075/39/14/R01.

[87] C. D. Lin, Anh-Thu Le, Cheng Jin, and Hui Wei. *Attosecond and Strong-Field Physics: Principles and Applications*. Cambridge University Press, 2018.

[88] Arno Bohm. "Time Evolution." In: *Quantum Mechanics: Foundations and Applications*. Berlin, Heidelberg: Springer Berlin Heidelberg, 1986, pp. 310–327. ISBN: 978-3-662-01168-3. DOI: 10.1007/978-3-662-01168-3_12. URL: https://doi.org/10.1007/978-3-662-01168-3_12.

[89] J. J. Sakurai and Jim Napolitano. *Modern Quantum Mechanics*. 3rd ed. Cambridge: Cambridge University Press, 2020. ISBN: 978-1-108-49969-6. DOI: 10.1017/9781108770340. URL: https://doi.org/10.1017/9781108770340.

[90] Thomas Brabec, ed. *Strong Field Laser Physics*. 1st ed. Vol. 134. Springer Series in Optical Sciences. New York, NY: Springer, 2008, pp. XV + 592. ISBN: 978-0-387-40077-8. DOI: 10.1007/978-0-387-34755-4. URL: https://doi.org/10.1007/978-0-387-34755-4.

[91] Y. J. Chen and Bambi Hu. "Strong-field approximation for diatomic molecules: Comparison between the length gauge and the velocity gauge." In: *Phys. Rev. A* 80 (3 2009), p. 033408. DOI: 10.1103/PhysRevA.80.033408. URL: https://link.aps.org/doi/10.1103/PhysRevA.80.033408.

[92] Thomas Kim Kjeldsen and Lars Bojer Madsen. "Strong-field ionization of N2: length and velocity gauge strong-field approximation and tunnelling theory." In: *Journal of Physics B: Atomic, Molecular and Optical Physics* 37.10 (2004), p. 2033. DOI: 10.1088/0953-4075/37/10/003. URL: https://dx.doi.org/10.1088/0953-4075/37/10/003.

[93] H. R. Reiss. *Dual gauge concepts in electrodynamics, and new limitations on gauge invariance*. 2022. arXiv: 2106.10226 [physics.gen-ph]. URL: https://arxiv.org/abs/2106.10226.

[94] J. Vábek, H. Bachau, and F. Catoire. "Ionization dynamics and gauge invariance." In: *Physical Review A* 106.5 (Nov. 2022), p. 053115. ISSN: 2469-9926. DOI: 10.1103/PhysRevA.106.053115. URL: https://link.aps.org/doi/10.1103/PhysRevA.106.053115.

[95] D. Bauer, D. B. Milošević, and W. Becker. "Strong-field approximation for intense-laser–atom processes: The choice of gauge." In: *Physical Review A* 72.2 (Aug. 2005), p. 023415. ISSN: 1050-2947. DOI: 10.1103/PhysRevA.72.023415. URL: https://link.aps.org/doi/10.1103/PhysRevA.72.023415.

[96] C. T. L. Smeenk, L. Arissian, B. Zhou, A. Mysyrowicz, D. M. Villeneuve, A. Staudte, and P. B. Corkum. "Partitioning of the Linear Photon Momentum in Multiphoton Ionization." In: *Phys. Rev. Lett.* 106 (19 2011), p. 193002. DOI: 10.1103/PhysRevLett.106.193002. URL: https://link.aps.org/doi/10.1103/PhysRevLett.106.193002.

[97] M. C. Suster, J. Derlikiewicz, K. Krajewska, F. Cajiao Vélez, and J. Z. Kamiński. "Nondipole signatures in ionization and high-order harmonic generation." In: *Physical Review A* 107.5 (May 2023), p. 053112. ISSN: 2469-9926. DOI: 10.1103/PhysRevA.107.053112. URL: https://link.aps.org/doi/10.1103/PhysRevA.107.053112.

[98] Kang Lin et al. "Photoelectron energy peaks shift against the radiation pressure in strong-field ionization." In: *Science Advances* 8 (2022), eabn7386. ISSN: 2375-2548. DOI: 10.1126/sciadv.abn7386.

[99] Morten Førre. "Nondipole effects and photoelectron momentum shifts in strong-field ionization by infrared light." In: *Physical Review A* 106.1 (July 2022), p. 013104. ISSN: 2469-9926. DOI: 10.1103/PhysRevA.106.013104. URL: https://link.aps.org/doi/10.1103/PhysRevA.106.013104.

[100] Lars Bojer Madsen. "Disappearance and reappearance of above-threshold-ionization peaks." In: *Phys. Rev. A* 106 (4 2022), p. 043118. DOI: 10.1103/PhysRevA.106.043118. URL: https://link.aps.org/doi/10.1103/PhysRevA.106.043118.

[101] Lars Bojer Madsen. "Nondipole effects in tunneling ionization by intense laser pulses." In: *Phys. Rev. A* 105 (4 2022), p. 043107. DOI: 10.1103/PhysRevA.105.043107. URL: https://link.aps.org/doi/10.1103/PhysRevA.105.043107.

[102] Rešad Kahvedžić and Stefanie Gräfe. "Strong-field approximation with leading-order nondipole corrections." In: *Physical Review A* 105.6 (June 2022), p. 063102. ISSN: 2469-9926. DOI: 10.1103/PhysRevA.105.063102. URL: https://link.aps.org/doi/10.1103/PhysRevA.105.063102.

[103] Pei-Lun He, Michael Klaiber, Karen Z. Hatsagortsyan, and Christoph H. Keitel. "Nondipole Coulomb sub-barrier ionization dynamics and photon momentum sharing." In: *Phys. Rev. A* 105 (3 2022), p. L031102. DOI: 10.1103/PhysRevA.105.L031102. URL: https://link.aps.org/doi/10.1103/PhysRevA.105.L031102.

[104] Simon Vendelbo Bylling Jensen, Mads Middelhede Lund, and Lars Bojer Madsen. "Nondipole strong-field-approximation Hamiltonian." In: *Phys. Rev. A* 101 (4 2020), p. 043408. DOI: 10.1103/PhysRevA.101.043408. URL: https://link.aps.org/doi/10.1103/PhysRevA.101.043408.

[105] Birger Böning, Willi Paufler, and Stephan Fritzsche. "Nondipole strong-field approximation for spatially structured laser fields." In: *Phys. Rev. A* 99 (5 2019), p. 053404. DOI: 10.1103/PhysRevA.99.053404. URL: https://link.aps.org/doi/10.1103/PhysRevA.99.053404.

[106] Arjun Nayak et al. "Saddle point approaches in strong field physics and generation of attosecond pulses." In: *Physics Reports* 833 (Nov. 2019), pp. 1–52. ISSN: 0370-1573. DOI: 10.1016/j.physrep.2019.10.002. URL: https://www.sciencedirect.com/science/article/pii/S0370157319303096.

[107] A. Jašarević, E. Hasović, R. Kopold, W. Becker, and D. B. Milošević. "Application of the saddle-point method to strong-laser-field ionization." In: *Journal of Physics A: Mathematical and Theoretical* 53.12 (Mar. 2020), p. 125201. ISSN: 1751-8121. DOI: 10.1088/1751-8121/ab749b. URL: https://dx.doi.org/10.1088/1751-8121/ab749b.

[108] Anne Weber, Margarita Khokhlova, and Emilio Pisanty. "Quantum tunneling without a barrier." In: *Phys. Rev. A* 111 (4 2025), p. 043103. DOI: 10.1103/PhysRevA.111.043103. URL: https://link.aps.org/doi/10.1103/PhysRevA.111.043103.

[109] Thomas Kim Kjeldsen and Lars Bojer Madsen. "Strong-field ionization of atoms and molecules: The two-term saddle-point method." In: *Phys. Rev. A* 74 (2 2006), p. 023407. DOI: 10.1103/PhysRevA.74.023407. URL: https://link.aps.org/doi/10.1103/PhysRevA.74.023407.

[110] Yulian V. Vanne and Alejandro Saenz. "Exact Keldysh theory of strong-field ionization: Residue method versus saddle-point approximation." In: *Phys. Rev. A* 75 (3 2007), p. 033403. DOI: 10.1103/PhysRevA.75.033403. URL: https://link.aps.org/doi/10.1103/PhysRevA.75.033403.

[111] Norman Bleistein and Richard A. Handelsman. *Asymptotic Expansions of Integrals*. English. New. Illustrated. New York: Holt, Rinehart and Winston, 1975, p. 425. ISBN: 0030835968, 9780030835964.

[112] Valery Serov. *Fourier Series, Fourier Transform and Their Applications to Mathematical Physics*. English. 1st ed. Applied Mathematical Sciences. 4 b/w illustrations. Cham: Springer International Publishing, 2017, pp. xi, 534. ISBN: 978-3-319-65261-0. DOI: 10.1007/978-3-319-65262-7. URL: https://doi.org/10.1007/978-3-319-65262-7.

[113] M. Lewenstein, Ph. Balcou, M. Yu. Ivanov, A. L'Huillier, and P. B. Corkum. "Theory of high-harmonic generation by low-frequency laser fields." In: *Phys. Rev. A* 49 (3 1994), pp. 2117–2132. DOI: 10.1103/PhysRevA.49.2117.

[114] D. Agačević, N. Ibrišimović, D. Škrgić, and et al. "Above-threshold ionization by a strong circularly polarized laser pulse assisted by a terahertz pulse." In: *European Physical Journal D* 78 (2024), p. 128. ISSN: 1434-6060. DOI: 10.1140/epjd/s10053-024-00920-9. URL: https://doi.org/10.1140/epjd/s10053-024-00920-9.

[115] L. Torlina, O. Smirnova, H. G. Müller, and M. Ivanov. "Interpreting attoclock measurements of tunneling times." In: *Nature Physics* 11 (2015), pp. 503–508. DOI: 10.1038/nphys3340.

[116] I. A. Ivanov. "Time delay in strong-field photoionization of a hydrogen atom." In: *Phys. Rev. A* 83 (2 2011), p. 023421. DOI: 10.1103/PhysRevA.83.023421. URL: https://link.aps.org/doi/10.1103/PhysRevA.83.023421.

[117] S V Popruzhenko. "Keldysh theory of strong field ionization: history, applications, difficulties and perspectives." In: *Journal of Physics B: Atomic, Molecular and Optical Physics* 47.20 (2014), p. 204001. DOI: 10.1088/0953-4075/47/20/204001. URL: https://dx.doi.org/10.1088/0953-4075/47/20/204001.

[118] P. Eckle, A. N. Pfeiffer, C. Cirelli, A. Staudte, R. Dörner, H. G. Muller, M. Büttiker, and U. Keller. "Attosecond ionization and tunneling delay time measurements in helium." In: *Science* 322.5907 (2008), pp. 1525–1529. DOI: 10.1126/science.1163439.

[119] Sidney Coleman. "Aspects of Symmetry: Selected Erice Lectures." In: (1985). Instantons in quantum mechanics.

[120] S. V. Popruzhenko, G. G. Paulus, and D. Bauer. "Coulomb-corrected quantum trajectories in strong-field ionization." In: *Phys. Rev. A* 77 (5 2008), p. 053409. DOI: 10.1103/PhysRevA.77.053409. URL: https://link.aps.org/doi/10.1103/PhysRevA.77.053409.

[121] D. B. Milošević. "Application of the uniform approximation to integrals occurring in ionization by a strong elliptically polarized laser field." In: *Physical Review A* 111.5 (May 2025). Phys. Rev. A, p. 053105. ISSN: 2469-9926. DOI: 10.1103/PhysRevA.111.053105. URL: https://link.aps.org/doi/10.1103/PhysRevA.111.053105.

[122] Jeff Bezanson, Jiahao Chen, Benjamin Chung, Stefan Karpinski, Viral B. Shah, Jan Vitek, and Lionel Zoubritzky. "Julia: dynamism and performance reconciled by design." In: *Proc. ACM Program. Lang.* 2.OOPSLA (Oct. 2018). DOI: 10.1145/3276490. URL: https://doi.org/10.1145/3276490.

[123] Patrick Kofod Mogensen and Asbjørn Nilsen Riseth. "Optim: A mathematical optimization package for Julia." In: *Journal of Open Source Software* 3.24 (2018), p. 615. DOI: 10.21105/joss.00615.

[124] Patrick Kofod Mogensen et al. *JuliaNLSolvers/NLsolve.jl: v4.5.1*. Version v4.5.1. Dec. 2020. DOI: 10.5281/zenodo.4404703. URL: https://doi.org/10.5281/zenodo.4404703.

[125] Tjalling J. Ypma. "Historical Development of the Newton-Raphson Method." In: *SIAM Review* 37.4 (1995), pp. 531–551. DOI: 10.1137/1037125.

[126] John Hubbard, Dierk Schleicher, and Scott Sutherland. "How to Find All Roots of Complex Polynomials by Newton's Method." In: *Inventiones Mathematicae* 146.1 (2001), pp. 1–33. DOI: 10.1007/s002220100149. URL: https://doi.org/10.1007/s002220100149.

[127] J. M. Ortega and W. C. Rheinboldt. *Iterative Solution of Nonlinear Equations in Several Variables*. Society for Industrial and Applied Mathematics, 2000. DOI: 10.1137/1.9780898719468. eprint: https://epubs.siam.org/doi/pdf/10.1137/1.9780898719468. URL: https://epubs.siam.org/doi/abs/10.1137/1.9780898719468.

[128] Björn Minneker, Birger Böning, and Stephan Fritzsche. "Generalized nondipole strong-field approximation of high-order harmonic generation." In: *Phys. Rev. A* 106 (5 2022), p. 053109. DOI: 10.1103/PhysRevA.106.053109. URL: https://link.aps.org/doi/10.1103/PhysRevA.106.053109.

[129] Danish Furekh Dar and Stephan Fritzsche. "Comparison between Jacobi-Anger and saddle point methods to treat Above-threshold ionization." In: *Journal of Physics B: Atomic, Molecular and Optical Physics* (2025). URL: http://iopscience.iop.org/article/10.1088/1361-6455/ae187b.

[130] Danish Furekh Dar and Stephan Fritzsche. "Nonlinear interference and electron dynamics: Probing photoelectron momentum distributions in strong-field ionization." In: *Phys. Rev. A* 109 (4 2024), p. L041101. DOI: 10.1103/PhysRevA.109.L041101. URL: https://link.aps.org/doi/10.1103/PhysRevA.109.L041101.

[131] Danish Furekh Dar, Björn Minneker, and Stephan Fritzsche. "Nondipole strong-field approximation for above-threshold ionization in a few-cycle pulse." In: *Phys. Rev. A* 107 (5 2023), p. 053102. DOI: 10.1103/PhysRevA.107.053102. URL: https://link.aps.org/doi/10.1103/PhysRevA.107.053102.

[132] D. F. Dar and S. Fritzsche. "Pulse Cycle Dependent Nondipole Effects in Above-Threshold Ionization." In: *Atoms* 11.6 (2023), p. 97. DOI: 10.3390/atoms11060097. URL: https://doi.org/10.3390/atoms11060097.

[133] Danish Furekh Dar, Anne Weber, Shreyas Ramakrishna, and Stephan Fritzsche. "Photoionization dynamics in intense few-cycle twisted laser pulses." In: *Phys. Rev. A* 111 (5 2025), p. 053113. DOI: 10.1103/PhysRevA.111.053113. URL: https://link.aps.org/doi/10.1103/PhysRevA.111.053113.

[134] C. P. J. Martiny and L. B. Madsen. "Finite-bandwidth effects in strong-field ionization of atoms by few-cycle circularly polarized laser pulses." In: *Phys. Rev. A* 76 (4 2007), p. 043416. DOI: 10.1103/PhysRevA.76.043416. URL: https://link.aps.org/doi/10.1103/PhysRevA.76.043416.

[135] C P J Martiny, M Abu-samha, and L B Madsen. "Counterintuitive angular shifts in the photoelectron momentum distribution for atoms in strong few-cycle circularly polarized laser pulses." In: *Journal of Physics B: Atomic, Molecular and Optical Physics* 42.16 (2009), p. 161001. DOI: 10.1088/0953-4075/42/16/161001. URL: https://dx.doi.org/10.1088/0953-4075/42/16/161001.

[136] R. R. Freeman, P. H. Bucksbaum, H. Milchberg, S. Darack, D. Schumacher, and M. E. Geusic. "Above-threshold ionization with subpicosecond laser pulses." In: *Phys. Rev. Lett.* 59 (10 1987), pp. 1092–1095. DOI: 10.1103/PhysRevLett.59.1092. URL: https://link.aps.org/doi/10.1103/PhysRevLett.59.1092.

[137] L. A. Lompré, A. L'Huillier, G. Mainfray, and C. Manus. "Laser-Intensity Effects in the Energy Distributions of Electrons Produced in Multiphoton Ionization of Rare Gases." In: *Journal of the Optical Society of America B* 2.12 (Dec.

1985), pp. 1906–1912. DOI: 10.1364/JOSAB.2.001906. URL: https://opg.optica.org/josab/abstract.cfm?URI=josab-2-12-1906.

[138] D. Feldmann, D. Petring, G. Otto, et al. "Angular distribution of photo electrons from above-threshold-ionization (ATI) of xenon by 532 nm, 355 nm and 266 nm radiation." In: *Zeitschrift für Physik D - Atoms, Molecules and Clusters* 6 (1987). Z Phys D - Atoms, Molecules and Clusters, pp. 35–42. DOI: 10.1007/BF01436995. URL: https://doi.org/10.1007/BF01436995.

[139] R. R. Freeman, P. H. Bucksbaum, H. Milchberg, S. Darack, D. Schumacher, and M. E. Geusic. "Above-threshold ionization with subpicosecond laser pulses." In: *Phys. Rev. Lett.* 59 (10 1987), pp. 1092–1095. DOI: 10.1103/PhysRevLett.59.1092. URL: https://link.aps.org/doi/10.1103/PhysRevLett.59.1092.

[140] Aleksander Skjerlie Simonsen and Morten Førre. "Magnetic-field-induced enhancement of atomic stabilization in intense high-frequency laser fields." In: *Physical Review A* 92.1 (July 2015). Phys. Rev. A, p. 013405. ISSN: 1050-2947. DOI: 10.1103/PhysRevA.92.013405. URL: https://link.aps.org/doi/10.1103/PhysRevA.92.013405.

[141] Leonard Rosenberg and Fei Zhou. "Generalized Volkov wave functions: Application to laser-assisted scattering." In: *Phys. Rev. A* 47 (3 1993), pp. 2146–2155. DOI: 10.1103/PhysRevA.47.2146. URL: https://link.aps.org/doi/10.1103/PhysRevA.47.2146.

[142] Birger Böning. "Above-threshold ionization driven by spatially structured laser fields." en. Dissertation, Friedrich-Schiller-Universität Jena, 2020. PhD thesis. Jena, 2020. DOI: 10.22032/dbt.45092. URL: https://www.db-thueringen.de/receive/dbt_mods_00045092.

EHRENWÖRTLICHE ERKLÄRUNG

Ich erkläre hiermit ehrenwörtlich, dass ich die vorliegende Arbeit selbstständig, ohne unzulässige Hilfe dritter und ohne Benutzung anderer als der angegebenen Hilfsmittel und Literatur angefertigt habe. Die aus anderen Quellen direkt oder indirekt übernommenen Daten und Konzepte sind unter Angabe der Quelle gekennzeichnet.
Bei der Anfertigung dieser Arbeit haben mir meine Betreuer und die Koautoren oben genannter Publikationen geholfen.
Weitere Personen waren an der inhaltlich-materiellen Erstellung der vorliegenden Arbeit nicht beteiligt. Insbesondere habe ich hierfür nicht die entgeltliche Hilfe von Vermittlungs- bzw. Beratungsdiensten (Promotionsberater oder andere Personen) in Anspruch genommen.
Niemand hat von mir unmittelbar oder mittelbar geldwerte Leistungen für Arbeiten erhalten, die im Zusammenhang mit dem Inhalt der vorgelegten Dissertation stehen.
Die Arbeit wurde bisher weder im In- noch im Ausland in gleicher oder ähnlicher Form einer anderen Prüfungsbehörde vorgelegt. Die geltende Promotionsordnung der Physikalisch-Astronomischen Fakultät ist mir bekannt.
Ich versichere ehrenwörtlich, dass ich nach bestem Wissen die reine Wahrheit gesagt und nichts verschwiegen habe.

Jena,

Danish Furekh Dar

EIGENSTÄNDIGKEITSERKLÄRUNG

1. Hiermit versichere ich, dass ich die vorliegende Arbeit - bei einer Gruppenarbeit die von mir zu verantwortenden und entsprechend gekennzeichneten Teile - selbstständig verfasst und keine anderen als die angegebenen Quellen und Hilfsmittel benutzt habe. Ich trage die Verantwortung für die Qualität des Textes sowie die Auswahl aller Inhalte und habe sichergestellt, dass Informationen und Argumente mit geeigneten wissenschaftlichen Quellen belegt bzw. gestützt werden. Die aus fremden oder auch eigenen, älteren Quellen wörtlich oder sinngemäß übernommenen Textstellen, Gedankengänge, Konzepte, Grafiken etc. in meinen Ausführungen habe ich als solche eindeutig gekennzeichnet und mit vollständigen Verweisen auf die jeweilige Quelle versehen. Alle weiteren Inhalte dieser Arbeit ohne entsprechende Verweise stammen im urheberrechtlichen Sinn von mir.
2. Ich weiß, dass meine Eigenständigkeitserklärung sich auch auf nicht zitierfähige, generierende KI-Anwendungen (nachfolgend „generierende KI“) bezieht. Mir ist bewusst, dass die Verwendung von generierender KI unzulässig ist, sofern nicht deren Nutzung von der prüfenden Person ausdrücklich freigegeben wurde (Freigabeerklärung). Sofern eine Zulassung als Hilfsmittel erfolgt ist, versichere ich, dass ich mich generierender KI lediglich als Hilfsmittel bedient habe und in der vorliegenden Arbeit mein gestalterischer Einfluss deutlich überwiegt. Ich verantworte die Übernahme der von mir verwendeten maschinell generierten Passagen in meiner Arbeit vollumfänglich selbst. Für den Fall der Freigabe der Verwendung von generierender KI für die Erstellung der vorliegenden Arbeit wird eine Verwendung in einem gesonderten Anhang meiner Arbeit kenntlich gemacht. Dieser Anhang enthält eine Angabe oder eine detaillierte Dokumentation über die Verwendung generierender KI gemäß den Vorgaben in der Freigabeerklärung der prüfenden Person. Die Details zum Gebrauch generierender KI bei der Erstellung der vorliegenden Arbeit inklusive Art, Ziel und Umfang der Verwendung sowie die Art der Nachweispflicht habe ich der Freigabeerklärung der prüfenden Person entnommen.
3. Ich versichere des Weiteren, dass die vorliegende Arbeit bisher weder im In- noch im Ausland in gleicher oder ähnlicher Form einer anderen Prüfungsbehörde vorgelegt wurde oder in deutscher oder einer anderen Sprache als Veröffentlichung erschienen ist.
4. Mir ist bekannt, dass ein Verstoß gegen die vorbenannten Punkte prüfungsrechtliche Konsequenzen haben und insbesondere dazu führen kann, dass meine Prüfungsleis-

tung als Täuschung und damit als mit „nicht bestanden“ bewertet werden kann. Bei mehrfachem oder schwerwiegendem Täuschungsversuch kann ich befristet oder sogar dauerhaft von der Erbringung weiterer Prüfungsleistungen in meinem Studiengang ausgeschlossen werden.

Jena,

Danish Furekh Dar

Curriculum Vitae

Personal information

Name: Danish Furekh Dar
Date of Birth: 09 February 1998
Place of Birth: Anantnag, Jammu and Kashmir, India

School education

02. 2004 – 12. 2005: Hanfia Islamia Eductional Institue, Pahalgam (Kullar), (Primary school)
Jammu and Kashmir, India

02. 2006 – 12. 2007: Imamia Public High School, Pahalgam (Sofipora), (Primary school)
Jammu and Kashmir, India

02. 2008 – 12. 2009: Army Goodwill School, Aishmuqam, (Primary school)
Jammu and Kashmir, India

02. 2010 – 12. 2011: Public English Medium School, bijbehara, (Primary school)
Jammu and Kashmir, India

02. 2012 – 12. 2012: Govt Middle School, Kullar, (Secondary school)
Jammu and Kashmir, India

02. 2013 – 12. 2015: Govt Higher Secondary School, Kullar, (Secondary school)
Jammu and Kashmir, India

University education

06. 2016 – 05. 2019: B.Sc. (Honours School) Physics,
Guru Nanak Dev University, Amritsar, Punjab, India

06. 2019 – 09. 2021: M.Sc. (Honours School) Physics,
Guru Nanak Dev University, Amritsar, Punjab, India

Doctoral studies

03. 2022 – Present: Research student
Helmholtz Institute Jena, Germany

Location: Signature
Date: